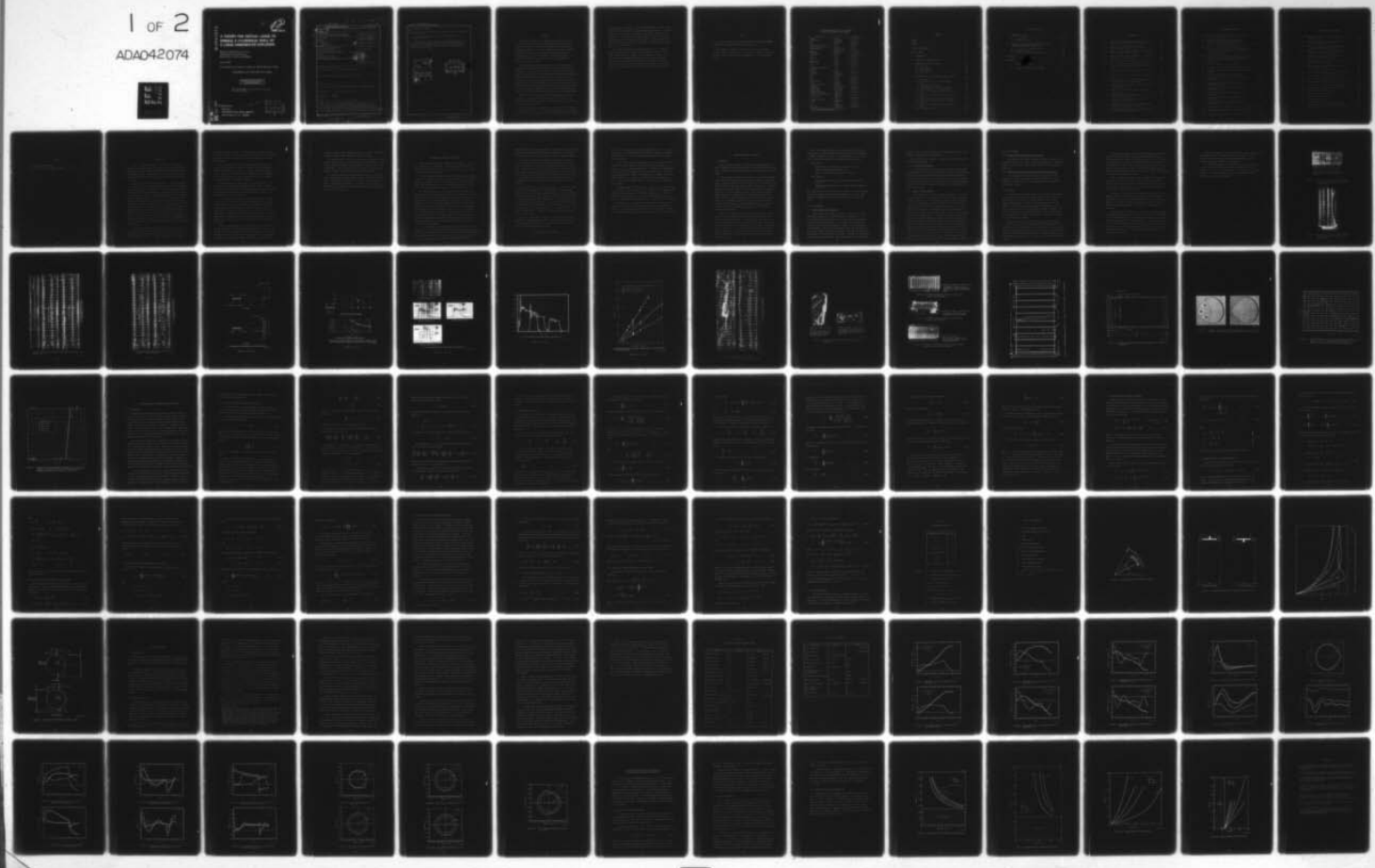


AD-A042 074 STANFORD RESEARCH INST MENLO PARK CALIF F/G 15/6
A THEORY FOR CRITICAL LOADS TO DAMAGE A CYLINDRICAL SHELL BY A --ETC(U)
JUN 76 A L FLORENCE, G R ABRAHAMSON DNA001-72-C-0087
UNCLASSIFIED DNA-4047F NL

1 OF 2
ADA042074



ADA042074

J
12
DNA 4047F

A THEORY FOR CRITICAL LOADS TO DAMAGE A CYLINDRICAL SHELL BY A LARGE UNDERWATER EXPLOSION

Stanford Research Institute
333 Ravenswood Avenue
Menlo Park, California 94025

June 1976

Final Report for Period 1 February 1972—26 April 1973

CONTRACT No. DNA 001-72-C-0087

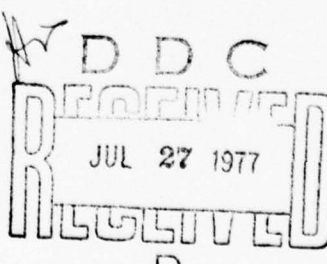
APPROVED FOR PUBLIC RELEASE;
DISTRIBUTION UNLIMITED.

THIS WORK SPONSORED BY THE DEFENSE NUCLEAR AGENCY
UNDER SUBTASK NB002-10.

AU NO. —
DDC FILE COPY

Prepared for
Director
DEFENSE NUCLEAR AGENCY
Washington, D. C. 20305

see 1473



UNCLASSIFIED

SECURITY CLASSIFICATION OF THIS PAGE (When Data Entered)

(9) Final rept. 1 Feb 72-

26 Apr 73,

REPORT DOCUMENTATION PAGE		READ INSTRUCTIONS BEFORE COMPLETING FORM
1. REPORT NUMBER DNA 4047F	2. GOVT ACCESSION NO.	3. RECIPIENT'S CATALOG NUMBER
4. TITLE (and Subtitle) A THEORY FOR CRITICAL LOADS TO DAMAGE A CYLINDRICAL SHELL BY A LARGE UNDERWATER EXPLOSION.		5. TYPE OF REPORT & PERIOD COVERED Final Report for Period 1 Feb 72—26 Apr 73
6. AUTHOR(S) A. L. Florence G. R. Abrahamson		7. PERFORMING ORG. REPORT NUMBER SRI Project PYU-1714
8. CONTRACT OR GRANT NUMBER(S) DNA 001-72-C-0087 new		9. PERFORMANCE ORGANIZATION NAME AND ADDRESS Stanford Research Institute 333 Ravenswood Avenue Menlo Park, California 94025
10. PROGRAM ELEMENT PROJECT, TASK AREA & WORK UNIT NUMBERS Subtask NB002-10		11. CONTROLLING OFFICE NAME AND ADDRESS Director Defense Nuclear Agency Washington, D.C. 20305
12. REPORT DATE June 1976		13. NUMBER OF PAGES 118 p.
14. MONITORING AGENCY NAME & ADDRESS (if different from Controlling Office)		15. SECURITY CLASS (of this report) UNCLASSIFIED
16. DISTRIBUTION STATEMENT (of this Report) Approved for public release; distribution unlimited.		
17. DISTRIBUTION STATEMENT (of the abstract entered in Block 20, if different from Report)		
18. SUPPLEMENTARY NOTES This work sponsored by the Defense Nuclear Agency under Subtask NB002-10.		
19. KEY WORDS (Continue on reverse side if necessary and identify by block number) Submarine Nuclear Underwater Explosion		
20. ABSTRACT (Continue on reverse side if necessary and identify by block number) A theory is presented for determining critical loads for cylindrical shells subjected to large underwater explosions. The theory treats dynamic elastic-plastic buckling with fluid-structure interaction caused by a transverse incident pulse in water. The approach is by modal analysis with the displacement and velocity distributions at the end of the initial elastic response forming the initial conditions of the subsequent plastic		

332500 JB

UNCLASSIFIED

SECURITY CLASSIFICATION OF THIS PAGE(When Data Entered)

20. ABSTRACT (Continued)

response. The transition from elastic to plastic response is determined by the hoop mode.

Experimental and theoretical final deformed shapes and pressure histories are similar.

The response of a stiffened shell to a rectangular pressure pulse is characterized by isodamage curves in the pressure-impulse plane. Results show steep damage gradients when pressures and durations exceed the values that cause incipient damage, which is in agreement with experimental observation.

ACCESSION for	
NTIS	White Section <input checked="" type="checkbox"/>
DOC	Buff Section <input type="checkbox"/>
UNANNOUNCED	<input type="checkbox"/>
JUSTIFICATION.....	
BY.....	
DISTRIBUTION/AVAILABILITY CODES	
DIST.	AVAIL and/or SPECIAL
A	

D D C
REFINED
JUL 27 1977
RECORDED
D

UNCLASSIFIED

SECURITY CLASSIFICATION OF THIS PAGE(When Data Entered)

SUMMARY

A theory is presented for determining critical load curves for cylindrical shells subjected to large underwater explosions. The theory treats dynamic elastic-plastic buckling with fluid-structure interaction caused by a transverse incident pulse in water. Specific results are generated for a rectangular incident pressure pulse (instantaneous rise, constant pressure, instantaneous decay) as a reasonable idealization of a shock wave from a large underwater explosion with surface cutoff.

Wavelengths observed in experiments (Fig 3.11) indicate that the predominant buckling mode forms during the initial elastic phase of deformation. This mode enters the initial conditions of the plastic phase of deformation and is the preferred mode for further amplification. Therefore, the theoretical approach is to treat the initial elastic response of the shell by model analysis until plasticity occurs in the hoop mode, and to use the displacement and velocity distributions at this time as initial conditions for the subsequent plastic response. Amplification of the preferred buckling mode is assumed to continue during the plastic phase until the hoop mode reaches the maximum inward displacement.

Experimental and theoretical final deformed shapes are similar (as shown in Figures 3.11 and 5.9), indicating the validity of the approach. Experimental and theoretical pressure histories are also similar (Figures 3.12, 5.16, A-3).

Structural damage is represented by an isodamage curve in the P-I (pressure-impulse) plane. For an incident rectangular pulse of pressure P and duration T , the impulse is $I = PT$. Damage is taken as the maximum

permanent radial displacement δ ; in dimensionless terms δ may be a fraction of the shell radius or a multiple of the shell thickness. A pressure-impulse curve is therefore the curve in the P-I plane on which δ is a constant; the curve connects rectangular pulses of equal effectiveness that range from ideal impulses to step loading. Pressure-impulse curves (Figure 6.2) were generated for an externally stiffened cylindrical shell (Table 5.1, Figure 4.2a).

It is shown by example that the excess impulse is not a constant along an isodamage curve but may vary by as much as a factor of two; this implies that excess impulse is not as accurate a measure of the damage potential of underwater shock waves as the P-I representation. Plots of the relationship between damage δ and pressure or duration (Figures 6.3 and 6.4) show how damage gradients steepen with increasing P and T, in conformance with experimental observation (Figures 3.13 and 6.4).

PREFACE

This work was done under Contract DNA001-72-C-0087, Subtask NB002. Commander D. M. Alderson was the Technical Monitor.

The authors are indebted to B. Bain for computer programming, numerical results, and plots, and to J. Malinak, C. Romander, J. Busma, E. Eckert, and C. Benson for their contributions to the experimental results.

Conversion factors for U.S. customary
to metric (SI) units of measurement.

To Convert From	To	Multiply By
angstrom	meters (m)	1. 000 000 X E -10
atmosphere (normal)	kilo pascal (kPa)	1. 013 25 X E +2
bar	kilo pascal (kPa)	1. 000 000 X E +2
barn	meter ² (m ²)	1. 000 000 X E -28
British thermal unit (thermochemical)	joule (J)	1. 054 350 X E +3
calorie (thermochemical)	joule (J)	4. 184 000
cal (thermochemical)/cm ²	mega joule/m ² (MJ/m ²)	4. 184 000 X E -2
curie	*giga becquerel (GBq)	3. 700 000 X E +1
degree (angle)	radian (rad)	1. 745 329 X E -2
degree Fahrenheit	degree kelvin (K)	$t_K = (t^{\circ} F + 459.67)/1.8$
electron volt	joule (J)	1. 602 19 X E -19
erg	joule (J)	1. 000 000 X E -7
erg/second	watt (W)	1. 000 000 X E -7
foot	meter (m)	3. 048 000 X E -1
foot-pound-force	joule (J)	1. 355 818
gallon (U. S. liquid)	meter ³ (m ³)	3. 785 412 X E -3
inch	meter (m)	2. 540 000 X E -2
jerk	joule (J)	1. 000 000 X E +9
joule/kilogram (J/kg) (radiation dose absorbed)	Gray (Gy)	1. 000 000
kilotons	terajoules	4. 183
kip (1000 lbf)	newton (N)	4. 448 222 X E +3
kip/inch ² (ksi)	kilo pascal (kPa)	6. 894 757 X E +3
ktap	newton-second/m ² (N-s/m ²)	1. 000 000 X E +2
micron	meter (m)	1. 000 000 X E -6
mil	meter (m)	2. 540 000 X E -5
mile (international)	meter (m)	1. 609 344 X E +3
ounce	kilogram (kg)	2. 834 952 X E -2
pound-force (lbs avoirdupois)	newton (N)	4. 448 222
pound-force inch	newton-meter (N·m)	1. 129 848 X E -1
pound-force/inch	newton/meter (N/m)	1. 751 268 X E +2
pound-force/foot ²	kilo pascal (kPa)	4. 788 026 X E -2
pound-force/inch ² (psi)	kilo pascal (kPa)	6. 894 757
pound-mass (lbm avoirdupois)	kilogram (kg)	4. 535 924 X E -1
pound-mass-foot ² (moment of inertia)	kilogram-meter ² (kg·m ²)	4. 214 011 X E -2
pound-mass/foot ³	kilogram/meter ³ (kg/m ³)	1. 601 846 X E +1
rad (radiation dose absorbed)	**Gray (Gy)	1. 000 000 X E -2
roentgen	coulomb/kilogram (C/kg)	2. 579 760 X E -4
shake	second (s)	1. 000 000 X E -8
slug	kilogram (kg)	1. 459 390 X E +1
torr (mm Hg, 0° C)	kilo pascal (kPa)	1. 333 22 X E -1

*The becquerel (Bq) is the SI unit of radioactivity; 1 Bq = 1 event/s.

**The Gray (Gy) is the SI unit of absorbed radiation.

CONTENTS

SUMMARY	1
PREFACE	3
LIST OF ILLUSTRATIONS	7
LIST OF TABLES	10
1. INTRODUCTION	11
2. THEORETICAL APPROACH AND RESULTS	14
3. EXPERIMENTAL BASIS FOR THEORY	17
3.1 Background	17
3.2 Hoop Response	18
3.3 Axial Response	20
3.4 Discussion	20
4. BUCKLING THEORY OF SUBMERGED CYLINDRICAL SHELLS	39
4.1 Backgroud	39
4.2 Governing Equation of Initial Elastic Phase	40
4.3 Fluid-Shell Interaction	43
4.4 Approximate Unit Resistance Functions	49
4.5 Representation of a Rectangular Pulse	50
4.6 System of Governing Equations of Elastic Phase	52
4.7 Solution of Governing Equations of Elastic Phase	53
4.8 Governing Equation of the Plastic Phase	56
4.9 System of Governing Equations of Plastic Phase	57
4.10 Solution of Governing Equations of Plastic Phase	58
4.11 Final Deformation	60

CONTENTS (continued)

5.	THEORETICAL RESULTS	67
5.1	Numerical Data	67
5.2	Numerical Results	67
6.	PRESSURE-IMPULSE ISODAMAGE REPRESENTATION AND COMPARISON WITH EXCESS IMPULSE RULE	86
6.1	PI Curves for a Cylindrical Shell	86
6.2	Physical Quantities	87
6.3	Comparison with Excess Impulse Rule	88
	REFERENCES	93
	APPENDICES	
A	EXCESS IMPULSE RULE	95
B	SUMMARY OF MATHEMATICAL TREATMENT	103

ILLUSTRATIONS

3.1	Quasi-Static Overall Buckling Produced by an Underwater Explosion (Figure 10b of Reference 2)	23
3.2	Quasi-Static Overall Buckling Produced by a Hydrostatic Load (Figure 11 of Reference 3)	23
3.3a	Dynamic Plating Buckling Produced by an Underwater Explosion--Front and Back Views	24
3.3b	Dynamic Plating Buckling Produced by an Underwater Explosion--Top and Bottom Views	25
3.3c	Experimental Setup for Model of Figures 3.3a and b	26
3.3d	Results of Charge Calibration Tests. Model of Figures 3.3a and b was at 24-inch Range. Model of Figure 3.4 was at 18-inch Range	27
3.3e	Typical Pressure Records from Charge Calibration Tests	28
3.3f	Plot of Pressure Pulses from Charge Calibration Tests	29
3.3g	Underwater Shock Wave Pressure Versus Inverse of Standoff Distance for Various Charges	30
3.4	Dynamic Overall Buckling. See Figures 3.3c and d for Experimental Setup	31
3.5	Dynamic Overall Buckling (Figures 10c and 10f of Reference 2)	32
3.6	Dynamic Plating Buckling Due to Axial Load (Figure 10a of Reference 2)	33
3.7	Dynamic Plating Buckling Due to Axial Load (Figure 10e of Reference 2)	33
3.8	Dynamic Plating Buckling Due to Overall Bending (Whipping) (Figure 10d of Reference 2)	33
3.9	Principal Dimensions of Models of Figures 3.1 and 3.5-3.8 (Figure 1 of Reference 2)	34

ILLUSTRATIONS (continued)

3.10	Principal Dimensions of Models of Figures 3.2-3.4 (Figure 1 of Reference 3)	35
3.11	Dynamic Overall Buckling of Uniform Shells (Al 6061-T6, 3-inch diameter, 1/16-inch wall) Produced by Underwater Explosions	36
3.12	Surface Pressure at Point of First Loading on a Model Like Those of Figure 3.11, as Measured with a Thin Foil (~ 1 mil) Ytterbium Gage Attached to the Model (Reference 4)	37
3.13	Maximum Permanent Deformation Versus Ratio of Total Peak Pressure to Hydrostatic Collapse Pressure for Models of Submarine Pressure Hulls (Figure 9 of Reference 2).	38
4.1	Notation. Element of Shell in Motion	63
4.2	Configurations for Ring-Stiffened Cylindrical Shells . .	64
4.3	Comparison of Approximate and Exact Unit Resistance Functions	65
4.4	Rectangular Pulse Passing Cylindrical Shell	66
5.1	Displacement and Velocity Amplitudes for the Hoop Mode ($n = 0$)	75
5.2	Displacement and Velocity Amplitudes for the Translational Mode ($n = 1$)	75
5.3	Displacement and Velocity Amplitudes for the Second Mode ($n = 2$)	76
5.4	Displacement and Velocity Amplitudes for the Third Mode ($n = 3$)	76
5.5	Displacement and Velocity Amplitudes for the Fourth Mode ($n = 4$)	77
5.6	Displacement and Velocity Amplitudes for the Fifth Mode ($n = 5$)	77
5.7	Modal Displacement Amplitudes at Times \bar{t} , T , and t_f . .	78
5.8	Shell Displacement at Times \bar{t} , T , and t_f (maximum $n = 10$)	78
5.9	Final Shell Deformation ($t = t_f$, maximum $n = 10$)	79

ILLUSTRATIONS (concluded)

5.10	Outer Fiber Strains at Times \bar{t} , T, and t_f (maximum n = 10)	79
5.11	Diffraction, Radiation, and Total Pressures Associated with Hoop Mode (n = 0)	80
5.12	Diffraction, Radiation, and Total Pressures Associated with Translational Mode (n = 1)	80
5.13	Diffraction, Radiation, and Total Pressure Associated with Second Mode (n = 2)	81
5.14	Diffraction, Radiation, and Total Pressures Associated with Third Mode (n = 3)	81
5.15	Diffraction Pressure at Front, Top and Bottom, and Rear of Rigid, Fixed Cylinder	82
5.16	Total Pressure at Front, Top and Bottom, and Rear of Cylindrical Shell.	82
5.17	Total Pressure Distribution at Time $t = 0.5$	83
5.18	Total Pressure Distribution at Time $t = \bar{t} = 1.15$	83
5.19	Total Pressure Distribution at Time $t = 2$	84
5.20	Total Pressure Distribution at Time $t = T = 3$	84
5.21	Total Pressure Distribution at Time $t = t_f = 4.13$	85
6.1	Isodamage Curves in Pressure-Duration Plane.	89
6.2	Isodamage Curves in Pressure-Impulse Plane	90
6.3	Damage-Duration Gradient Curves	91
6.4	Damage-Pressure Gradient Curves	92
A.1	Definition of Excess Impulse	99
A.2	Rigid-Plastic System	100
A.3	Calculated and Measured Pressure Histories	101
A.4	Plot of Experimental Data Showing Relationship of K_s and K_σ	102

TABLES

4.1 Dimensionless Quantities	61
5.1 Data for Stiffened Cylindrical Shell	73

1. INTRODUCTION

Damage to a submerged submarine as the result of an underwater explosion is commonly divided into two principal classes, hull damage and equipment damage. Severe hull damage affects the seaworthiness of the submarine; damage to equipment, i.e., machinery, weapons systems, and other items that are not part of the hull, affects mobility and fire power.

Damage to the cylindrical pressure hull of a submerged submarine by an underwater nuclear explosion is currently predicted by the Excess Impulse Rule (described in Appendix A). This is an empirical formula for the maximum stiffener deflection and is based on the correlation of test results for a variety of hulls loaded by approximately rectangular pressure pulses that simulate those from large explosions at large standoff. Test results correlated by the Excess Impulse Rule exhibit considerable scatter. Moreover, because of the empirical nature of the Excess Impulse Rule, its applicability to the prediction of damage outside the range of the tests on which it is based is questionable. In particular, beyond a certain depth, the Excess Impulse Rule indicates that, for a given pressure pulse, stiffener deflection decreases with depth of submergence. Since hydrostatic pressure increases with depth, it is intuitively obvious that the depth dependence of the Excess Impulse Rule is incorrect.

The purpose of the work reported here is to provide a theory for correlating available experimental results and for interpolating and extrapolating the results to other situations. To make interpolation and extrapolation valid, it is essential that the theory be based on

the correct physical mechanisms. To determine the mechanisms on which the theory should be based, we examined hull deformations in scale models produced by underwater explosions. From these observations the theory was developed.

Critical load curves for military structures under attack loads applied by gas pressure (air blast, for example) have been developed over the past decade or so in terms of critical peak-pressure/impulse curves. The utility of these curves for loads applied by gas pressure led to the suggestion that similar critical load curves be developed for loads resulting from underwater explosions.

In structures loaded by gas pressure, the compressibility of the gas makes the load essentially independent of the response. However, loads resulting from shock waves in water depend strongly on the response. This feature--the fluid-structure interaction--greatly complicates the determination of critical load curves.

In our first attempt to determine critical load curves for underwater explosions,¹ we used a rigid-plastic representation of the structure and determined the critical loads at the long-duration and short-duration extremes, taking approximate account of the fluid-structure interaction. An interpolation scheme was used to calculate the critical loads between the long-duration and short-duration extremes. While this theory agreed reasonably well with the test results on which the Excess Impulse Rule is based, it still did not provide a satisfactory theoretical basis.

A second attempt resulted in a theory that diverged substantially from the test results on which the Excess Impulse Rule is based. At this point we tried to find more details on those experiments to try to determine where the theory was wrong--in the representation of the structure or in the model of the fluid-structure interaction. We were unable to

find more details on those experiments and began a search for other experimental results, particularly scale model experiments.

We eventually found a few model test results from 1954-55 and performed a limited number of confirmatory tests in our laboratory. These results showed that buckling was the predominant response mode of the pressure hull. Hence an attempt was made to develop a revised theory based on buckling, instead of simple rigid-plastic response.

The work presented here combines dynamic buckling of cylindrical shells, developed at SRI over the past 15 years, with a Russian treatment of fluid-structure interaction. The result is a plausible theory based on experimental observations. We believe it points the way to theoretical understanding of other response modes involving buckling and fluid-structure interaction.

2. THEORETICAL APPROACH AND RESULTS

In the theory developed here, dynamic overall buckling is taken as the critical mode for hull damage. Experimental results show that the damage gradient with increasing load is steep; hence an analysis based on threshold response is adequate.

The theory describes buckling caused by a transverse incident pulse in water with specific results for a rectangular pulse, that is, a pulse with an instantaneous rise, a constant pressure, and an instantaneous decay. The rectangular pulse is a reasonable idealization of a shock wave from an underwater nuclear explosion, with surface cutoff.

The wavelengths observed in experiments indicate that the predominant buckling mode forms during the initial elastic phase of deformation. This mode enters the initial conditions of the plastic phase and is the preferred mode for further amplification. Therefore, the theoretical approach is to treat the initial response of the shell by elastic modal analysis until plasticity occurs in the hoop mode, and to use the displacement and velocity distributions at this time as initial conditions for the subsequent plastic response. Amplification of the preferred buckling mode is assumed to continue during the plastic phase until the hoop mode reaches the maximum inward radial displacement. The experimental and theoretical final deformed shapes are similar, indicating the validity of the approach.

It is also observed in experiments that a central length of shell buckles to a shape that does not depend on the axial position of the cross section. This deformation pattern is seen in the shell shown in Figure 3.4. Also, the cross section of the shell in Figure 3.11 has a shape that is typical of the shapes of slices that were cut along the shell for a

central length covering several diameters. This observation justified the simplifying assumption of analyzing dynamic buckling of a ring instead of a cylindrical shell of finite length, a much more complicated problem.

Experimental and theoretical pressure histories at the first contact of the pulse with the shell also show good agreement exhibiting a sharp rise followed by a sharp decay and gradual rise (Figures 3.12 and 5.16). The final decay differs because the theory is based on an idealized rectangular pulse. Aside from the final decay, the main difference in the pulses is the pressure level in the valley between the sharp decay and gradual rise. This pressure level depends on the nature of the structure, and since the structures differ, these levels should not be the same.

An effective way of representing the damage of a structure to pulse loading is by an isodamage curve in the P-I (pressure-impulse) plane (Figure 6.2). For an incident rectangular pulse of pressure P and duration T , the impulse is $I = PT$. Damage to a submarine shell may be taken as the maximum permanent radial displacement δ ; in dimensionless terms this displacement may be represented as a fraction of the shell radius or a multiple of the shell thickness. A pressure-impulse curve is therefore the curve in the P-I plane on which δ is a constant; the curve connects rectangular pulses of equal effectiveness that range from ideal impulse to step loading.

The theory developed here was used to generate P-I curves for an externally stiffened cylindrical shell. The pressure and duration of the incident rectangular pulses are represented by P and T , and the damage is represented nondimensionally by

$$\delta_a = \max |w(\theta, t_f) - w_1(t_f) \cos \theta|$$

that is, by the maximum inward radial displacement at the time t_f when the hoop mode inward displacement $w_o(t)$ reaches a maximum. The displacement parameter δ_a is the final maximum inward displacement divided by the shell radius a .

For the model cylindrical shell subjected to a rectangular incident pulse with a duration equal to a transit time of two diameters ($t_d = 100 \mu\text{sec}$, $T = 4$), an incident pressure of $p_i = 2046 \text{ psi}$ ($P = 0.0062$) will cause a permanent deformation of 3.5 wall thicknesses ($\delta_a = 0.04$); the corresponding incident impulse is 204 psi-msec ($I = 0.0248$). The static yield pressure is $p_y = \sigma(kH)/a = 925 \text{ psi}$, giving a pressure ratio $p_i/p_y = 2.21$; thus the excess impulse is $I_x = (p_i - p_y)t_d = 112 \text{ psi-msec}$ ($I = 0.0136$).

As another example, if the pulse has a transit time of four diameters ($t_d = 200 \mu\text{sec}$, $T = 8$), a pressure of $p_i = 1250 \text{ psi}$ ($P = 0.0038$) will also cause a permanent deformation of 3.5 wall thicknesses ($\delta_a = 0.04$); the pressure ratio is now $p_i/p_y = 1.35$. The incident impulse is 250 psi-msec ($I = 0.0304$) and the excess impulse is $I_x = 65 \text{ psi-msec}$ ($I = 0.0079$).

Examination of the isodamage curves shows that the excess impulse depends on the P-I or P-T point selected. Hence, excess impulse is not constant for constant damage and is therefore not as accurate a measure of the damage potential of underwater shock waves as the P-I representation.

3. EXPERIMENTAL BASIS FOR THEORY

3.1 BACKGROUND

Model tests were conducted to simulate the response modes that occur in submarine pressure hulls loaded by underwater shock waves from large explosions. The results of these tests formed the basis for our theory.

We first looked for large-scale test results to determine response modes. However, the available results were very sketchy, undoubtedly because the damage gradient with increasing load is very steep, as shown below. Because of this steep damage gradient, achievement of threshold response requires either precise critical load predictions and precise load control or a large number of tests. Large explosions generally produce loads that are uncertain by at least 10 percent, which is enough to span the range from no damage to extensive damage. Hence, except for an occasional luck result, many test structures must be fielded with large explosions to get threshold response. Since this is costly, there are not enough large scale tests to illustrate threshold response modes.

Contrary to our expectations, we also found very few model test results to review. Inquiries to the Navy led to United States Naval Research and Development Center, Carderock, as the best source. In a visit to Carderock, we acquired two references^{2,3} dated 1954 and 1955, which describe model tests in preparation for the Pacific nuclear test WIGWAM. Apparently, no other model tests showing threshold response have been reported. To verify these results and obtain quantitative response information, we supplemented the available results with some model tests at SRI.

Model test results illustrating the various threshold response modes evoked by simulated underwater shock waves from nuclear explosion are shown in Figures 3.1 to 3.8. The response modes may be classified as the following variations of hoop response and axial response:

Hoop response

Quasi-static overall buckling (Figures 3.1 and 3.2)

Dynamic plating buckling (Figure 3.3)

Dynamic overall buckling (Figures 3.4 and 3.5)

Axial response

Dynamic plating buckling due to axial load (Figures 3.6 and 3.7)

Dynamic plating buckling due to overall bending (whipping) (Figure 3.8).

Hull dimensions are given in Figure 3.9 for Figures 3.1 and 3.5 through 3.8, and in Figure 3.10 for Figures 3.2 through 3.4. Each of these modes and the mechanisms by which they are activated are discussed below.

3.2 HOOP RESPONSE

3.2.1 Quasi-Static Overall Buckling

This response mode, shown in Figure 3.1, consists of a single inward lobe extending over several stiffeners. In this example, the lobe is about two hull diameters long. A similar model loaded hydrostatically is shown in Figure 3.2. The response is essentially the same as in the model loaded dynamically. Hence, the term quasi-static overall buckling. This is the well-studied classic buckling behavior of a finite cylinder under external pressure. Buckling occurs when the hoop thrust in the hull becomes great enough to overcome the hoop bending resistance in the critical mode. The nonuniformity of the dynamic load

does not affect the basic response mode, but probably affects the load required to produce a given response level.

Quasi-static overall buckling is a special case of dynamic overall buckling described below.

3.2.2 Dynamic Plating Buckling

This response mode, shown in Figure 3.3, consists of inward and outward dimpling of the hull plating between stiffeners. Inward dimpling occurs alone, but outward dimpling always occurs between two inward dimples. Dimpling occurs when the hoop thrust is sufficient to overcome the bending resistance of the plating in this mode. Since this response mode results in relatively minor hull damage, it is not considered the critical damage mode.

3.2.3 Dynamic Overall Buckling

This response mode is shown in Figures 3.4 and 3.5. It is similar to the quasi-static overall buckling in that the lobes extend over several stiffeners, but it differs in that there are several lobes instead of one (particularly evident in Figure 3.4). The shift from a single lobe to several lobes in the threshold mode is due to the difference in load duration. The response time for the development of a single lobe is greater than for several lobes. Hence, the load duration may be shorter than necessary to evoke the single lobe mode, but long enough to evoke higher order modes. This type of dynamic buckling in higher order modes is called pulse buckling and has been studied extensively at SRI over the past 15 years (see Section 4 for references). The analysis yields time-dependent amplification factors for the various modes. Typically, the amplification factors show a peak that extends over a few modes. If the load duration is long enough, the peak occurs in the region of the static buckling mode. The most-magnified modes predicted by the theory generally agree well with experimental results.

3.3 AXIAL RESPONSE

3.3.1 Dynamic Plating Buckling Due to Axial Load

This response mode, shown in Figures 3.6 and 3.7, consists of an inward deformation of the plating between stiffeners that may extend all around the circumference (Figure 3.6) or only a few stiffener spacings (Figure 3.7).

3.3.2 Dynamic Plating Buckling Due to Overall Bending (Whipping)

This response mode, shown in Figure 3.8, consists of inward buckling of the plating between the central stiffeners due to axial bending. The buckles occur on the compressive side and extend over a few stiffener spacings.

3.4 DISCUSSION

The response modes described above involve instability under pulse loads. They can all be treated by pulse buckling theory. The theory developed here is restricted to the hoop response mode of dynamic overall buckling, which is taken as the critical hoop mode for hull damage. As shown below, the damage gradient with increasing load is steep; hence an analysis based on threshold response is adequate. The theory for dynamic overall buckling developed earlier for loads that are independent of the response was extended to account for the effects of fluid-structure interaction.

The general goal in the design of stiffened shells for hulls is to match the critical load for the plating between stiffeners and the critical load for overall bending of the plating and stiffeners together. Moreover, the stiffeners are designed not to fail by lateral buckling as shown in Figures 3.3(b) and 3.4(a). Hence an ideally designed stiffener shell would behave essentially as a uniform shell with increased bending stiffness.

To examine the response of uniform shells to underwater shock wave loading, we tested a series of long aluminum (6061-T6) cylinders of 3-inch diameter and 1/16-inch wall. Cross sections of two of the cylinders are shown in Figure 3.11. At higher loads the central portion on the loaded side is driven inward, resulting in rupture along the loaded side. The cross sections of Figure 3.11 show that the mode numbers of interest in the threshold region are of the order of eight. This observation was used in developing the theory.

Figure 3.12 shows the pressure history measured on the surface of a model like those of Figure 3.11. This record was obtained with a thin foil (~ 1 mil) ytterbium gage attached to the surface of the model at the point of first loading.⁴ A similar record obtained by other means is shown in Appendix A (Figure A-3).

If dimpling of the hull plating (Figure 3.3) occurs before overall buckling, it will influence the overall buckling mode by introducing nonuniformities. Thus, the theory described in Section 4 should be regarded as a first step in applying pulse buckling theory to submarine pressure hulls, taking account of the effects of fluid-structure interaction.

As mentioned at the beginning of this section, the damage gradient in underwater structural response is steep. The basis for this observation is given in Figure 3.13. The ordinate in Figure 3.13 is the ratio of the peak deflection Δ to the wall thickness t . The abscissa is the ratio of the load (hydrostatic pressure P_o plus peak free field shock pressure P_m) to the collapse pressure of the hull P_c . We see that the deflection increases from 0 to more than 10 wall thicknesses for a 10 percent increase in load.

Comparison of Figures 3.3(a) and (b) with 3.4 further illustrates the steep damage gradient for underwater structural response. Here an increase in the free-field pressure from 750 to 1050 psi produced response ranging from threshold to hull rupture.

The steep damage gradient for underwater structural response means that the theory for critical load curves can be based on threshold response. This is very important because, in the analysis of threshold response, we can take advantage of many of the simplifications and idealizations of classical mechanics.

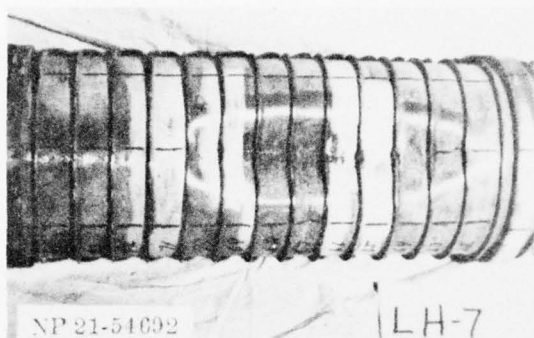
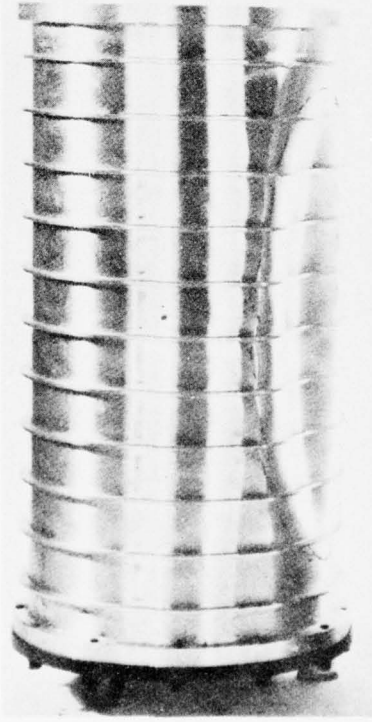


FIGURE 10b ~ MODEL LH-7 AFTER TEST 3-C
THE FAILURE IS OF THE OVERALL INSTABILITY
TYPE.

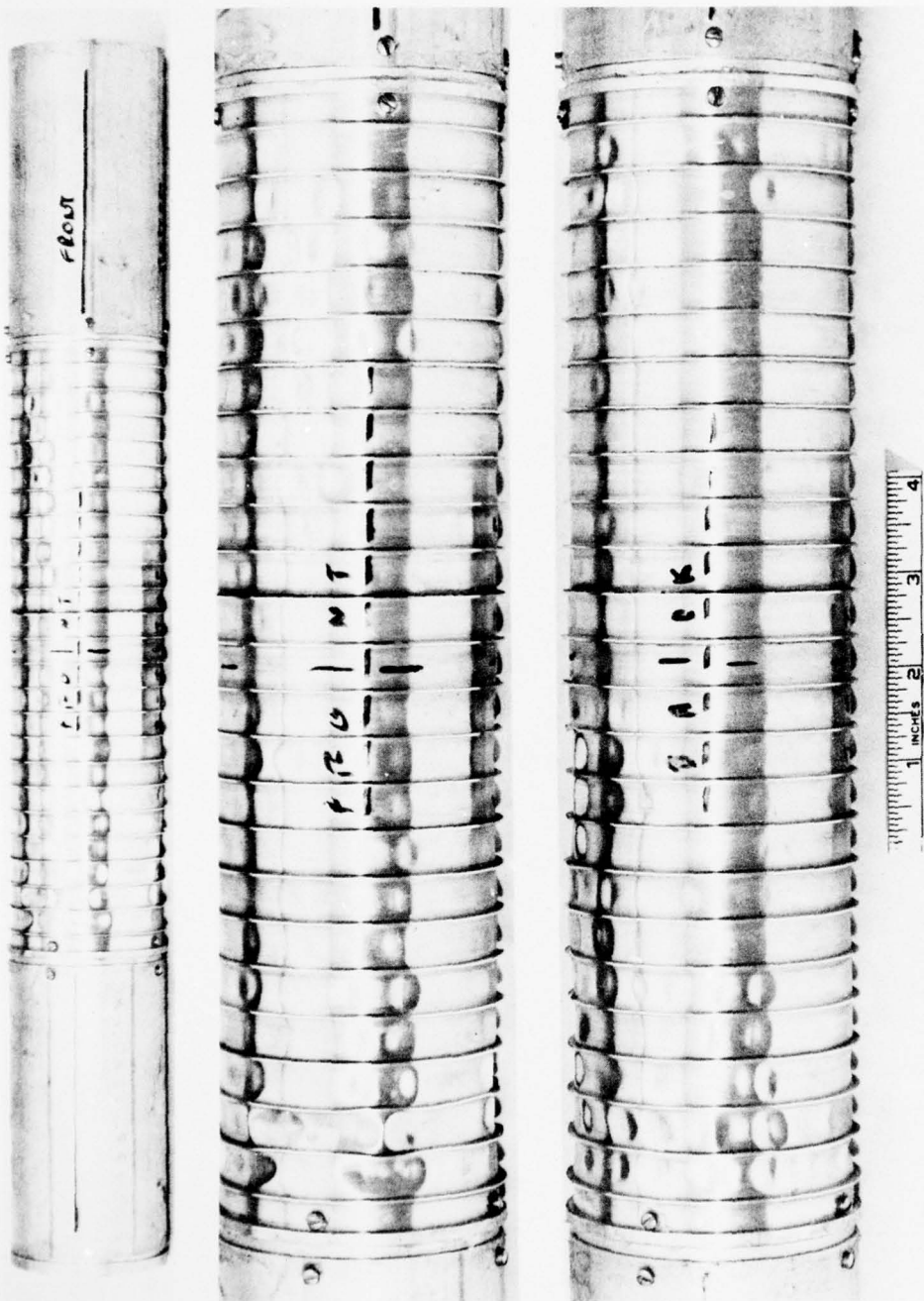
MP-1714-61

FIGURE 3.1 QUASI-STATIC OVERALL BUCKLING PRODUCED
BY AN UNDERWATER EXPLOSION (FIGURE 10b
OF REFERENCE 2)



MP-1714-62

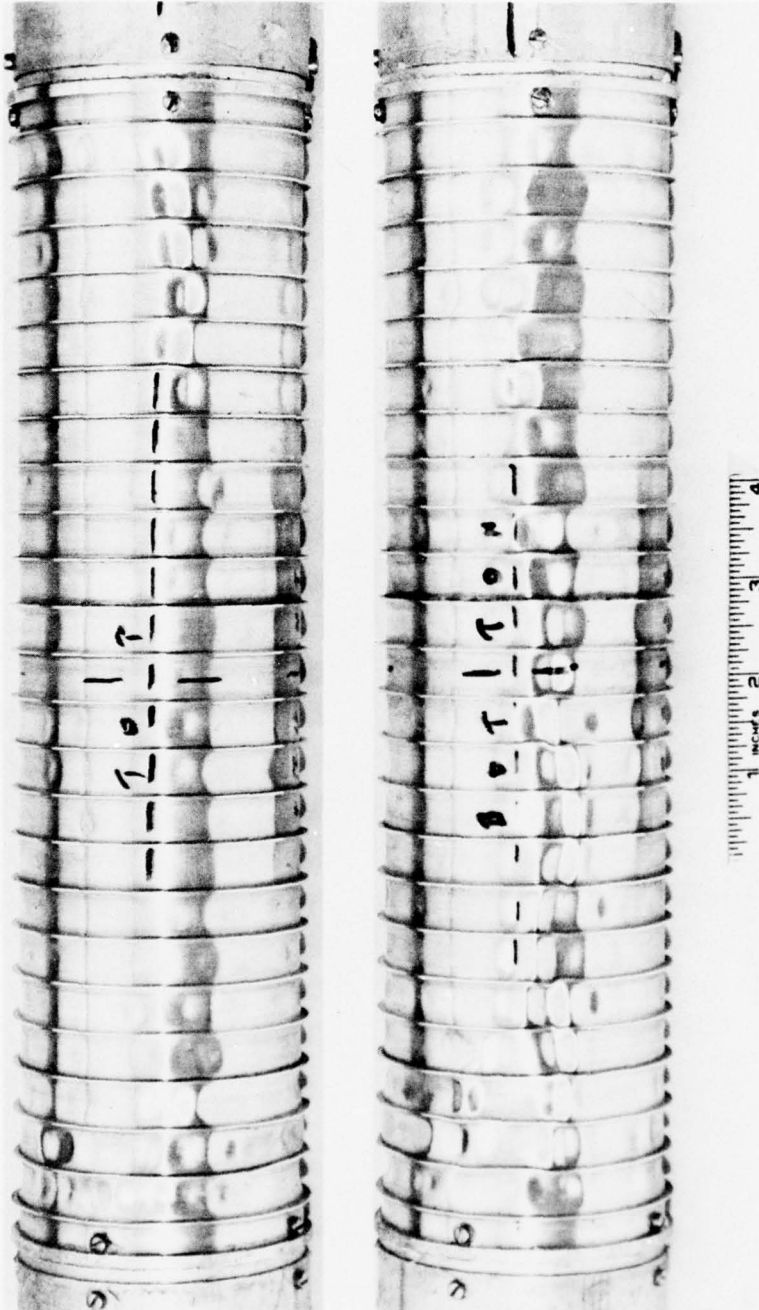
FIGURE 3.2 QUASI-STATIC OVERALL BUCKLING PRODUCED
BY A HYDROSTATIC LOAD (FIGURE 11 OF
REFERENCE 3)



(a) DYNAMIC PLATING BUCKLING PRODUCED BY AN UNDERWATER EXPLOSION—FRONT AND BACK VIEWS

MP-1714-63R

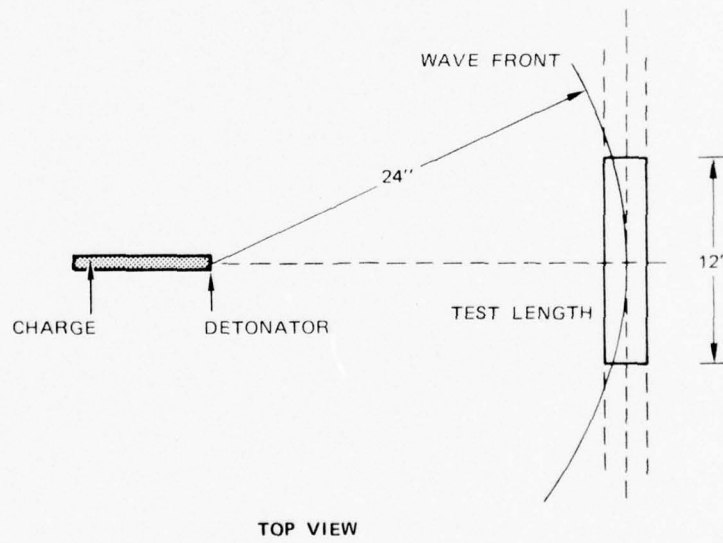
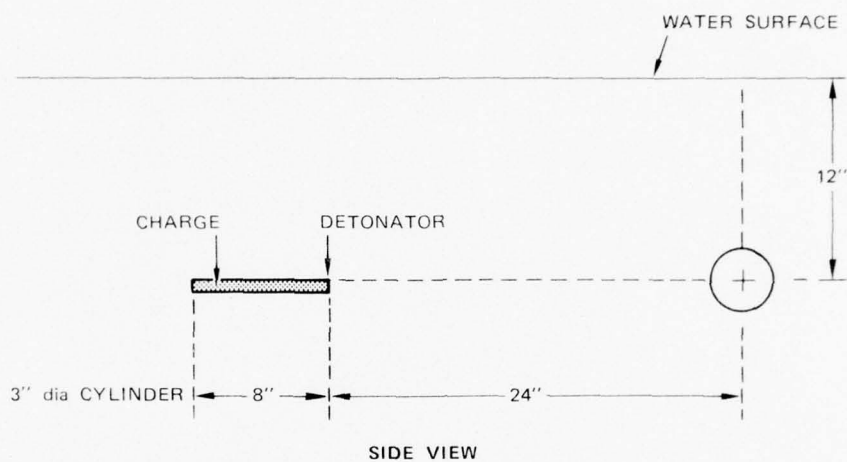
FIGURE 3.3



(b) DYNAMIC PLATING BUCKLING PRODUCED BY AN UNDERWATER EXPLOSION—TOP AND BOTTOM VIEWS

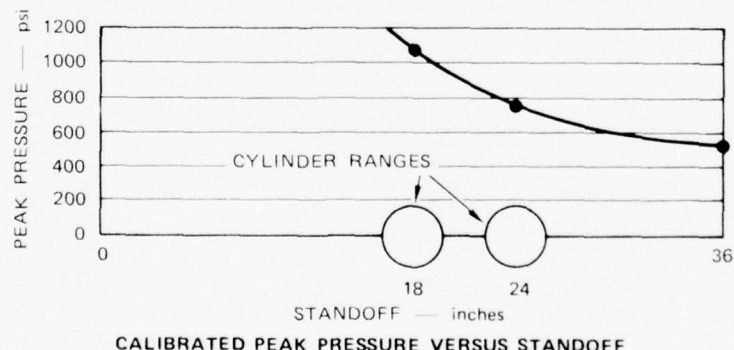
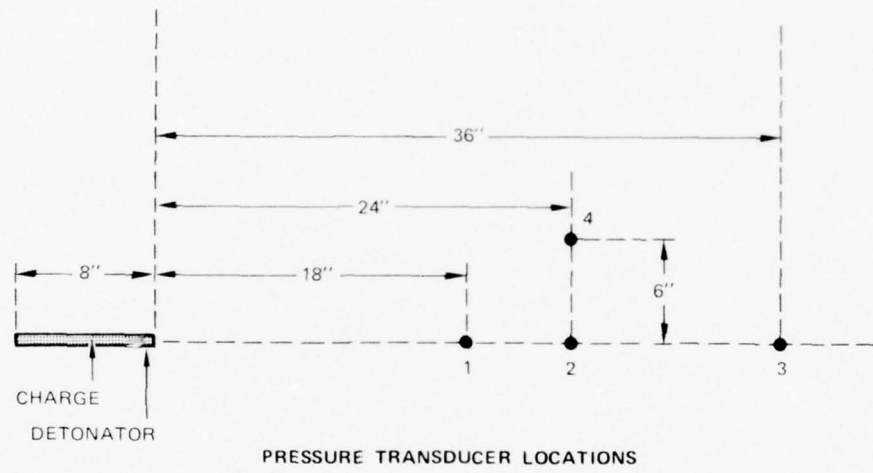
MP-1714-64R

FIGURE 3.3 (Continued)



(c) EXPERIMENTAL SETUP FOR MODEL OF FIGURES 3.3a AND b
MA-1714-33

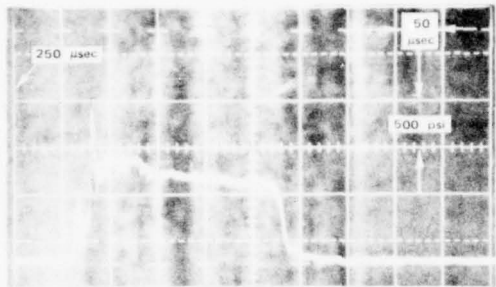
FIGURE 3.3 (Continued)



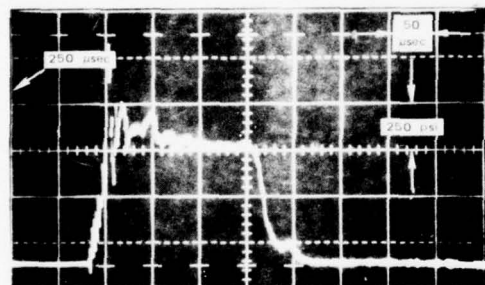
(d) RESULTS OF CHARGE CALIBRATION TESTS. MODEL OF FIGURES 3.3a AND b WAS AT 24-INCH RANGE. MODEL OF FIGURE 3.4 WAS AT 18-INCH RANGE.

MA-1714-34

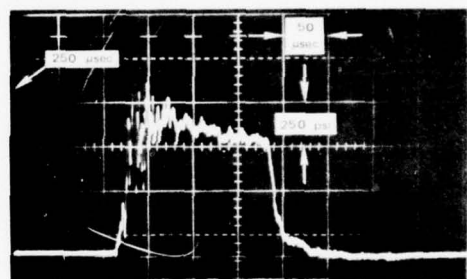
FIGURE 3.3 (Continued)



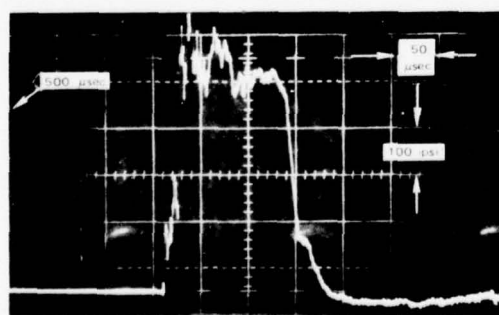
PRESSURE TRANSDUCER 1



PRESSURE TRANSDUCER 2



PRESSURE TRANSDUCER 4

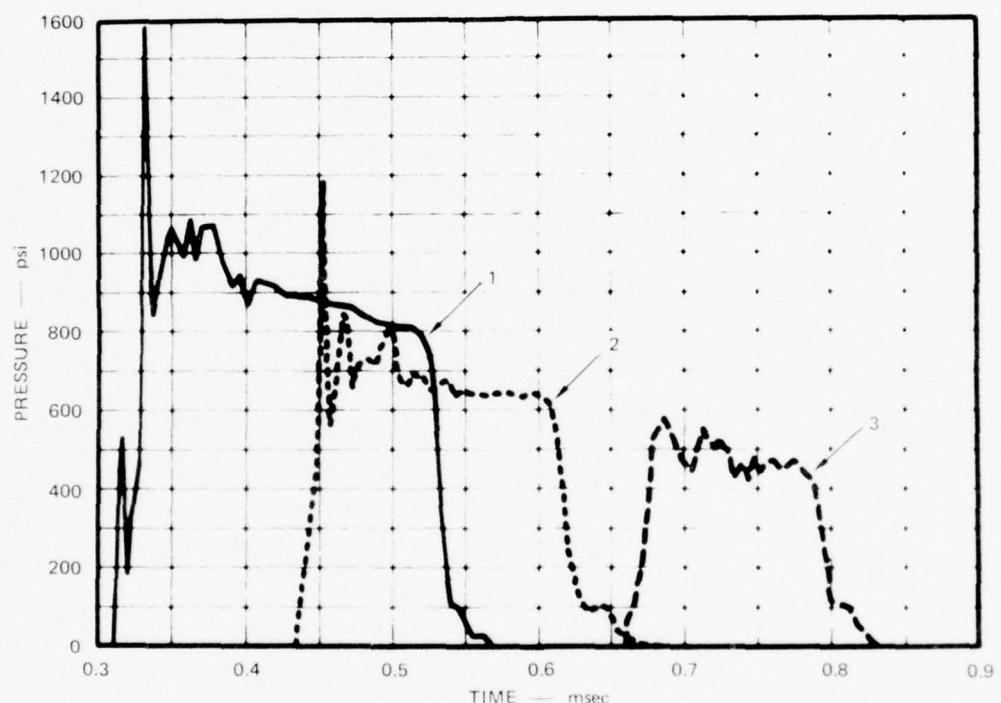


PRESSURE TRANSDUCER 3

(e) TYPICAL PRESSURE RECORDS FROM CHARGE CALIBRATION TESTS

MP-1714-31R

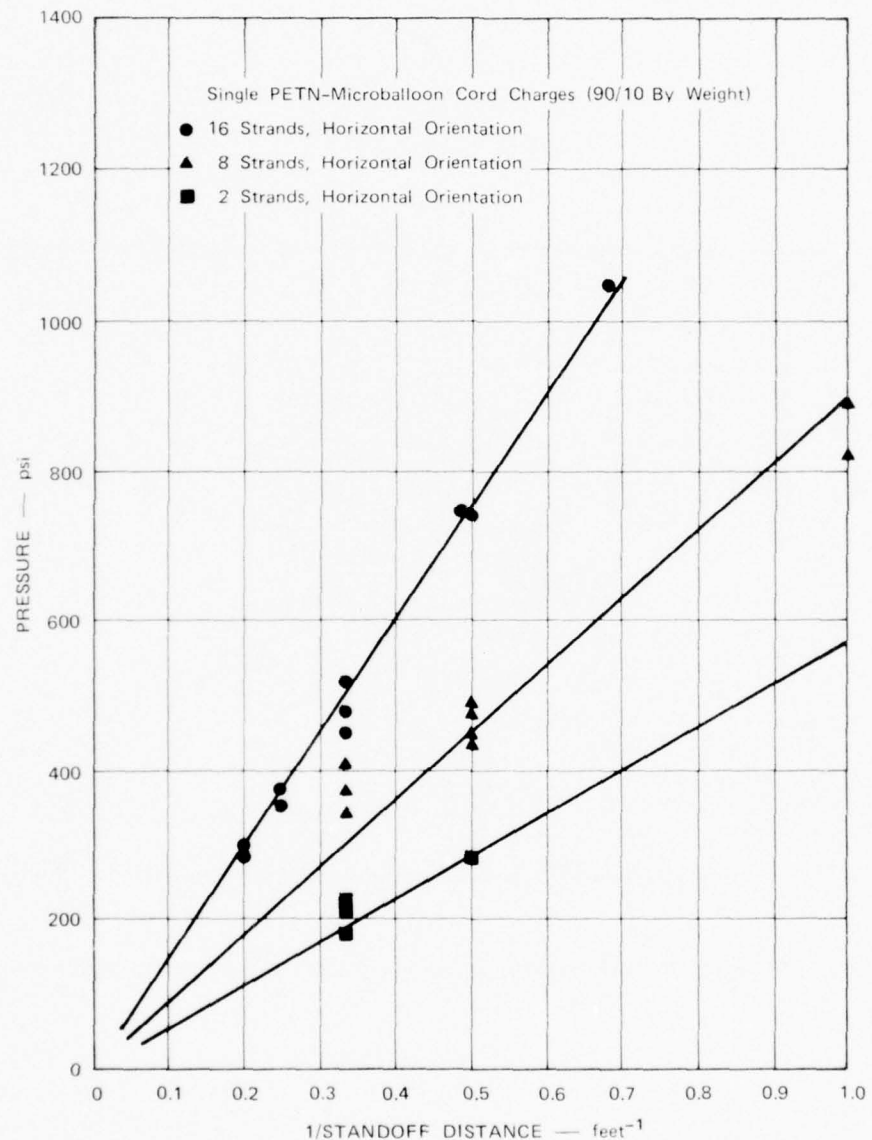
FIGURE 3.3 (Continued)



(f) PLOT OF PRESSURE PULSES FROM CHARGE CALIBRATION TESTS

MA-1714-32

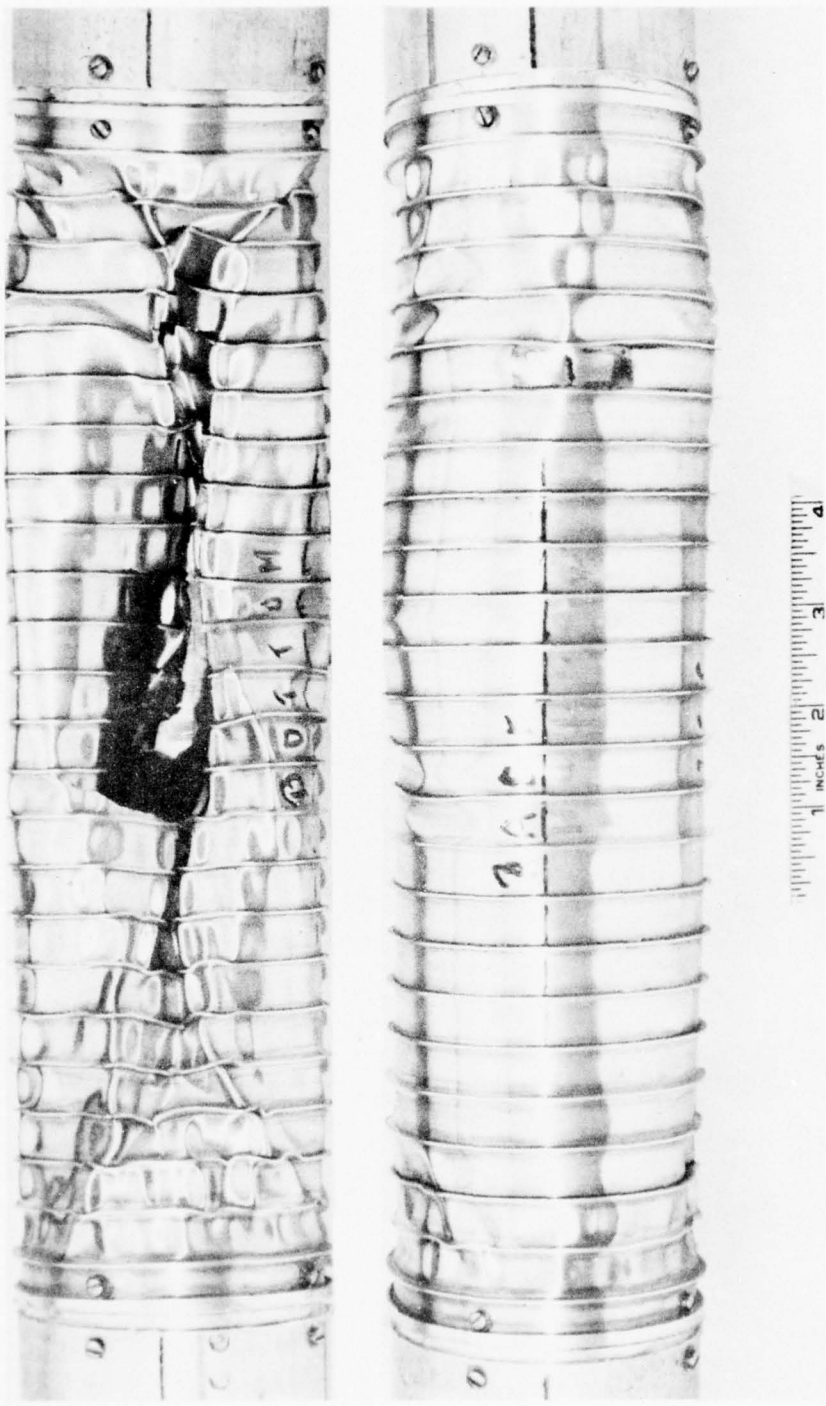
FIGURE 3.3 (Continued)



(g) UNDERWATER SHOCK WAVE PRESSURE VERSUS INVERSE OF STANDOFF DISTANCE FOR VARIOUS CHARGES

MA-3091-105A

FIGURE 3.3 (Concluded)



MP-1214-65

FIGURE 3.4 DYNAMIC OVERALL BUCKLING

See Figures 3.3c and d for experimental setup.



FIGURE 10c - MODEL LH-9 AFTER TEST 1-C
THE TOTAL PEAK PRESSURE WAS ABOUT THE SAME AS FOR LH-3 IN FIGURE 10a BUT THE DEPTH WAS GREATER BY 314 FT.

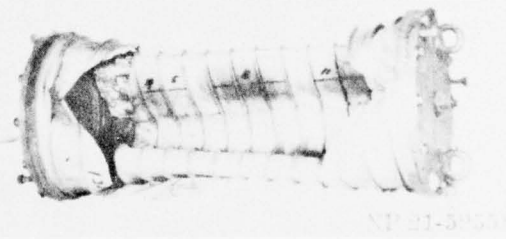
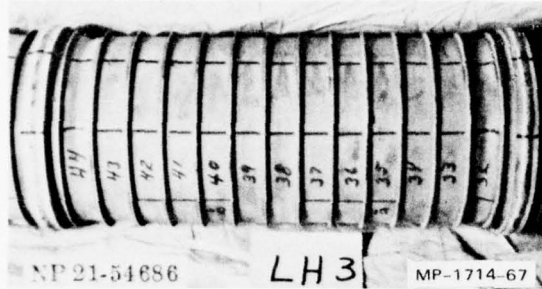


FIGURE 10f - MODEL U-5 AFTER TEST 2-C
THE INTERNAL LEAD KEEL IS VISIBLE. THE KEEL AND PART OF THE PLATING WERE ROTATED ABOUT ONE EDGE OF THE KEEL IN THIS TEST.

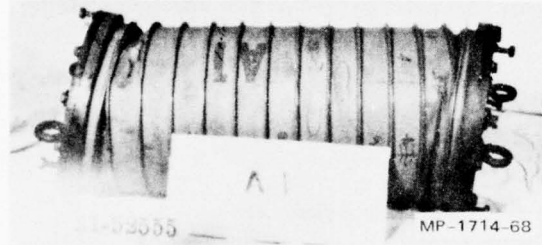
MP-1714-66

FIGURE 3.5 DYNAMIC OVERALL BUCKLING (FIGURES 10c AND 10f OF REFERENCE 2)



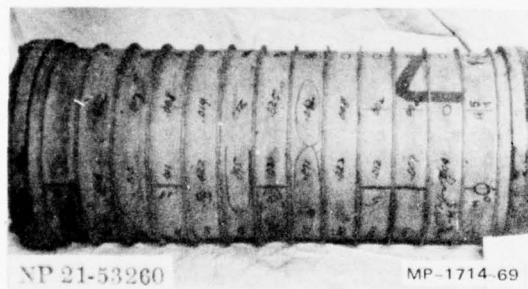
(a) FIGURE 10a - MODEL LH-3 AFTER TEST 2-B
NOTE DISHING OF SHELL AT ENDS OF
COMPARTMENT. THERE WAS MORE SEVERE
DISHING AT THE EXTREME ENDS OF THE
MODEL.

FIGURE 3.6 DYNAMIC PLATING BUCKLING DUE TO AXIAL LOAD
(FIGURE 10a OF REFERENCE 2)



(b) FIGURE 10e - MODEL A-1 AFTER TEST 2-C
THE DISHING AT THE ENDS IS MORE
EXAGGERATED THAN IN FIGURE 10a.

FIGURE 3.7 DYNAMIC PLATING BUCKLING DUE TO AXIAL LOAD
(FIGURE 10e OF REFERENCE 2)



(c) FIGURE 10d - MODEL SH-7
THE CENTRAL BAY SHOWS FAILURE
ASSOCIATED WITH SHIPPING. THERE ARE
LOBES IN ADJACENT BAYS.

FIGURE 3.8 DYNAMIC PLATING BUCKLING DUE TO OVERALL BENDING
(WHIPPING) (FIGURE 10d OF REFERENCE 2)

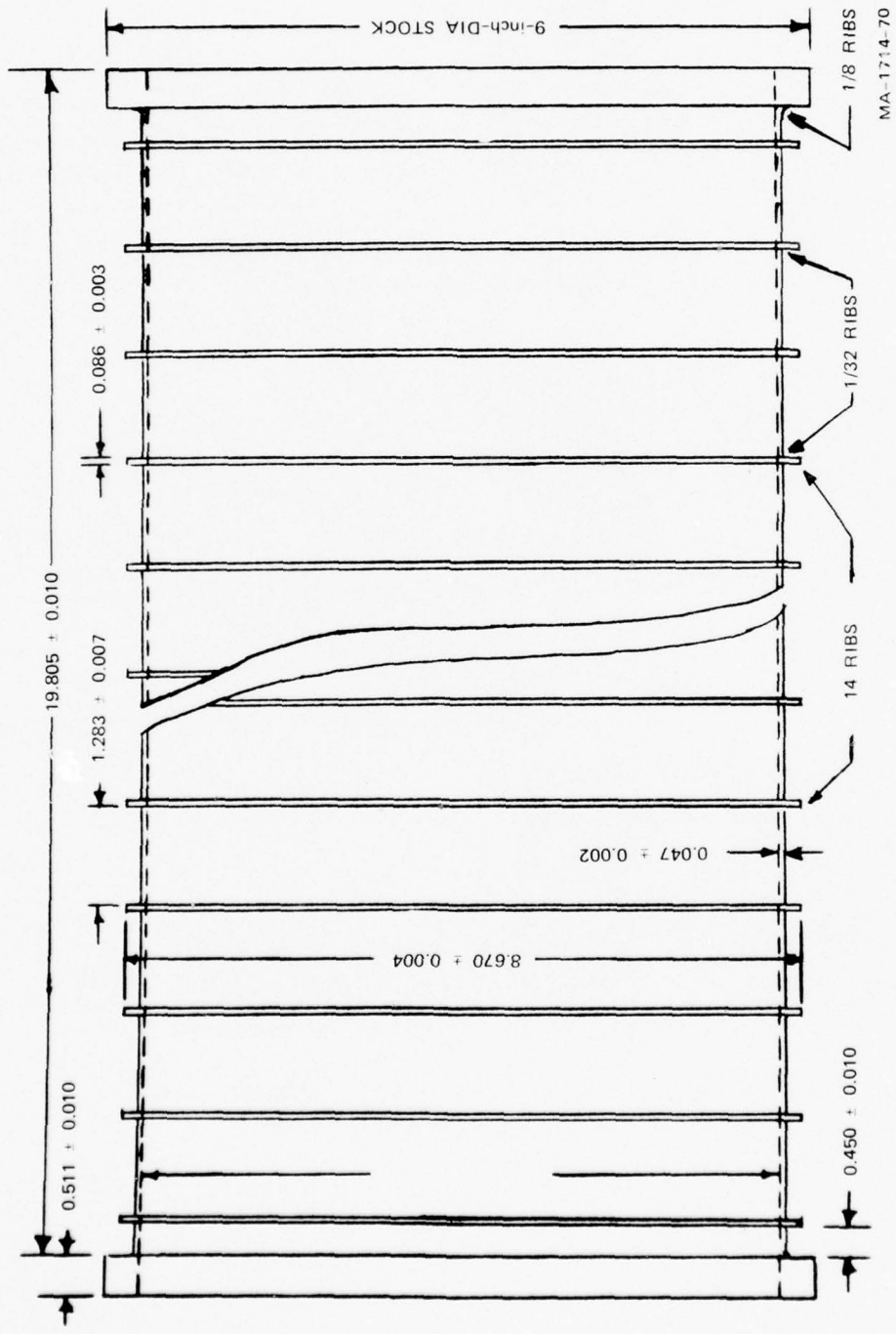
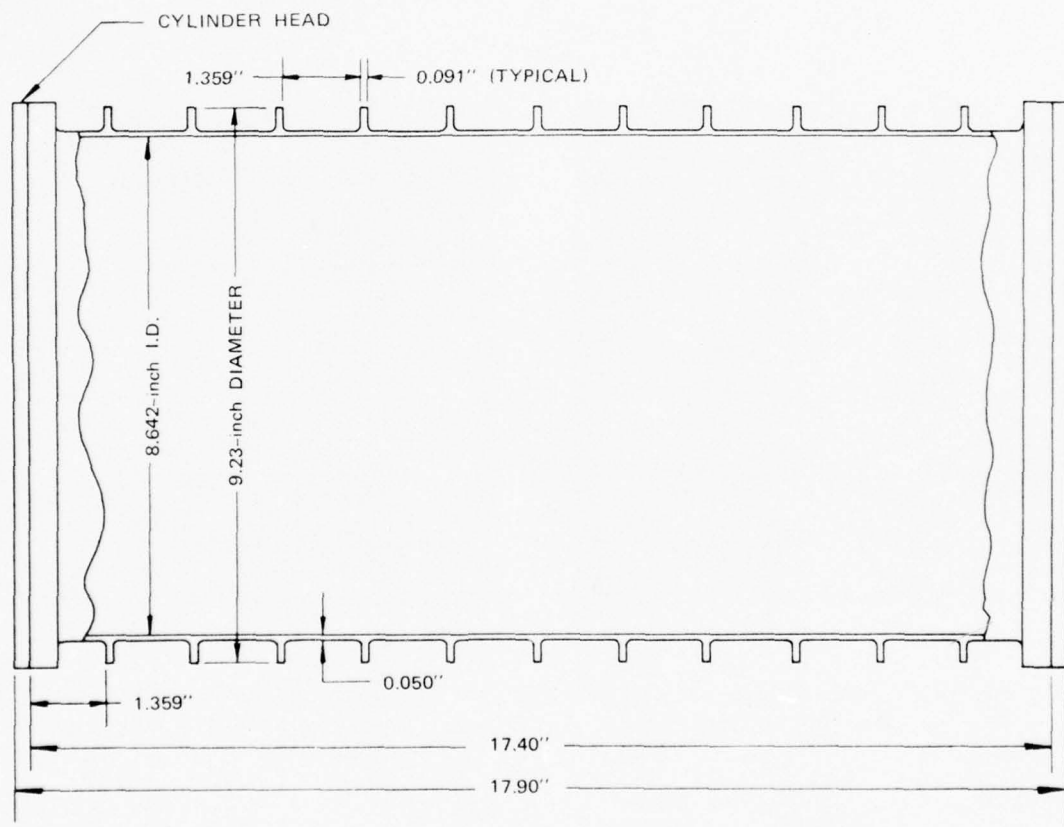
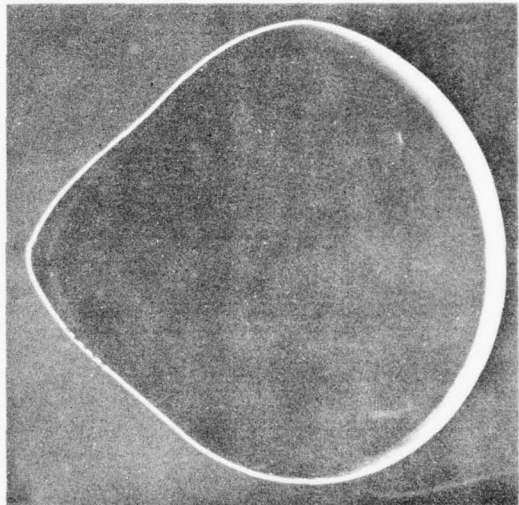
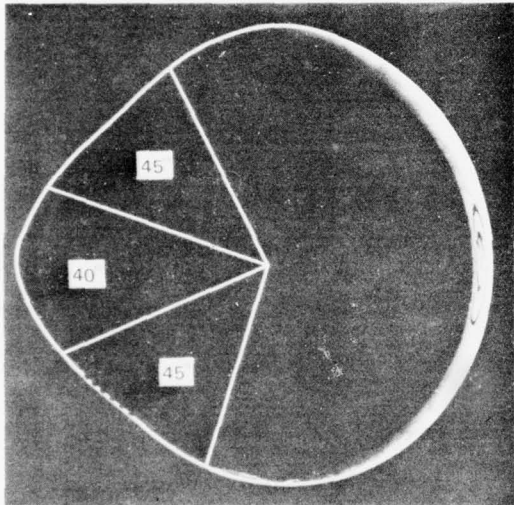


FIGURE 3.9 PRINCIPAL DIMENSIONS OF MODELS OF FIGURES 3.1 AND 3.5-3.8 (FIGURE 1 OF REFERENCE 2)



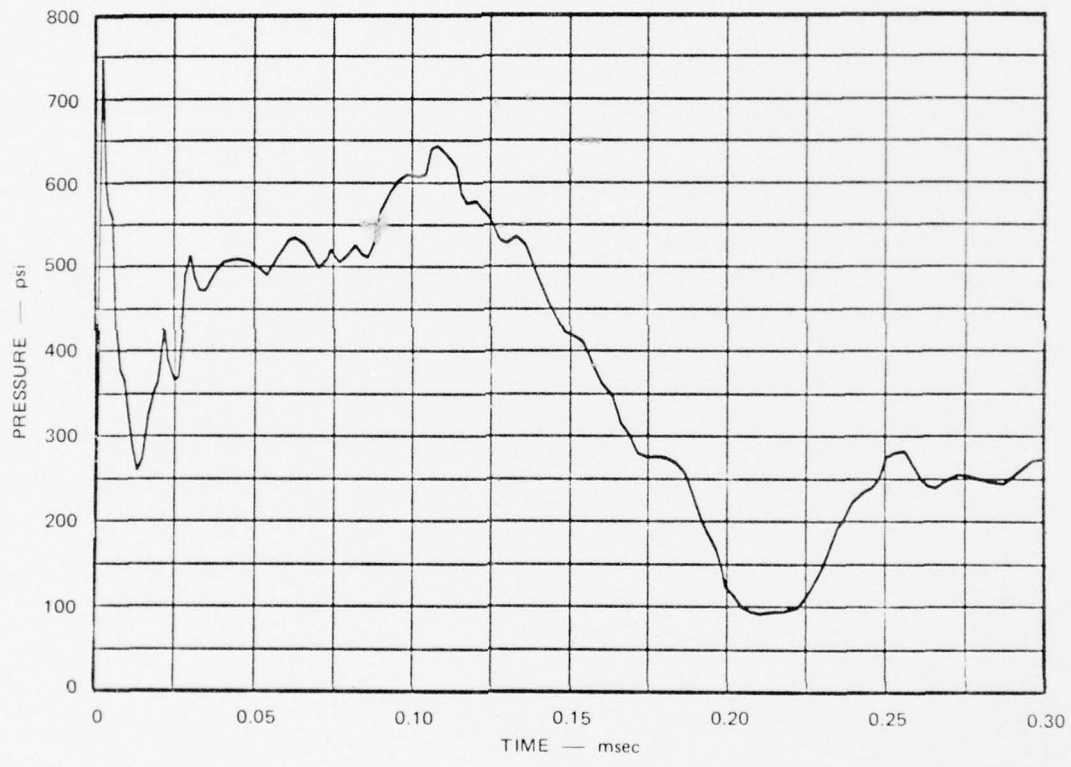
MA-1714-71

FIGURE 3.10 PRINCIPAL DIMENSIONS OF MODELS OF FIGURES 3.2-3.4 (FIGURE 1 OF REFERENCE 3)



MP-1714-72

FIGURE 3.11 DYNAMIC OVERALL BUCKLING OF UNIFORM SHELLS (AI 6061-T6, 3-INCH DIAMETER, 1/16-INCH WALL) PRODUCED BY UNDERWATER EXPLOSIONS



MA-1714-73

FIGURE 3.12 SURFACE PRESSURE AT POINT OF FIRST LOADING ON A MODEL LIKE THOSE OF FIGURE 3.11, AS MEASURED WITH A THIN FOIL (~1 mil) YTTERBIUM GAGE ATTACHED TO THE MODEL (REFERENCE 4)

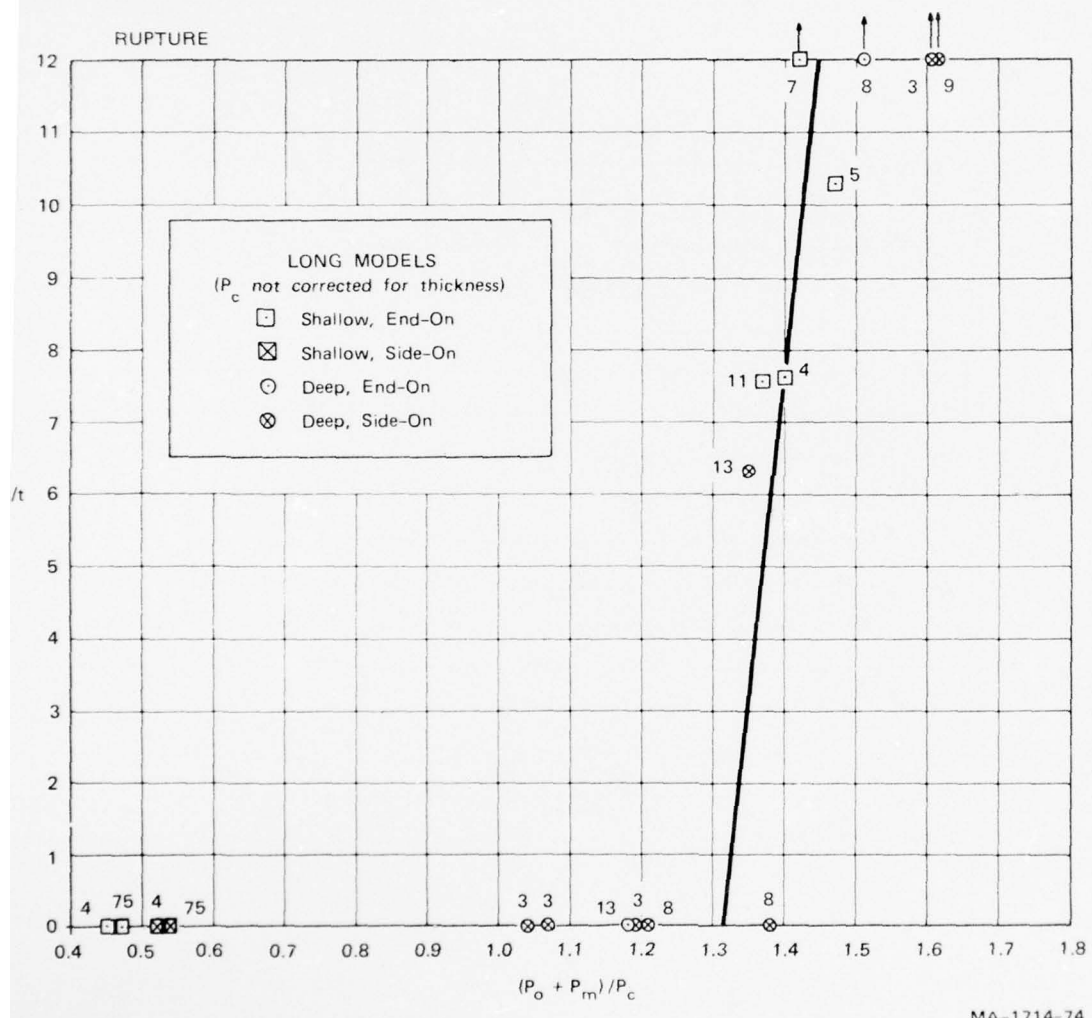


FIGURE 3.13 MAXIMUM PERMANENT DEFORMATION VERSUS RATIO OF TOTAL PEAK PRESSURE TO HYDROSTATIC COLLAPSE PRESSURE FOR MODELS OF SUBMARINE PRESSURE HULLS (FIGURE 9 OF REFERENCE 2)

4. BUCKLING THEORY OF SUBMERGED CYLINDRICAL SHELLS

4.1 BACKGROUND

Because catastrophic damage occurs when the cylindrical sheet and ring stiffeners buckle together, as shown in Figure 3.4(a) of Section 3, the theory was developed to describe overall buckling rather than the local buckling that consists only of sheet dimpling, shown in Figure 3.3(a). The theory describes buckling caused by a transverse incident pulse in water with specific results for a rectangular pulse (instantaneous rise, a constant pressure, and an instantaneous decay). The rectangular pulse is a reasonable idealization of a shock wave from a large underwater explosion, with surface cutoff.

The wavelengths observed in the experiments indicate that the predominant buckling mode forms during the initial elastic phase of deformation; thus this mode enters the initial conditions of the plastic phase and is consequently the preferred mode for further amplification. Therefore, the theoretical approach is to treat the initial response of the shell by elastic modal analysis until plasticity occurs in the hoop mode, and to use the displacement and velocity distributions at this time as initial conditions for the subsequent plastic response. Amplification of the preferred buckling mode is assumed to continue during the plastic phase until the membrane mode reaches the maximum inward radial displacement.

The buckling analysis is based on the dynamic pulse buckling theory developed at SRI over the past 15 years. The fluid-structure interaction is based on the Russian work by Mnev and Pertsev.⁵ The relevant parts of this work are included below to make the treatment complete. Appendix B summarizes the theory presented in this section in the form used for the

computations reported in Sections 5 and 6. Appendix B also includes several improved approximations.

4.2 GOVERNING EQUATION OF INITIAL ELASTIC PHASE

It is assumed that the cylindrical shell is long enough for a central portion to respond as an infinitely long shell. The theory is therefore planar and is described in polar coordinates r, θ .

Considering unit axial length regarded as a ring, the proportionality of moment and curvature change is

$$M = EI\kappa \quad (4.1)$$

where E is the elastic modulus of the shell material, I is the second moment of area of the ring cross section, and κ is the curvature increase corresponding to a radially inward displacement $w(\theta, t)$. The expression for κ is

$$\kappa = \frac{1}{a^2} \left(\frac{\partial^2 w}{\partial \theta^2} + w \right) \quad (4.2)$$

where a is the radius of the centroid of the ring cross sectional area.

Figure 4.1 shows a shell element at time t that has been displaced radially inwards a distance $w(\theta, t)$, shortened from an original length of $a d\theta$ to $d\lambda$, and bent so that the subtended angle changed from $d\theta$ to $d\phi$. These deformations were caused by the external pressure $p(\theta, t)$ and were resisted by the internal membrane thrust S , bending moment M , and shear force Q , along with the radial inertial force. As an approximation, the circumferential displacements and variations in S are neglected. Neglecting also the rotary inertia, the equations of motion of the element are

$$\frac{\partial Q}{\partial \lambda} + S \frac{\partial Q}{\partial \lambda} = -m \frac{\partial^2 w}{\partial t^2} + p \quad (4.3)$$

$$Q = \frac{\partial M}{\partial \lambda} \quad (4.4)$$

where m is the mass per unit arc length of shell. In (4.3), the curvature is

$$\frac{\partial \alpha}{\partial \lambda} = \frac{1}{a} + \kappa \quad (4.5)$$

A further approximation is made by setting $d\lambda = ad\theta$.

Equations (4.1) through (4.5) are now combined to produce the governing equation in the form

$$\frac{EI}{a^4} \left(\frac{\partial^4 w}{\partial \theta^4} + \frac{\partial^2 w}{\partial \theta^2} \right) + S \left[\frac{1}{a} + \frac{1}{a^2} \left(\frac{\partial^2 w}{\partial \theta^2} + w \right) \right] = -m \frac{\partial^2 w}{\partial t^2} + p \quad (4.6)$$

The thrust S is the product of the average circumferential compressive stress σ and the cross-sectional area A per unit length of shell. If H is the depth of the stiffener, as shown in the two cases in Figure 4.2, the area A may be expressed as

$$A = k \frac{H}{a}$$

$$k_a = (\zeta + \lambda - 1)\lambda\zeta \quad (4.7)$$

where $\zeta = H/h$ and $\lambda = L/\ell$. As indicated in Figure 4.2, L is the stiffener spacing, ℓ is the stiffener thickness, and h is the sheet thickness. Because the membrane stress is assumed to be approximately constant around the circumference at each instant, it follows that $\sigma_\theta = E\varepsilon_\theta = Ew_0/a$, where E is the elastic modulus, $\varepsilon_\theta = w_0/a$ is the

circumferential compressive membrane strain, and w_o is the average radially inward displacement. Thus

$$S = \frac{k_i H w_o}{a} \quad (4.8)$$

For the cross sections of Figure 4.2, the second moment of area may be expressed as

$$I = k_i^3 H^3 / 12$$

$$k_i = \left[\lambda (\zeta^4 + \lambda - 1) - (\lambda - 1)(\zeta - 1)^4 \right] / \lambda \zeta^3 (\zeta + \lambda - 1) \quad (4.9)$$

If the density of the shell material is ρ_s , the mass per unit length is

$$m = \rho_s A = \rho_s k_i H \quad (4.10)$$

By substitution of S , I , and m from (4.8), (4.9), and (4.10) into (4.6), the governing equation becomes

$$\frac{E k_i^3 H^3}{12a^4} \left(\frac{\partial^4 w}{\partial \theta^4} + \frac{\partial^2 w}{\partial \theta^2} \right) + \frac{E k_i H w_o}{a^2} \left[1 + \frac{1}{a} \left(\frac{\partial^2 w}{\partial \theta^2} + w \right) \right] = - \rho_s k_i H \frac{\partial^2 w}{\partial t^2} + p \quad (4.11)$$

Note that the coefficient w_o in this partial differential equation is a function of time, as is the pressure p .

As an algebraic simplification, dimensionless quantities are introduced according to Table 4.1, to put (4.11) in the form

$$\frac{\partial^2 w}{\partial t^2} + k_1 k_2 \left(\frac{\partial^4 w}{\partial \theta^4} + \frac{\partial^2 w}{\partial \theta^2} \right) + k_2 w_o \left(1 + \frac{\partial^2 w}{\partial \theta^2} + w \right) = \mu p \quad (4.12)$$

The final form of the governing equation can be obtained only by taking into account the dependence of the pressure on the response of the shell. This fluid-structure interaction is the subject of the next section.

4.3 FLUID-SHELL INTERACTION

In the work of Mnev and Pertsev,⁵ the pressure field in the fluid is considered as the superposition of three fields: (1) pressure in the undisturbed incident pulse, (2) pressure caused by diffraction of a fixed rigid cylinder, and (3) pressure caused by radiation from a deforming and translating cylinder. This superposition is justified in the following exposition.

Let ψ_d be the velocity potential for the diffraction field. Then, the particle velocity, pressure, and wave equation are,

$$v_d = \frac{\partial \psi_d}{\partial r} \quad p_d = -\frac{\partial \psi_d}{\partial t} \quad \nabla^2 \psi_d = \frac{\partial^2 \psi_d}{\partial t^2} \quad (4.13)$$

Let v_s be the radial component of velocity on a fixed unit circle ($r = 1$) associated with the passing undisturbed incident wave. For a fixed rigid cylinder to occupy the unit circle, the incident and diffraction fields must superimpose to provide no radial velocity on the unit circle; that is,

$$\frac{\partial \psi_d}{\partial r} + v_s = 0 \quad r = 1 \quad (4.14)$$

The solution of the cylindrical wave equation in (4.13), satisfying the boundary condition (4.14) on the unit circle and the condition $\psi_d \rightarrow 0$ as $r \rightarrow \infty$ (initial conditions $\psi_d = 0, \partial \psi_d / \partial t = 0$) may be found by a Laplace transformation with respect to time t and separation of variables with respect to the polar coordinates r, θ .

If the radial component of the velocity in the incident wave at the unit circle has the Fourier representation

$$v_s = \sum_{n=0}^{\infty} b_n(t) \cos n\theta \quad r = 1 \quad (4.15)$$

the Laplace transform of the diffraction field velocity potential is

$$\psi_d^L = \sum_{n=0}^{\infty} \frac{b_n^L K_n(r s) \cos n\theta}{K_n(s) \left[n + \frac{s K_{n-1}(s)}{K_n(s)} \right]} \quad (4.16)$$

In (4.16), s is the transform parameter and $K_n(s)$ is a modified Bessel function of the second kind of order n and argument s . Transforming the pressure formula in (4.13) gives $p_d^L = -s \psi_d^L$ and hence, by (4.16),

$$p_d^L = - \sum_{n=0}^{\infty} s b_n^L m_n \cos n\theta \quad r = 1 \quad (4.17)$$

where

$$m_n = \left[n + \frac{s K_{n-1}(s)}{K_n(s)} \right]^{-1} = - \frac{K_n(s)}{s K'_n(s)} \quad (4.18)$$

If the incident wave pressure evaluated on the unit circle is

$$p_s^o = \sum_{n=0}^{\infty} a_n \cos n\theta \quad r = 1 \quad (4.19)$$

and the pressure distribution on the fixed, rigid cylinder is

$$p^o = p_s^o + p_d^L = \sum_{n=0}^{\infty} p_n^o \cos n\theta \quad r = 1 \quad (4.20)$$

it follows that

$$p^{OL} = p_s^L + p_d^L = \sum_{n=0}^{\infty} \left(a_n^L - s b_n^L \right) \cos n\theta \quad (4.21)$$

and

$$p_n^L = a_n^L - s b_n^L \quad (4.22)$$

Inversion of (4.22) provides the exact solution for the pressure on a fixed, rigid cylinder subjected to a transverse pressure pulse, but it is more fruitful to employ the approximate method to be described.

Let φ_r be the velocity potential for the radiation field. Then,

$$v_r = \frac{\partial \varphi}{\partial r} \quad p_r = - \frac{\partial \varphi}{\partial t} \quad \partial_r^2 \varphi = \frac{\partial^2 \varphi}{\partial t^2} \quad (4.23)$$

Recalling that the radially inward displacement of the deformable shell boundary of the fluid is $w(\theta, t)$, the boundary condition to be satisfied by φ_r is

$$\frac{\partial \varphi}{\partial r} + \frac{\partial w}{\partial t} = 0 \quad r = 1 \quad (4.24)$$

If the shell displacement is given the Fourier representation

$$w = \sum_{n=0}^{\infty} w_n \cos n\theta \quad (4.25)$$

the transformed boundary condition (4.24), with the initial condition $w(\theta, 0) = 0$, is

$$\frac{\partial \varphi^L}{\partial r} = - \sum_{n=0}^{\infty} s w_n^L \cos n\theta \quad (4.25)$$

The solution of the cylindrical wave equation of (4.23) satisfying the boundary condition (4.24) on the unit circle and the condition $\varphi_r \rightarrow 0$ as $r \rightarrow \infty$ (initial conditions $\varphi_r = 0$, $\partial\varphi_r/\partial t = 0$) may be found by a Laplace transformation with respect to time t and separation of variables with respect to the polar coordinates r, θ . This procedure leads to the transformed radiation velocity potential

$$\varphi_r^L = \sum_{n=0}^{\infty} \frac{s w_n^L K_n(rs) \cos n\theta}{K_n(s) \left[n + \frac{s K_{n-1}(s)}{K_n(s)} \right]} \quad (4.26)$$

Transforming the pressure formula in (4.23) gives $p^{rL} = -s \varphi_r^L$ and hence, by (4.26)

$$p^{rL} = - \sum_{n=0}^{\infty} s^2 w_n^L m_n \cos n\theta \quad r = 1 \quad (4.27)$$

where m_n is defined by (4.18). If the radiation pressure is given the representation

$$p^r = - \sum_{n=0}^{\infty} p_n^r \cos n\theta \quad r = 1 \quad (4.28)$$

it follows that

$$p^{rL} = - \sum_{n=0}^{\infty} p_n^{rL} \cos n\theta \quad r = 1 \quad (4.29)$$

and, by (4.27),

$$p_n^{rL} = s^2 w_n^L m_n \quad (4.30)$$

Introducing the function $\psi_n(s)$ defined by

$$\psi_n^L(s) = m_n(s) \quad (4.31)$$

expression (4.30) becomes

$$p_n^{rL} = s^2 w_n^L \psi_n^L \quad (4.32)$$

With initial conditions $w_n(0) = 0$ and $\dot{w}_n(0) = 0$, where a dot denotes time differentiation, the transform of each shell acceleration component is

$$s^2 w_n^L = \int_0^\infty \ddot{w}_n(t) e^{-st} dt$$

so that, by applying the convolution theorem of transforms, (4.32) can be inverted to give the radiation pressure components

$$p_n^r = \int_0^t \ddot{w}_n(\tau) \psi_n^L(t - \tau) d\tau \quad (4.33)$$

A physical interpretation can be given to the function ψ_n if we consider the unit step velocity in the n^{th} mode of deflection, $\dot{w}_n(t) = H(t)$, where $H(t)$ is the unit step function ($H = 0$ for $t < 0$ and $H = 1$ for $t > 0$). Thus, $w_n(t) = tH(t)$ and $w_n^L(s) = s^{-2}$, which, by (4.32) gives $p_n^{rL} = \psi_n^L$. Thus $\psi_n^L = p_n^r$ is the radiation pressure associated with the n^{th} mode for a shell moving at unit velocity. The function ψ_n^L is called the unit function of resistance. Other properties of $\psi_n^L(t)$ are $\psi_n^L(0) = 1$, $\psi_n^L(\infty) = 0$, and

$$\int_0^\infty \psi_n(t) dt = \frac{1}{n} \quad (4.34)$$

This last result can be shown⁵ to be the apparent addition mass during motion of a shell in an incompressible fluid.

The unit function of resistance can also be introduced into (4.22) for the transform of the diffraction pressure components so that

$$p_n^{oL} = a_n^L - s b_n^L \psi_n^L \quad (4.35)$$

Inversion of (4.35) gives

$$p_n^o = a_n^o(t) - b_n^o(t) - \int_0^t b_n^o(\tau) \dot{\psi}_n^L(t-\tau) d\tau \quad (4.36)$$

The first step in the solution of equation (4.12) is to set

$$p = P p^o + p^r \quad (4.37)$$

where P is a number that determines the pressure in the incident pulse. For $P = 1$ the pressure equals the bulk modulus of water, so the values of P that are of interest are $O(10^{-3})$. The second step is to give w , p^o , and p^r their Fourier series representations (4.25), (4.20), and (4.28). Equating coefficients of $\cos n\theta$ then gives an infinite set of ordinary differential equations. The third step is to approximate the functions ψ_n in the pressure coefficients (4.33) and (4.36) and to evaluate the pressure and velocity coefficients a_n and b_n for the given incident pulse.

4.4 APPROXIMATE UNIT RESISTANCE FUNCTIONS

Approximate unit resistance functions are needed because the exact functions are inconvenient to use in analysis. The choice of the approximate functions ψ_n is based on knowledge of the exact functions (obtained numerically for the lower modes), general properties, and the need for an analytically tractable form. The approximate functions chosen to represent the exact functions

$$\psi_0(t) = \begin{cases} (1 - a) + a e^{-t/2a} & a = 0.85, t \leq 8 \\ 0 & t > 8 \end{cases} \quad (4.38)$$

$$\psi_n(t) = \left(1 - \frac{n}{2}t\right) \left[1 - H\left(t - \frac{2}{n}\right)\right] \quad n \geq 1 \quad (4.39)$$

These are compared with the exact functions for $n = 0, 1$, and 2 in Figure 4.3. An improved version of ψ_1 is also shown and is used in Appendix B.

The functions (4.39) are approximations in the form of two straight lines and satisfy the conditions $\psi_n(0) = 0$, $\psi_n(\infty) = 0$, and (4.34). The function (4.38) is special because two straight lines do not form an adequate approximation for the important hoop mode; $\psi_0(0) = 1$ but $\psi_0(\infty) = 1 - a$, so a limiting time of applicability of $t \leq 8$ is suggested; when $t > 8$, set $\psi_0 = 0$.

Substitution of ψ_0 in (4.36) and (4.33) gives the hoop mode pressure coefficients

$$p_0^o = a_o - b_o + \frac{1}{2} \int_0^t b_o(\tau) e^{-(t-\tau)/2a} d\tau \quad (4.40)$$

$$p_0^r = \dot{w}_o - \frac{1}{2} w_o + \frac{1}{4a} \int_0^t w_o(\tau) e^{-(t-\tau)/2a} d\tau \quad (4.41)$$

and substitution of ψ_n in (4.36) and (4.33) gives the other pressure coefficients.

$$p_n^o = a_n - b_n + \frac{n}{2} \int_0^t b_n(\tau) d\tau \quad n \geq 1 \quad (4.42)$$

$$(t - \frac{2}{n}) H(t - \frac{2}{n})$$

$$p_n^r = \alpha_n w_n + \beta_n \dot{w}_n + \gamma \ddot{w}_{nn} \quad n \geq 1 \quad (4.43)$$

where

$$\left. \begin{aligned} \alpha_n &= -\frac{n}{2} \left[1 - H\left(t - \frac{2}{n}\right) \right] \\ \beta_n &= 1 - H\left(t - \frac{2}{n}\right) \\ \gamma_n &= \frac{1}{n} H\left(t - \frac{2}{n}\right) \end{aligned} \right\} \quad (4.44)$$

Improved formulas for p_0^o and p_1^o are presented in Appendix B.

4.5 REPRESENTATION OF A RECTANGULAR PULSE

With the aid of Figure 4.4, it is seen that a rectangular incident pulse may be represented by the formula

$$p_s = H(t - 1 + \cos\theta) - H(t - 1 + \cos\theta) \quad (4.45)$$

the time origin being when the wave front first contacts the unit circle. In (4.45) the first term represents step loading and the second term represents step unloading after a duration T . The

corresponding particle velocity resolved along the outward normal of the unit circle is

$$v_s = -\cos\theta[H(t - 1 + \cos\theta) - H(t - T - 1 + \cos\theta)] \quad (4.46)$$

In the series representations (4.19) and (4.15) for p_s and v_s the coefficients are

$$a_0 = \frac{1}{\pi} \int_0^\pi p_s d\theta \quad a_n = \int_0^\pi p_s \cos n\theta d\theta \quad n \geq 1 \quad (4.47)$$

$$b_0 = \frac{1}{\pi} \int_0^\pi v_s d\theta \quad b_n = \frac{2}{\pi} \int_0^\pi v_s \cos n\theta d\theta \quad n \geq 1 \quad (4.48)$$

Substituting (4.45) and (4.46) for p_s and v_s in the integrals (4.47) and (4.48) and carrying out the integration give

$$\begin{aligned} a_0 &= a'_0 [H(t) - H(t - 2)] + H(t - 2) \\ &\quad + a''_n [H(t - T) - H(t - T - 2)] - H(t - T - 2) \\ a_n &= a'_n [H(t) - H(t - 2)] + a''_n [H(t - T) \\ &\quad - H(t - T - 2)] \end{aligned} \quad n \geq 1 \quad (4.49)$$

$$b_0 = b'_0 [H(t) - H(t - 2)] + b''_0 [H(t - T) - H(t - T - 2)]$$

$$b_1 = b'_1 [H(t) - H(t - 2)] - H(t - 2) + b''_1 [H(t - T)$$

$$- H(t - T - 2)] + H(t - T - 2)$$

$$b_n = b'_n [H(t) - H(t - 2)] + b''_n [H(t - T) - H(t - T - 2)]$$

where

$$a'_0 = \frac{\theta_0}{\pi} \quad a'_n = \frac{2}{\pi n} \sin n\theta_0 \quad n \geq 1$$

$$b'_0 = -\frac{1}{\pi} \sin \theta_0 \quad b'_1 = -\frac{1}{\pi} (\theta_0 + \frac{1}{2} \sin 2\theta_0)$$

$$b'_n = -\frac{1}{\pi} \left[\frac{1}{n+1} \sin(n+1)\theta_0 + \frac{1}{n-1} \sin(n-1)\theta_0 \right] \quad n \geq 2$$

$$a''_0 = -\frac{\theta_1}{\pi}$$

$$a''_n = -\frac{2}{\pi n} \sin n\theta_1 \quad n \geq 1$$

$$b''_0 = \frac{1}{\pi} \sin \theta_1 \quad b''_1 = \frac{1}{\pi} (\theta_1 + \frac{1}{2} \sin 2\theta_1)$$

$$b''_n = \frac{1}{\pi} \left[\frac{1}{n+1} \sin(n+1)\theta_1 + \frac{1}{n-1} \sin(n-1)\theta_1 \right] \quad n \geq 2$$

$$\cos \theta_0 = 1 - t \quad \cos \theta_1 = 1 - (t - T)$$

As shown in Figure 4.4, θ_0 and θ_1 are the angles subtended by the wave front and wave rear.

4.6 SYSTEM OF GOVERNING EQUATIONS OF ELASTIC PHASE

After substituting the series representations (4.25), (4.20), and (4.28) for w , p^o , and p^r in the governing equation (4.12) and equating to zero the coefficients of each $\cos n\theta$, we obtain the following system of equations:

$$\ddot{w}_0 + k_2 w_0 = \mu (P p_0^o - p_0^r) \quad (4.50)$$

$$\ddot{w}_n + k_2 (n^2 - 1) (k_1 n^2 - w_0^2) w_n = \mu (P p_n^o - p_n^r) \quad n \geq 1 \quad (4.51)$$

To obtain (4.50) it is assumed that $w_o \ll 1$ (hoop displacement small compared with shell radius). Introducing in (4.50) and (4.51) the radiation pressure coefficients (4.41) and (4.43) results in the equations

$$\ddot{w}_o + \mu \dot{w}_o + (k_2 - \mu/2)w_o = \mu P p_0^o \quad (4.52)$$

$$(1 + \mu \gamma_n) \ddot{w}_n + \mu \beta_n \dot{w}_n + [k_2(n^2 - 1)(k_1 n^2 - w_o^2) + \mu \alpha_n] w_n = \mu P p_n^o \quad n \geq 1 \quad (4.53)$$

To obtain (4.52), we neglect the last term of (4.41) (this term is retained in the summary of Appendix B). The accompanying initial conditions are

$$w_n(0) = 0 \quad \dot{w}_n(0) = 0 \quad n \geq 0 \quad (4.54)$$

4.7 SOLUTION OF GOVERNING EQUATIONS OF ELASTIC PHASE

The solution of (4.52) for the hoop mode with initial conditions (4.54) is

$$w_o = \frac{\mu P}{\nu} \int_0^t \left(e^{s_1(t-\tau)} - e^{s_2(t-\tau)} \right) p_0^o(\tau) d\tau \quad (4.55)$$

where

$$s_1 = (\nu - \mu)/2$$

$$s_2 = -(\nu + \mu)/2$$

$$\nu = s_1 - s_2 = [\mu^2 - 4(k_2 - \mu/2)]^{1/2}$$

The first equation of the set (4.53) governing shell translation is

$$(1 + \mu \gamma_1) \ddot{w}_1 + \mu \beta_1 \dot{w}_1 + \mu \alpha_1 w_1 = \mu P p_1^o \quad (4.56)$$

and formulas (4.44) give the coefficients

$$\alpha_1 = -\frac{1}{2} \quad \beta_1 = 1 \quad \gamma_1 = 0 \quad \text{for } t \leq 2$$

and

$$\alpha_1 = 0 \quad \beta_1 = 0 \quad \gamma_1 = 1 \quad \text{for } t \geq 2$$

Hence equation (4.56) is replaced by the following two equations:

$$\ddot{w}_1 + \mu \dot{w}_1 - (\mu/2) w_1 = \mu P p_1^o \quad t \leq 2 \quad (4.57)$$

$$(1 + \mu) \ddot{w}_1 = \mu P p_1^o \quad t \geq 2 \quad (4.58)$$

The solution of (4.57) with initial conditions $w_1(0) = 0$ and $\dot{w}_1(0) = 0$ is

$$w_1 = \frac{\mu P}{\nu} \int_0^t (e^{s_1(t-\tau)} - e^{s_2(t-\tau)}) p_1^o(\tau) d\tau \quad t \leq 2 \quad (4.59)$$

where

$$s_1 = (\nu - \mu)/2$$

$$s_2 = -(\nu + \mu)/2$$

$$\nu = s_1 - s_2 = (\mu^2 + 2\mu)^{1/2}$$

The solution of (4.58) is

$$w_1 = w_1(2) + (t - 2)\dot{w}_1(2) + \frac{\mu P}{1+\mu} \int_2^t \int_2^\tau p_1^o(\eta) d\eta d\tau \quad t \geq 2 \quad (4.60)$$

The remaining equations of the set (4.53), with $w_o(t)$ given by (4.55), are solved by numerical methods [the translational mode $n = 1$ may also be solved numerically instead of by (4.59) and (4.60)].

The dimensionless radially inward displacement w_o of (4.55) is the same as the hoop compressive strain ϵ_θ . An approximation to the time at which the elastic deformation phase ends is that value \bar{t} at which w_o of (4.55) equals the compressive yield strain ϵ_y of the shell material; expressed mathematically

$$w_o(\bar{t}) = \bar{w}_o = \epsilon_y \quad (4.61)$$

At time \bar{t} , the radially inward velocity, $\dot{w}_o(t) = \bar{v}_o$, in the hoop mode is, by differentiation of (4.55)

$$\bar{v}_o = \frac{\mu P}{\nu} \int_0^{\bar{t}} (s_1 e^{s_1(\bar{t}-\tau)} - s_2 e^{s_2(\bar{t}-\tau)}) p_0^o(\tau) d\tau \quad (4.62)$$

with $s_1 = (\nu - \mu)/2$, $s_2 = (\nu + \mu)/2$, and $\nu = s_1 - s_2 = [\mu^2 - 4(k_2 - \mu/2)]^{1/2}$.

For the buckling modes, equations (4.53) are solved numerically because of the time dependent coefficient of w_n (an analytical solution is, of course, possible if w_o can be neglected in the coefficient).

The initial conditions for the plastic phase of deformation are

$$w_n(\bar{t}) = \bar{w}_n \quad \dot{w}_n(\bar{t}) = v_n \quad n \geq 1 \quad (4.63)$$

4.8 GOVERNING EQUATION OF THE PLASTIC PHASE

As a simplified description of the complicated plastic response, buckling is taken to occur in accordance with the Shanley or tangent modulus theory.⁶ In this theory, it is supposed that the membrane and bending strains combine to produce no strain rate reversal on the shell cross section. Thus, while the compressive hoop strain increases, the accompanying curvature increase should not be excessive. Experiments imply conformity with this condition during the earlier part of the plastic phase because low buckling modes are observed (see Figure 3.11). Strain rate reversal does occur in the later part of the plastic phase because eventually large curvatures develop. Use of the tangent modulus theory leads to an overprediction of the buckling amplitude because the resistive moment is much higher when strain rate reversal occurs; however, this is not considered a serious handicap of the theory. The advantage of the theory is that it allows a simple analytical treatment leading to conservative results from a defensive viewpoint.

The theoretical development here is also based on geometrical linearity, that is, relatively small displacements and strain ($\gtrsim 10$ percent). To obtain the simplest possible theory, we use a constant tangent modulus E_h ; a variable E_h can readily be incorporated if warranted.

The stress-strain curve for the shell material is given a bilinear representation consisting of an elastic line of slope E and a strain-hardening line of slope E_h , having a point of intersection with coordinates ϵ_y and σ_y , which define the yield strain and yield stress. Because materials of interest have relatively low values of E_h , the membrane thrust is considered constant and equal to

$$S = \frac{k}{a} H \sigma_y = \frac{k}{a} H E \epsilon_y = \frac{k}{a} H E w_o / a \quad (4.64)$$

in terms of physical quantities.

According to the tangent modulus theory the moment-curvature change relationship is

$$M = E_h I \chi \quad (4.65)$$

By following the derivation of the governing equation (4.12) for the elastic phase, but using (4.65) and (4.64) instead of (4.1) and (4.8), we find the dimensionless form of the governing equation for the plastic phase to be

$$\frac{\partial^2 w}{\partial t^2} + k_1 k_2 k_3 \left(\frac{\partial^4 w}{\partial \theta^4} + \frac{\partial^2 w}{\partial \theta^2} \right) + k_2 \bar{w}_o \left(1 + \frac{\partial^2 w}{\partial \theta^2} + w \right) = \mu p \quad (4.66)$$

where $t \geq \bar{t}$, $p = Pp_o + p^r$, and $k_3 = E_h/E$; the dimensionless quantities are listed in Table 4.1. The initial conditions are

$$w(\theta, \bar{t}) = \bar{w}(\theta) \quad \text{and} \quad \frac{\partial w}{\partial t}(\theta, \bar{t}) = \bar{v}(\theta) \quad (4.67)$$

determinable from the values at the end of the elastic phase.

4.9 SYSTEM OF GOVERNING EQUATIONS OF PLASTIC PHASE

After substituting the series representations (4.25), (4.20), and (4.28) for w , p_o , and p^r in the governing equation (4.12) and equating to zero the coefficients for each $\cos n\theta$, we obtain the following system of equations:

$$\ddot{w}_o + k_2 \bar{w}_o = \mu (Pp_o - p^r_o) \quad t \geq \bar{t} \quad (4.68)$$

$$\ddot{w}_n + k_2 (n^2 - 1) (k_1 k_3 n^2 - \bar{w}_o) w_n = \mu (Pp_n^o - p_n^r) \quad t \geq \bar{t}, n \geq 1 \quad (4.69)$$

To obtain (4.68) it is again assumed that $w_o \ll 1$. Introducing in (4.68) and (4.69) the radiation pressure coefficients (4.41) and (4.43) results in

$$\ddot{w}_o + \mu \dot{w}_o - (\mu/2)w_o = \mu P p_0^o - k_2 \bar{w}_o \quad t \geq \bar{t} \quad (4.70)$$

$$(1 + \mu \gamma_n) \ddot{w}_n + \mu \beta_n \dot{w}_n + \left[k_2 (n^2 - 1) (k_1 k_3 n^2 - \bar{w}_o) + \mu \alpha_n \right] w_n = \mu P p_n^o \quad t \geq \bar{t}, n \geq 1 \quad (4.71)$$

To obtain (4.70), we neglect the last term of (4.41) (this term is retained in the summary of Appendix A). The accompanying initial conditions are

$$w_n(\bar{t}) = \bar{w}_n \quad \dot{w}_n(\bar{t}) = \bar{v}_n \quad n \geq 0 \quad (4.72)$$

given by (4.61) and (4.62) when $n = 0$ and (4.63) when $n \geq 1$.

4.10 SOLUTION OF GOVERNING EQUATIONS OF PLASTIC PHASE

The solution of (4.70) for the hoop mode with initial conditions (4.72) is

$$\begin{aligned} w_o(\tau) &= \left[\bar{v}_o + \bar{w}_o (\mu + s_1 - k_2/s_1) \right] e^{s_1 \tau / \nu} - \left[\bar{v}_o + \bar{w}_o (\mu + s_2 - k_2/s_2) \right] e^{s_2 \tau / \nu} + \frac{2k_2 \bar{w}_o}{\mu} + \frac{\mu P}{\nu} \int_0^\tau \left[e^{s_1(\tau-\eta)} \right. \\ &\quad \left. - e^{s_2(\tau-\eta)} \right] p_0^o(t + \eta) d\eta \end{aligned} \quad (4.73)$$

where $\tau = t - \bar{t}$, $s_1 = (\nu - \mu)/2$, $s_2 = -(\nu + \mu)/2$, $\nu = s_1 - s_2 = (\mu^2 + 2\mu)^{1/2}$

The first equation of the set (4.71) governing shell translation is

$$(1 + \mu\gamma_1)\ddot{w}_1 + \mu\beta_1\dot{w}_1 + \mu\alpha_1 w_1 = \mu P p_1^0 \quad (4.74)$$

and formulas (4.44) give the coefficients

$$\alpha_1 = -\frac{1}{2} \quad \beta_1 = 1 \quad \gamma_1 = 0 \quad \text{for } t \leq 2$$

and

$$\alpha_1 = 0 \quad \beta_1 = 0 \quad \gamma_1 = 1 \quad \text{for } t \geq 2$$

Hence equation (4.74) is replaced by the following two equations

$$\ddot{w}_1 + \mu\dot{w}_1 - (\mu/2)w_1 = \mu P p_1^0 \quad t \leq 2 \quad (4.75)$$

$$(1 + \mu)\ddot{w}_1 = \mu P p_1^0 \quad t \geq 2 \quad (4.76)$$

Equations (4.75) and (4.76) are the same as (4.57) and (4.58) so that the solutions (4.59) and (4.60) extend into the plastic phase. Physically, this result simply expresses that rigid-body translation is being described and consequently is independent of the elastic and plastic deformations.

Each equation of the set (4.71) has coefficients that are constant within time intervals according to (4.43) and (4.44). Thus

$$\alpha_n = -n/2, \quad \beta_n = 1, \quad \gamma_n = 0 \quad \text{for } \bar{t} \leq t \leq 2/n$$

$$\alpha_n = 0, \quad \beta_n = 0, \quad \gamma_n = 1/n \quad \text{for } t \geq \bar{t}, \quad t \geq 2/n$$

and several cases can arise.

For $\bar{t} \leq t \leq 2/n$, (4.71) becomes

$$\ddot{w}_n + \mu \dot{w}_n + \left[k_2(n^2 - 1)(k_1 k_3 - \bar{w}_o) - \mu n/2 \right] w_n = \mu P p_n^o \quad n \geq 2 \quad (4.77)$$

which, for initial conditions (4.72), has the solution

$$w_n(\tau) = \left[\frac{\bar{v}}{v} + \frac{\bar{w}}{v}(s_1 + \mu) \right] e^{s_1 \tau/v} - \left[\frac{\bar{v}}{v} + \frac{\bar{w}}{v}(s_2 + \mu) \right] e^{s_2 \tau/v} + \frac{\mu P}{v} \int_0^{\tau} \left[e^{s_1(\tau-\eta)} - e^{s_2(\tau-\eta)} \right] p_n^o(\bar{t} + \eta) d\eta \quad (4.78)$$

where $\tau = t - \bar{t}$, $s_1 = (\mu - v)/2$, $s_2 = -(\mu + v)/2$, $v = s_1 - s_2 = \sqrt{\mu^2 + 4\{\mu n/2 + k_2(n^2 - 1)\bar{w}_o - k_1 k_2 k_3 n^2 (n^2 - 1)\}}$.

For $t \geq \bar{t}$ and $t \geq 2/n$, (4.71) becomes

$$(1 + \mu/n) \ddot{w}_n + k_2(n^2 - 1)(k_1 k_3 n^2 - \bar{w}_o) w_n = \mu P p_n^o \quad n \geq 2 \quad (4.79)$$

which, for initial conditions (4.72), has the solution (4.78) with

$$s_1 = -s_2 = [k_2(n^2 - 1)(\bar{w}_o - k_1 k_3 n^2)/(1 + \mu/n)]^{1/2}, \quad v = s_1 - s_2. \quad \text{If}$$

$\bar{t} < 2/n$ the initial conditions of (4.79) are w_n and \dot{w}_n at $t = 2/n$ obtainable from (4.78) with $\tau = (2/n) - \bar{t}$.

4.11 FINAL DEFORMATION

The final deformation is taken as the shape when the value of the hoop mode deflection determined by (4.73) reaches a maximum, that is, when $\dot{w}_o(t_f) = 0$. The mode amplitudes w_n are then determined from (4.78), and the modes are superposed to produce the final shape.

Table 4.1
DIMENSIONLESS QUANTITIES

Dimensionless Ratio *	Symbol
w/a	w
w_o/a	w_o
ct/a	t
$p/\rho c^2 = p/K$	p
$(k_i/k_a)/(H^2/12a^2)$	k_1
c_s^2/c^2	k_2
E_h/E	k_3

* Notation: w Inward radial displacement (Figure 4.1)

w_o Average inward radial displacement

a Average shell radius (Figure 4.2)

$$a = a_i + z_o \quad (\text{Figure 4.2a})$$

$$a = a_o - z_o \quad (\text{Figure 4.2b})$$

$$z_o = k_z H/2; k_z = (\zeta^2 + \lambda - 1)/\zeta(\zeta + \lambda - 1),$$

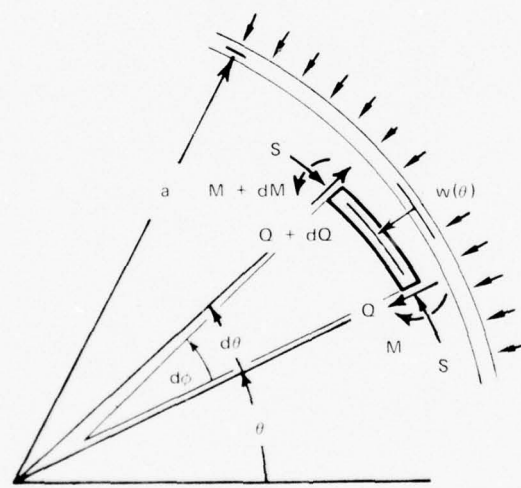
$$\zeta = H/h, \lambda = L/l$$

H Overall shell thickness (Figure 4.2)

h Plating thickness (Figure 4.2)

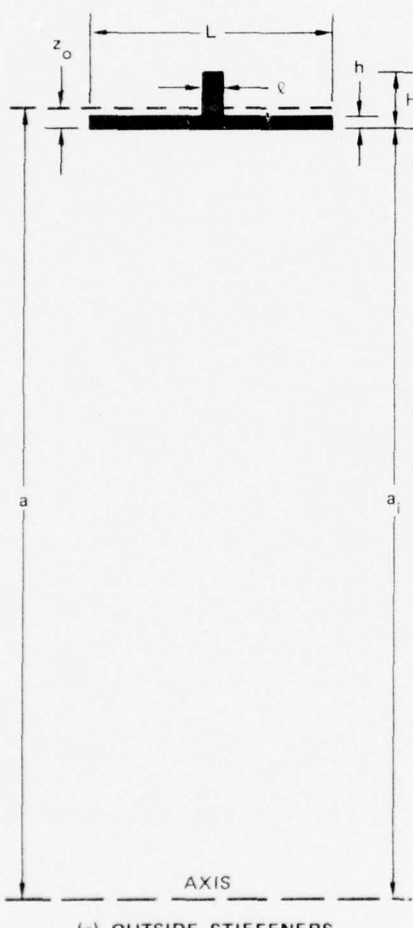
Table 4.1 (concluded)

L	Stiffener spacing (Figure 4.2)
λ	Stiffener thickness (Figure 4.2)
t	Time
ρ	Fluid density
ρ_s	Shell material density
$c = (k/\rho)^{1/2}$	Fluid sound speed
$c_s = (E/\rho_s)^{1/2}$	Shell sound speed
K	Fluid bulk modulus
E	Shell modulus of elasticity
E_h	Shell hardening modulus
p	Fluid pressure on shell
k_i	$[\lambda(\zeta^4 + \lambda - 1) - (\lambda - 1)(\zeta - 1)^4]/\lambda\zeta^3(\zeta + \lambda - 1)$
k_a	$(\zeta + \lambda - 1)/\lambda\zeta$



GA-3570-3E

FIGURE 4.1 NOTATION FOR ELEMENT OF SHELL IN MOTION



(a) OUTSIDE STIFFENERS



(b) INSIDE STIFFENERS

MA-310582-10

FIGURE 4.2 CONFIGURATIONS FOR RING-STIFFENED CYLINDRICAL SHELLS

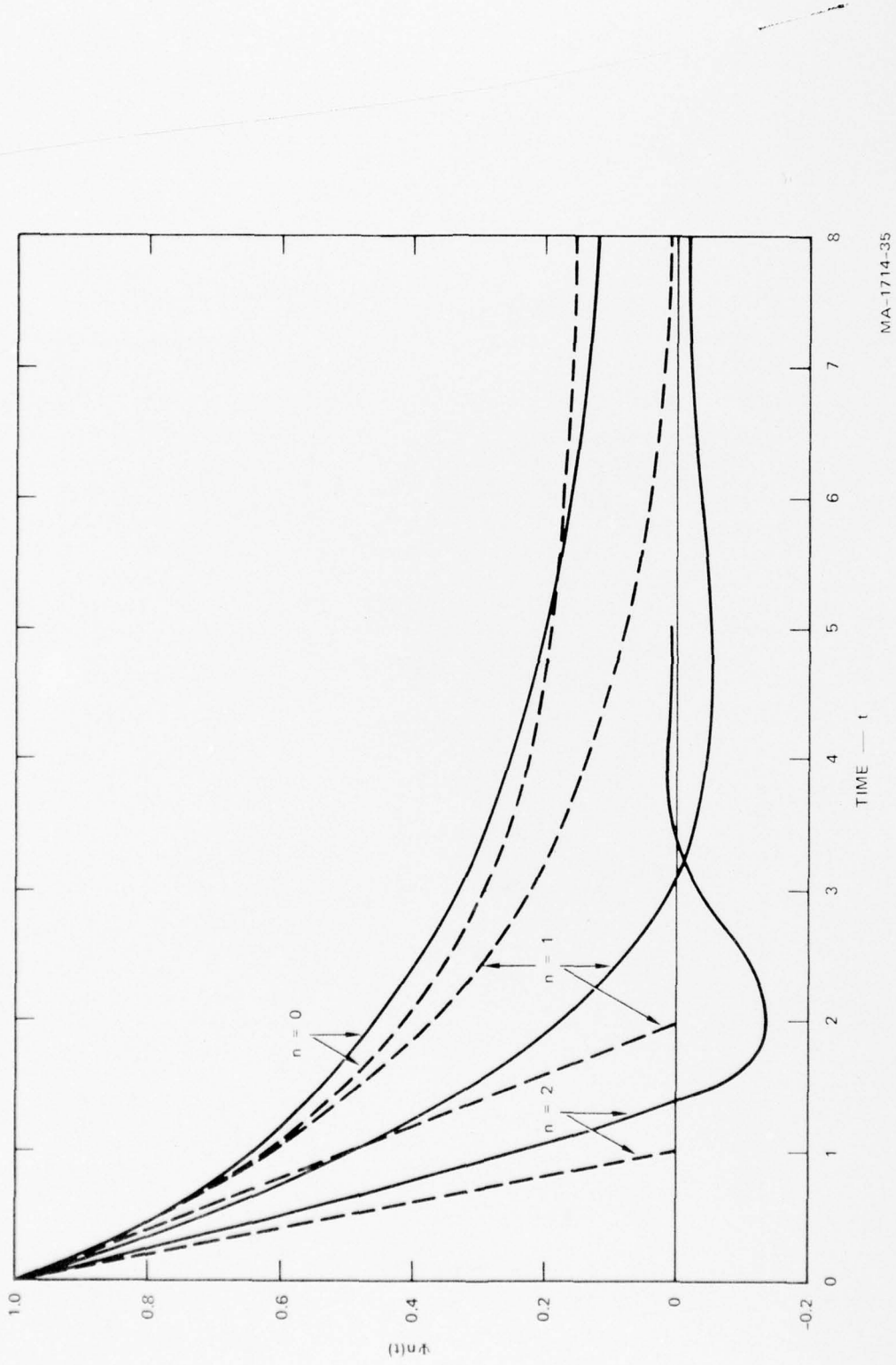
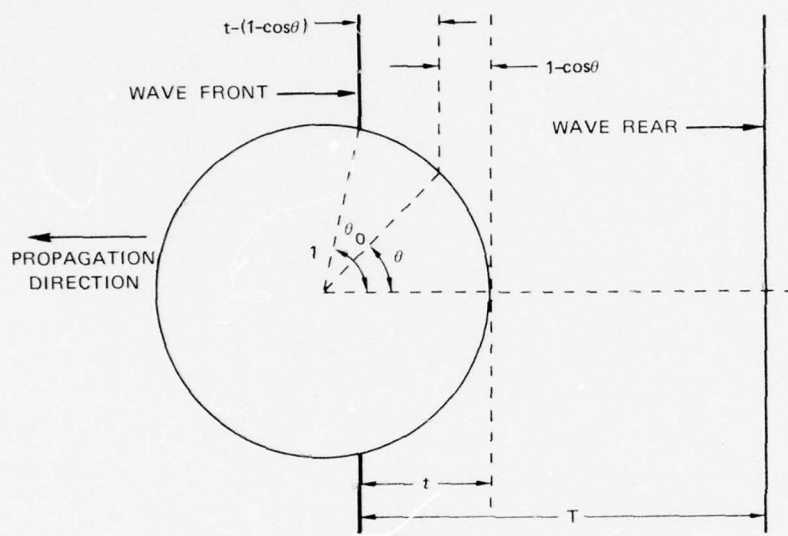
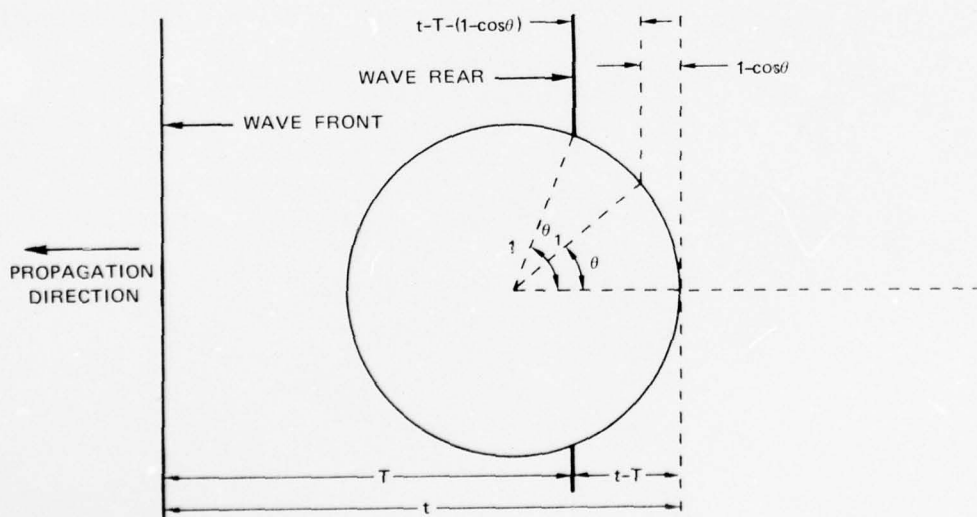


FIGURE 4.3 COMPARISON OF APPROXIMATE AND EXACT UNIT RESISTANCE FUNCTIONS

MA-1714-35



(a) LOADING



(b) UNLOADING

MA-310582-11

FIGURE 4.4 RECTANGULAR PULSE PASSING CYLINDRICAL SHELL

5. THEORETICAL RESULTS

5.1 NUMERICAL DATA

An externally stiffened model cylindrical shell (Figure 4.2a) has been chosen to illustrate the results predicted by the theory described in Section 4. The data for this numerical example are listed in Table 5.1.

The model was chosen to furnish realistic values of the required input constants k_1 , k_2 , k_3 , μ , and \bar{w}_0 . In this example the value of E_h was chosen as an average value for steels over plastic strains up to about five times the yield strain; it was found that final deformations were insensitive to E_h for k_3 in the range $0.02 < k_3 < 0.1$. With geometric scaling and the same material, the values of these constants do not change, so the results are applicable to a full-scale stiffened shell. Similarly, the values of P and T are realistic and independent of scale.

5.2 NUMERICAL RESULTS

A solution was obtained in accordance with the treatment outlined in Appendix B. Various illustrative portions of the solution are shown in Figures 5.1 through 5.19. For this example it was found that 10 modes provided an adequate description of the shell response because higher modes are not amplified during the motion (trigonometric oscillation instead of hyperbolic growth). The results are discussed in terms of dimensionless quantities.

Figures 5.1 to 5.6 show the growth of the displacement and velocity amplitudes for modes $n = 0$ to $n = 5$. Figure 5.1 shows the behavior of

the hoop mode. The associated numerical results show that plastic flow occurs at $t = \bar{t} = 1.15$ with $w_0 = \dot{w}_0 = 0.002$ and that the hoop motion ceases at $t_f = 4.13$ (incident pulse duration is $T = 3$), at which time $w_0 = 0.0087$. The maximum hoop strain is about $4.2 \epsilon_y$. The plot for the velocity shows an initial rapid increase followed by a gradual decrease until plastic flow occurs, whereupon the velocity increases until pressure unloading commences at $T = 3$.

Figure 5.2 shows the behavior of the translation mode. The maximum displacement as a rigid body is $w_1 = 0.018$, which is 1.8 percent of the radius or 1.6 wall thicknesses. The translational velocity overshoots the incident pulse particle velocity of 0.005 to reach $\dot{w}_1 = 0.0066$ at $t = 1.45$ and gradually tends to the incident wave particle velocity until pressure unloading occurs at $T = 3$. Some reverse translational velocity is predicted after $t = 36$. Computations carried out for longer times in this mode show that the shell comes to rest. Also, computations carried out for larger times with no unloading show that the shell translational velocity eventually assumes the incident * step wave particle velocity.

Figure 5.3 shows the deformation amplitude in the second mode, which is the ovaling or $\cos 2\theta$ Fourier component. The maximum displacement of $w_2 = 0.0044$ occurs at time $t = 2.55$ and is about one-half of the maximum hoop mode displacement of 0.0087.

*The behavior of the translational motion depends on the unit resistance function $\psi_1(t)$ chosen to approximate the exact function. In this example $\psi_1(t) = e^{-t/2}$ was used to provide a final shell translational velocity equal to the step incident wave particle velocity. If the two straight line approximation (4.39) is used, the final shell translational velocity is about twice the particle velocity. The mathematically correct velocity probably lies closer to the latter value. This investigation was not pursued because translational behavior has no influence over the final deformation.

Figures 5.4, 5.5, and 5.6 show the third, fourth, and fifth mode displacement amplitudes with maxima at the shell unloading time of $t_f = 4.13$ determined by the hoop mode. These maxima are 0.0025, 0.0021, and 0.0015, respectively. Corresponding figures for modes 6 through 10 are not included here, but they show continued trends of diminishing maximum amplitudes and they all occur at or near t_f .

Figure 5.7 is a plot of the maximum displacement amplitudes of modes 0 to 10 at times \bar{t} , T , and t_f . The plot allows a comparison of modal amplitude increase. For modes above about $n = 7$ the growth is negligible; in fact, these amplitudes are predicted by the theory to be oscillatory. From the distribution of Figure 5.7 it is seen that the deforming shape of the shell cross section contains mostly the Fourier components $n = 0$ and $n = 2-6$ ($n = 1$ is rigid body translation).

Figure 5.8 shows Cartesian plots of the deformed shape of the shell at times \bar{t} , T , and t_f . In this example, the shape at \bar{t} (when plastic flow starts in the hoop mode) is generally amplified during plastic buckling. However, realistic examples exist where the plastic buckling has substantial higher modes, especially for lower values of the strain-hardening modulus (e.g., $k_3 < 0.02$).
3

Figure 5.9 shows a polar plot of the final deformed shape. The maximum radially inward displacement occurs at $\theta = \pm 40^\circ$ and at the back at $\theta = 180^\circ$ (see also Figure 5.8); the displacement magnitude at $\theta = \pm 40^\circ$ is 0.0144, which is 1.66 times the hoop mode deflection $w_0(t_f)$. This collapse shape has been observed in scale model tests carried out at SRI (see Figure 3.11 for a qualitative comparison).

Figure 5.10 shows the outer fiber strain around the shell at times \bar{t} , T , and t_f . At time t_f the neutral axis hoop strain is -0.0087, and the departures from this value are ± 0.0033 . Although an analysis to examine the extent of strain-rate reversal, if any, has not yet been included in the theoretical treatment, the strain curves imply that

reversal was absent in this example (curves do not cross each other).

The lower the hardening modulus value E_h , the greater the possibility of strain-rate reversal.

Figures 5.11 through 5.14 show modes $n = 0$ to 3 for the diffraction pressure $P_p^0 - p_n^r$. Figure 5.11 shows the pressures associated with the hoop motion. The diffraction pressure monotonically tends to the free-field pressure of $P = 0.005$ until pressure unloading occurs at $T = 3$. The radiation pressure, plotted as a pressure relief caused by the shell motion, is seen by comparison with Figure 5.1 to depend primarily on the shell velocity during the initial elastic phase of deformation. During the plastic phase, the pressure relief increases in a manner similar to the shell velocity but at a slower rate because of the compensating effect of the convergent fluid afterflow. During the elastic phase, the total pressure rises to a plateau of 0.003, which is maintained until incident pressure unloading at $T = 3$. After time $T = 3$, the total pressure regains a comparable value because of the fluid afterflow and inertia.

Figure 5.12 shows the pressures associated with the rigid-body translation of the shell. The main feature is the relatively small total pressure brought about by the pressure relief caused by the shell motion.

Figures 5.13 and 5.14 show the pressures associated with shell deformation in the second and third modes. As in the case of the translational first mode, the pressure relief is considerable. Pressure magnitudes generally decrease and oscillation frequencies increase as the mode number increases. The modal amplitude velocities \dot{w}_n correspond primarily to the diffraction pressures in the elastic phase.

Figure 5.15 shows the diffraction pressure at the front ($\theta = 0$), top and bottom ($\theta = \pi/2$), and rear ($\theta = \pi$) of a rigid, fixed cylinder subjected to the incident rectangular pulse of pressure $P = 0.005$ and

duration $T = 3$, as described by the harmonics $n = 0$ to 10 . On arrival of the wave at the front of the cylinder, the incident pressure doubles in amplitude to 0.01 , which is in accordance with acoustic reflection from a rigid plane wall. Thereafter, the pressure decays to the incident pressure because of diffraction around the cylindrical surface. At the top and bottom of the cylinder the pressure history is not substantially different from the incident wave history. At the rear of the cylinder the pressure rises gradually to the incident pressure. Unloading demands the sustaining of a negative pressure in the fluid, which physically means cavitation with zero pressure. In actual underwater explosions, this effect would be reduced because the pulse cutoff would not be instantaneous.

Figure 5.16 shows the total pressure at the front, top and bottom, and rear of a cylindrical shell. At the front the pressure rises to a value of 0.009 ($P = 0.005$) but is rapidly relieved by the shell wall motion; the pressure at $\theta = 0$ drops to a value less than 0.001 . After the minimum pressure is reached, the pressures at $\theta = 0$, $\pm \pi/2$, and π rise smoothly together to a plateau of about 0.003 . A short duration of negative pressure is predicted immediately following unloading; this condition is not so severe as that shown in Figure 5.15 for the rigid, fixed cylinder. It is probable that a realistic pulse cutoff will remove this unrealistic feature.

A striking qualitative comparison with experiment is afforded by Figures A-3 and 3.12. Theory and experiment both show a sharp rise followed by a sharp decay and gradual rise. The final decay differs because the theory is based on an idealized rectangular pulse. Aside from the final decay, the main difference in the pulses is the pressure level in the valley between the sharp decay and gradual rise. This pressure level depends on the nature of the structure, and since the structures differ, these levels should not be the same.

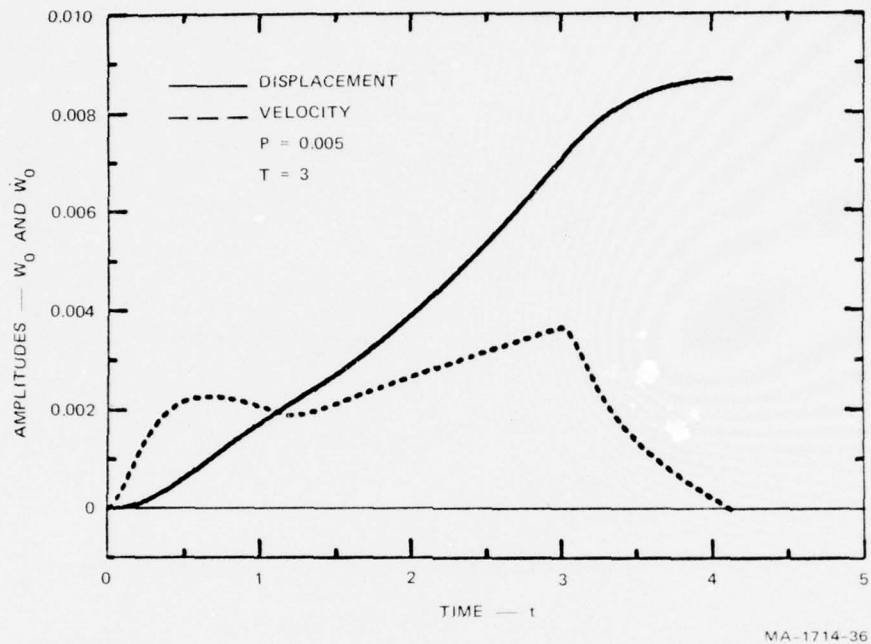
Figures 5.17 to 5.21 exhibit the history of the total pressure distribution around the cylindrical shell by means of plots at times $t = 0.5$, 1.15 , 2.0 , 3.0 , and 4.13 . A uniform pressure distribution is almost established at time $t = \bar{t} = 1.15$ (Figure 5.18) even though at this time the incident wave front has travelled only 1.15 shell radii. At the shell engulfment time $t = 2$, the pressure distribution is uniform (Figure 5.19) and remains uniform at least until the pulse duration time $t = T = 3$ (Figure 5.20). Departure from uniformity is noticeable at time $t = t_f = 4.13$ (Figure 5.21). These results are consistent with the total pressure results displayed in Figures 5.11 to 5.14, which show that the hoop mode Fourier component of pressure rapidly reaches a constant value and is much greater than the remaining components.

Table 5.1
DATA FOR STIFFENED CYLINDRICAL SHELL

Property	Symbol	Values	
Internal radius	a_i	1.44 in	3.66 cm
Wall thickness	h	0.0167 in	0.0424 cm
Stiffener depth	H	0.0985 in	0.25 cm
Stiffener width	ℓ	0.030 in	0.0762 cm
Stiffener spacing	L	0.435 in	1.105 cm
Shell density (steel)	ρ_s	7.8 g/cm^3	
Fluid density (water)	ρ	1.0 g/cm^3	
Shell elastic modulus	E	$30 \times 10^6 \text{ psi}$	206,897 MPa
Fluid bulk modulus	K	$0.33 \times 10^6 \text{ psi}$	2,276 MPa
Yield stress	σ_y	60,000 psi	
Yield strain	$\epsilon_y = \sigma_y/E$	0.002	
Shell hardening modulus	E_h	$3 \times 10^6 \text{ psi}$	20,690 MPa
Stiffener width parameter	$\lambda = L/\ell$	15.10	
Stiffener depth parameter	$\zeta = H/h$	5.90	
Area coefficient	k_a	0.2245	
Second area moment coefficient	k_i	0.1674	
Neutral axis coefficient	k_z	0.4145	
Neutral axis depth	$z_o = k_z H/2$	0.0204	
Shell radius	$a = a_i + z_o$	1.46 in	3.71 cm

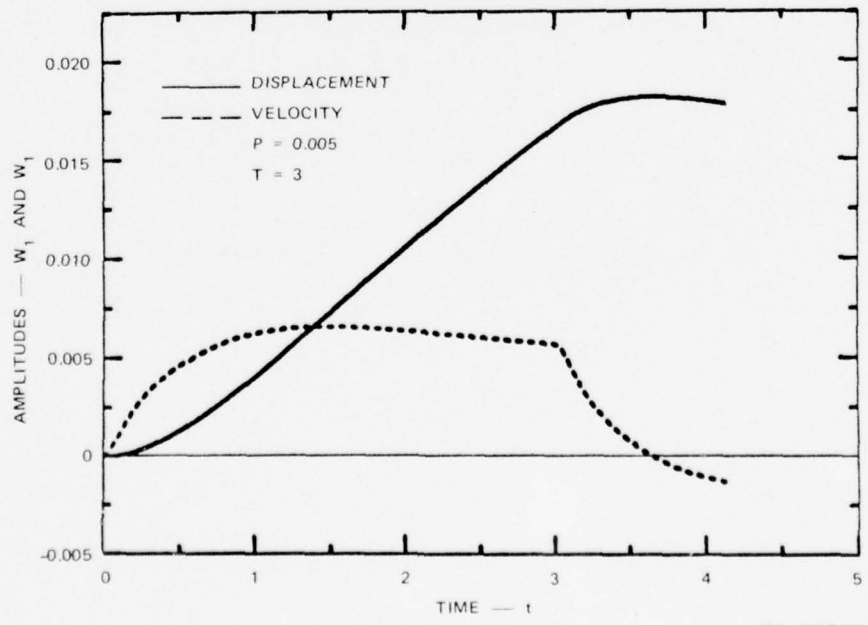
Table 5.1 (Concluded)

Property	Symbol	Values	
Fluid sound speed	$c = K/\rho$		1,509 m/sec
Shell sound speed	$c_s = E/\rho_s$		5.151 m/sec
Geometry constant	$k_1 = (k_i/k_a)(H^2/12a^2)$		
Wave speed constant	$k_2 = c_s^2/c^2$	11.655	
Plasticity constant	$k_3 = E_h/E$	0.1	
Mass constant	$\mu = \rho a/\rho_s (k_a H)$	8.465	
Maximum elastic hoop displacement	$\bar{w}_o = \epsilon_y$	0.002	
Incident pressure parameter	P	0.005	
Incident pressure	$p_i = KP$	1650 psi	11.38 MPa
Static yield pressure	$p_y = \sigma_y (k_a H)/a$	925 psi	6.38 MPa
Pulse transit time (no. of radii)	T	3	
Pulse duration	$t_d = Ta/c$	75 μ sec	



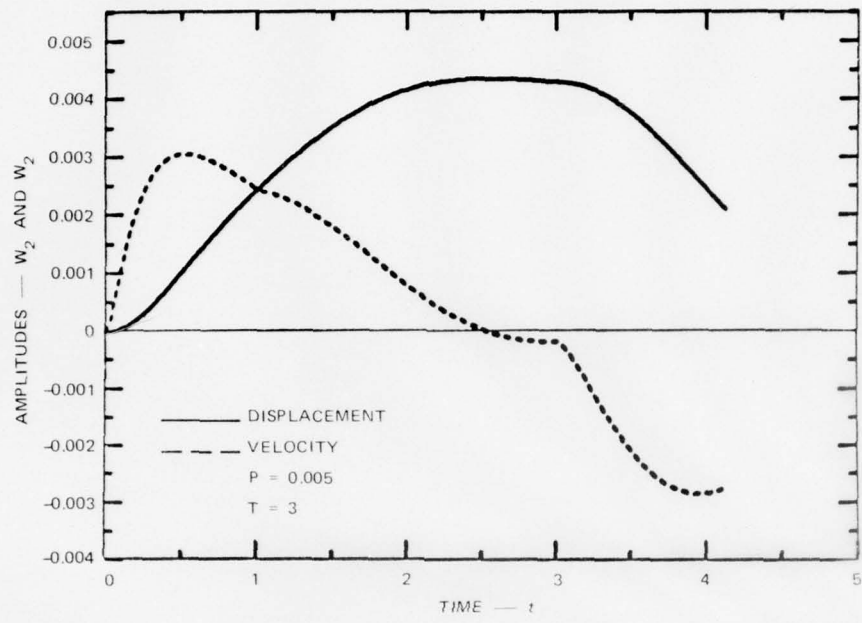
MA-1714-36

FIGURE 5.1 DISPLACEMENT AND VELOCITY AMPLITUDES FOR THE HOOP MODE ($n = 0$)



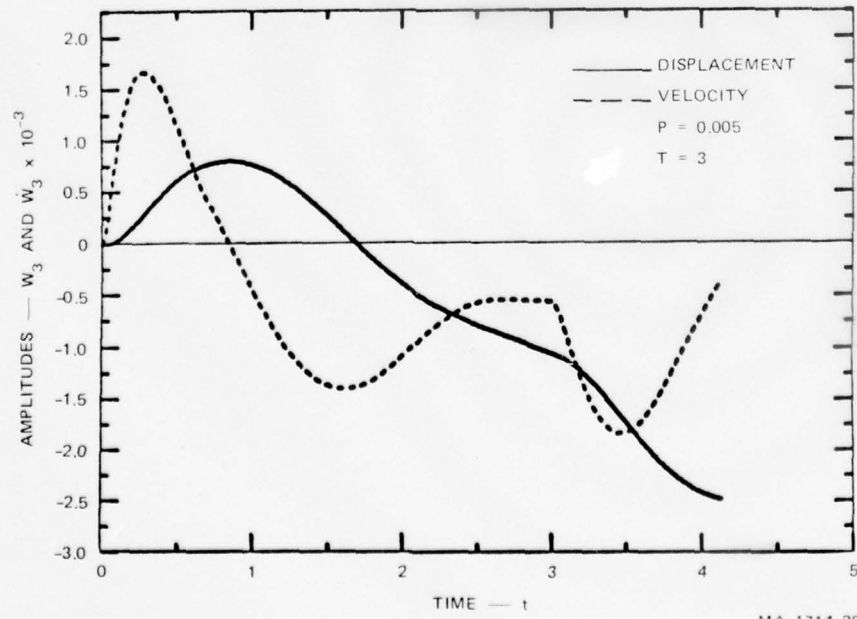
MA-1714-37

FIGURE 5.2 DISPLACEMENT AND VELOCITY AMPLITUDES FOR THE TRANSLATIONAL MODE ($n = 1$)



MA-1714-38

FIGURE 5.3 DISPLACEMENT AND VELOCITY AMPLITUDES FOR THE SECOND MODE ($n = 2$)



MA-1714-39

FIGURE 5.4 DISPLACEMENT AND VELOCITY AMPLITUDES FOR THE THIRD MODE ($n = 3$)

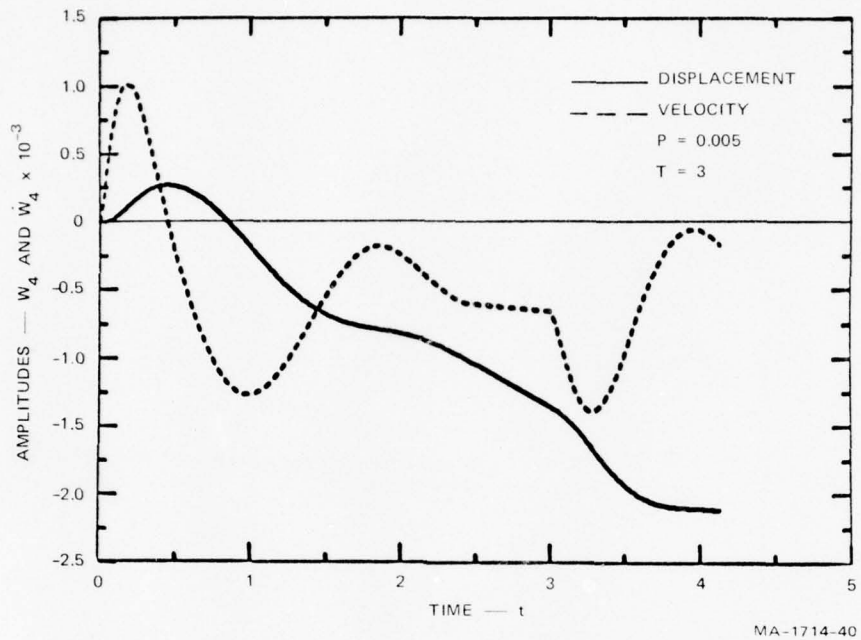


FIGURE 5.5 DISPLACEMENT AND VELOCITY AMPLITUDES FOR THE FOURTH MODE ($n = 4$)

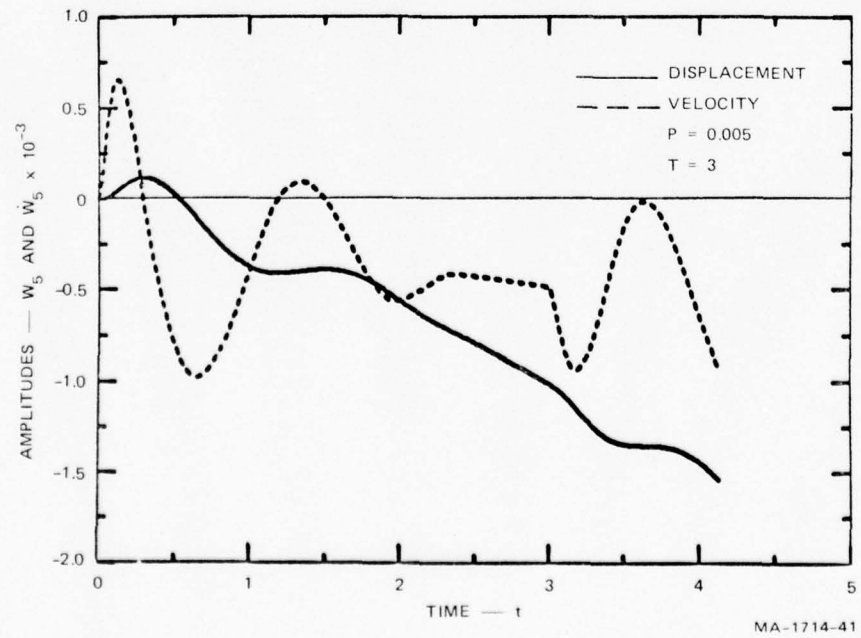


FIGURE 5.6 DISPLACEMENT AND VELOCITY AMPLITUDES FOR THE FIFTH MODE ($n = 5$)

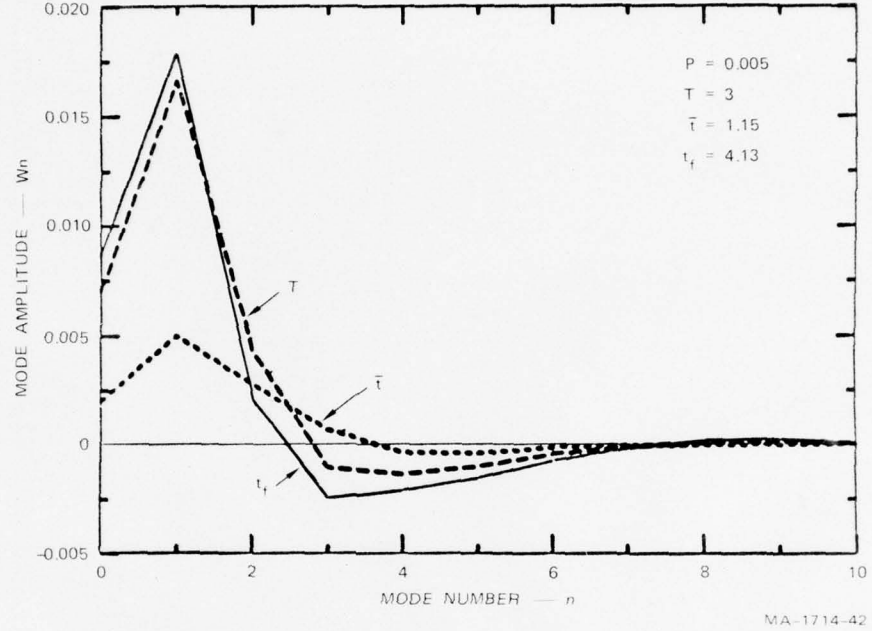


FIGURE 5.7 MODAL DISPLACEMENT AMPLITUDES AT TIMES \bar{t} , T , AND t_f

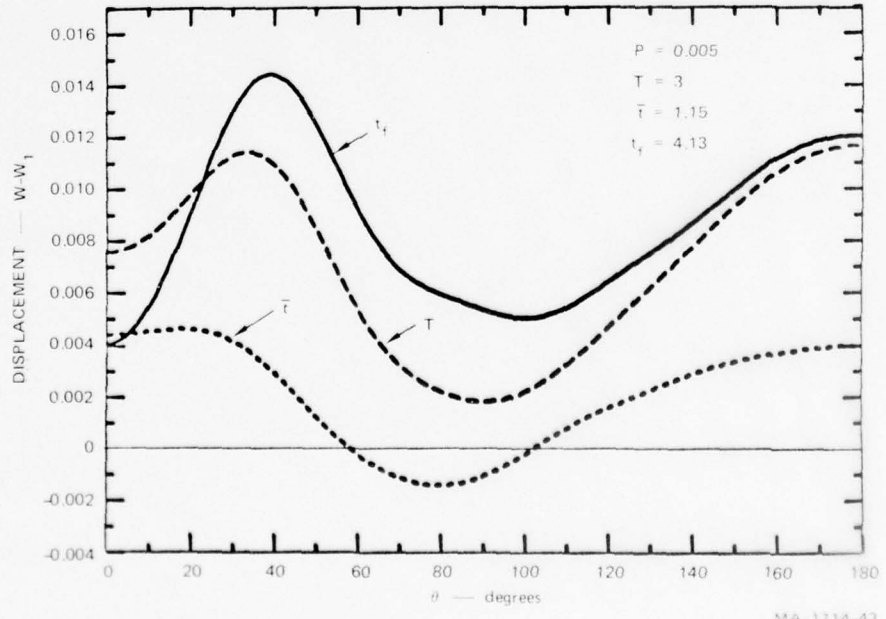


FIGURE 5.8 SHELL DISPLACEMENT AT TIMES \bar{t} , T , AND t_f (MAXIMUM $n = 10$)

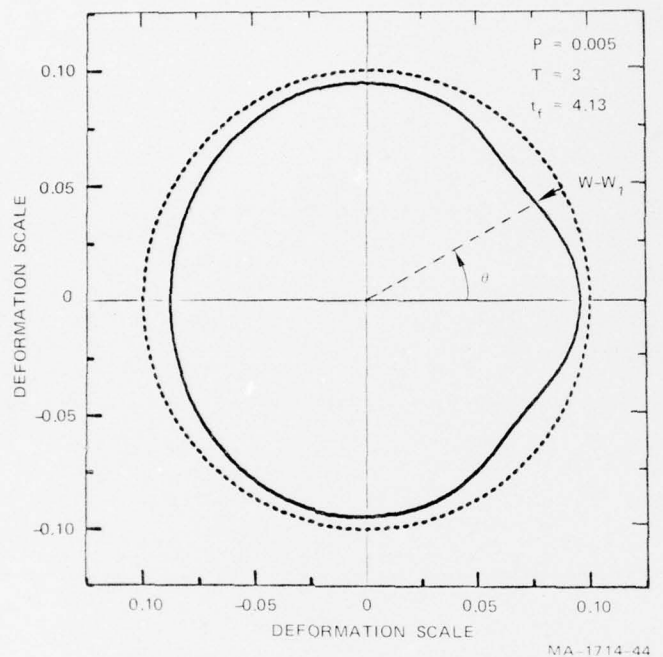


FIGURE 5.9 FINAL SHELL DEFORMATION ($t = t_f$, MAXIMUM $n = 10$)

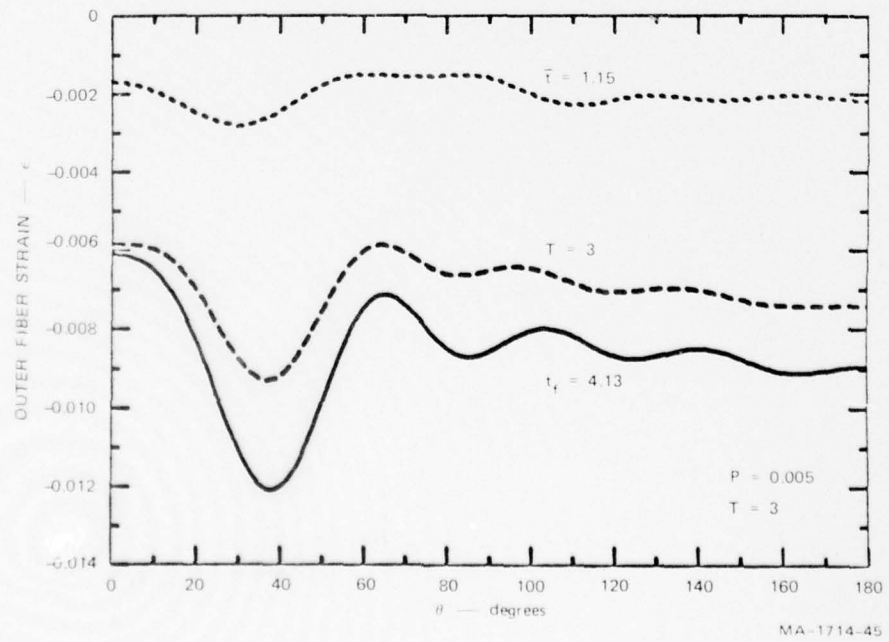


FIGURE 5.10 OUTER FIBER STRAINS AT TIMES \bar{t} , T, AND t_f
(MAXIMUM n = 10)

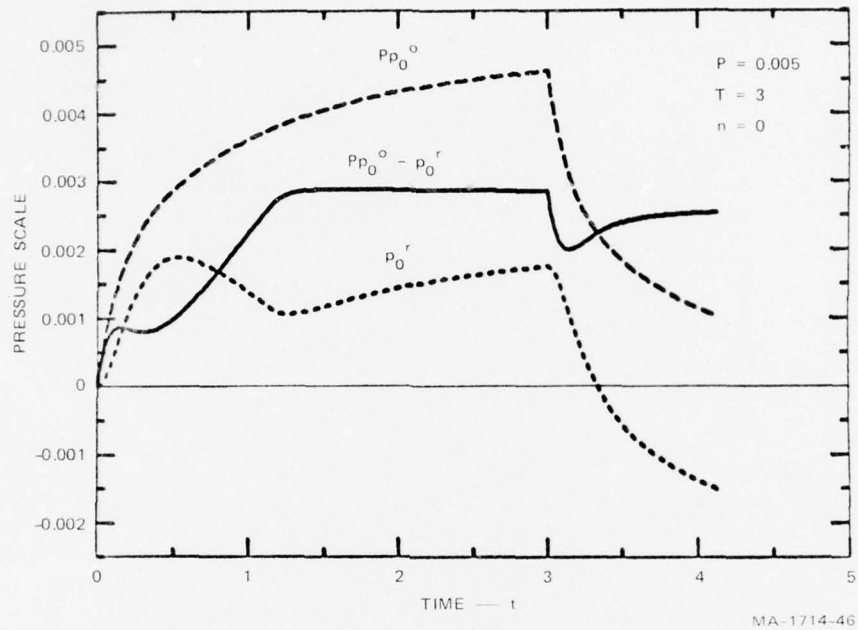


FIGURE 5.11 DIFFRACTION, RADIATION, AND TOTAL PRESSURES ASSOCIATED WITH HOOP MODE ($n = 0$)

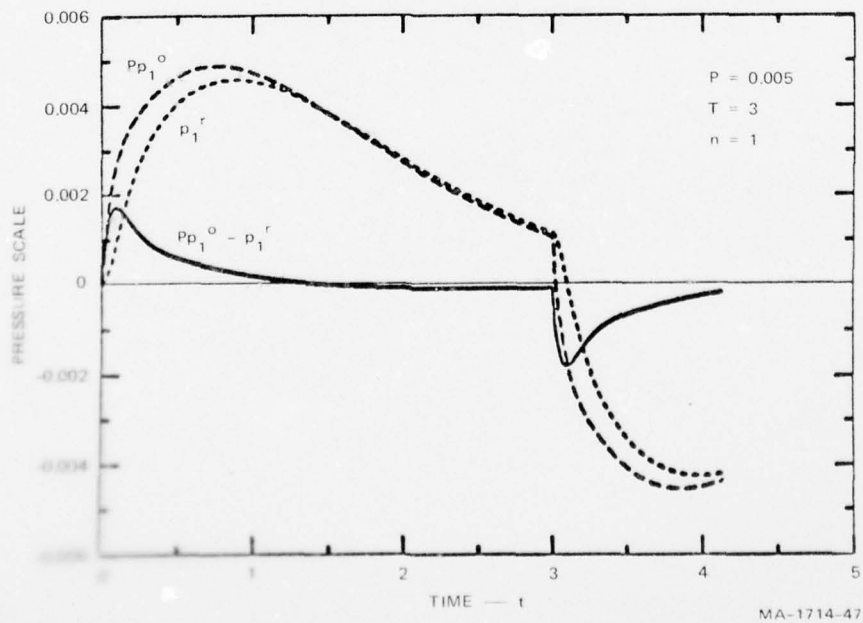


FIGURE 5.12 DIFFRACTION, RADIATION, AND TOTAL PRESSURES ASSOCIATED WITH TRANSLATIONAL MODE ($n = 1$)

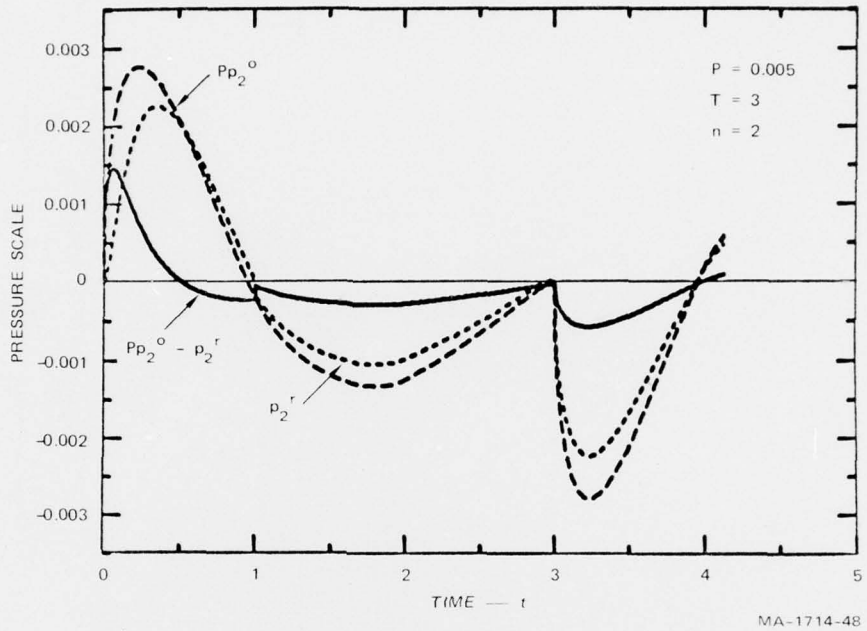


FIGURE 5.13 DIFFRACTION, RADIATION, AND TOTAL PRESSURE ASSOCIATED WITH SECOND MODE ($n = 2$)

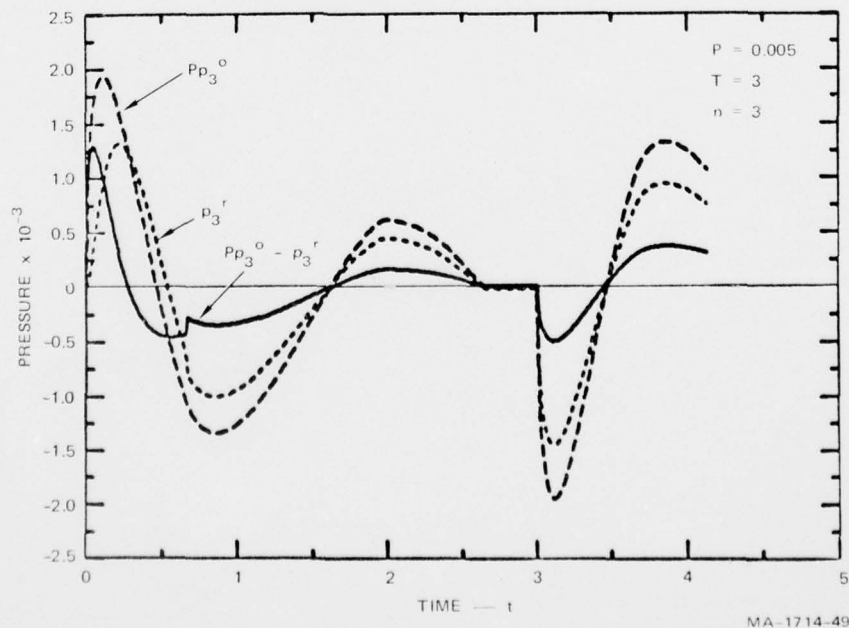


FIGURE 5.14 DIFFRACTION, RADIATION, AND TOTAL PRESSURES ASSOCIATED WITH THIRD MODE ($n = 3$)

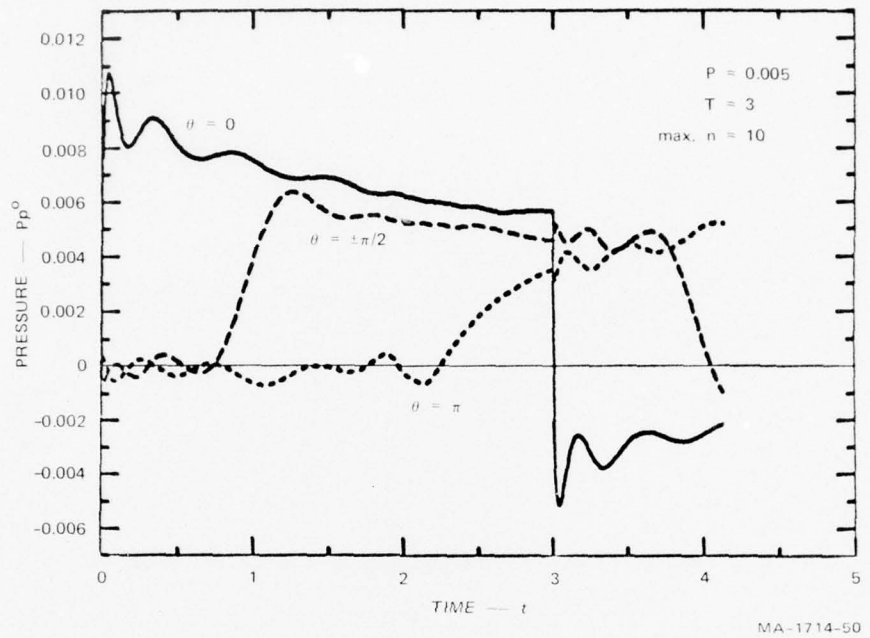


FIGURE 5.15 DIFFRACTION PRESSURE AT FRONT, TOP AND BOTTOM, AND REAR OF RIGID, FIXED CYLINDER

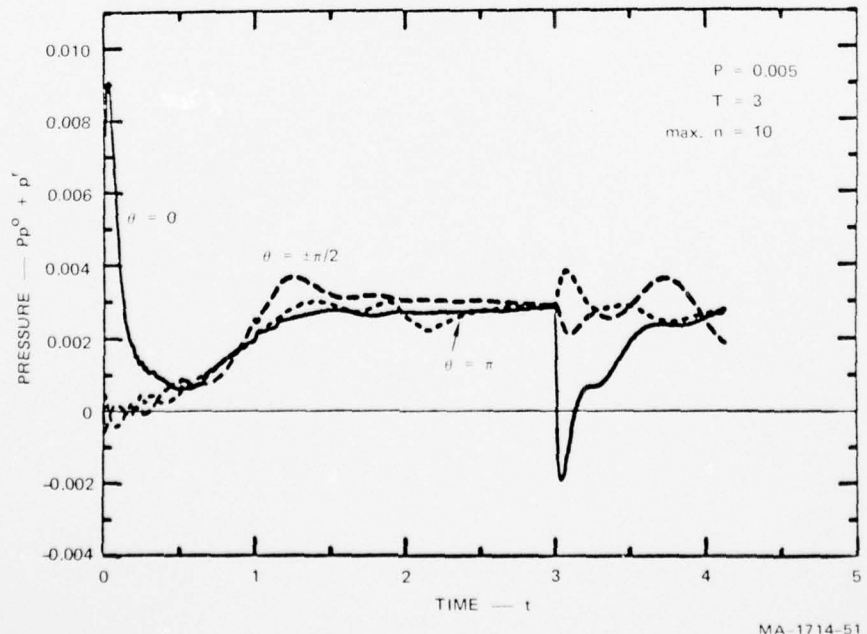


FIGURE 5.16 TOTAL PRESSURE AT FRONT, TOP AND BOTTOM, AND REAR OF CYLINDRICAL SHELL

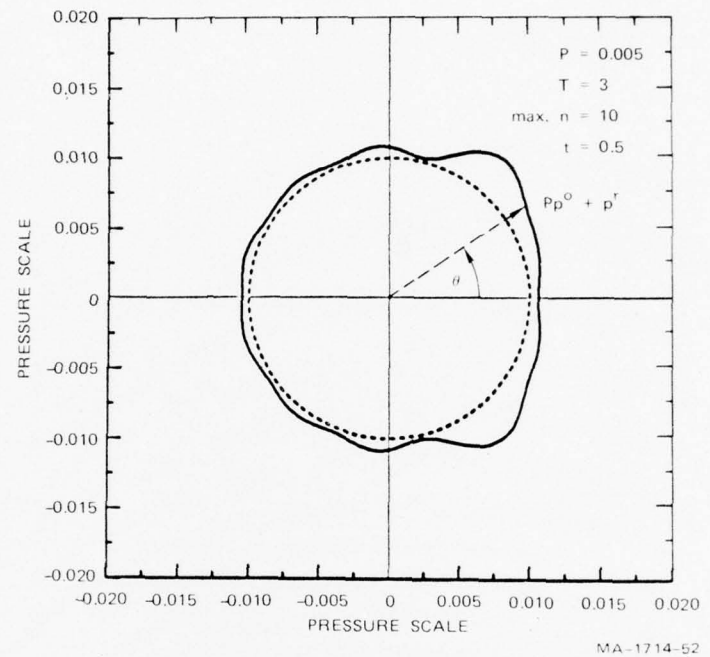


FIGURE 5.17 TOTAL PRESSURE DISTRIBUTION AT TIME $t = 0.5$

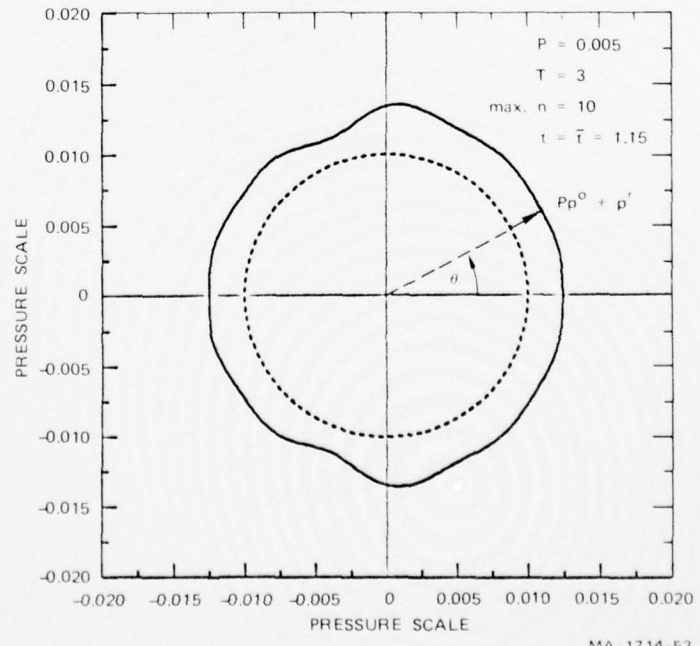


FIGURE 5.18 TOTAL PRESSURE DISTRIBUTION AT TIME $t = \bar{t} = 1.15$

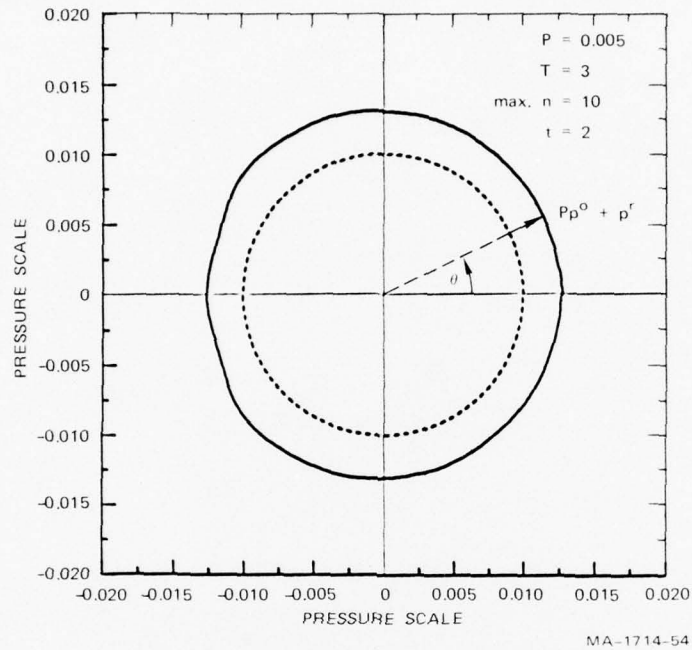


FIGURE 5.19 TOTAL PRESSURE DISTRIBUTION AT TIME
 $t = 2$

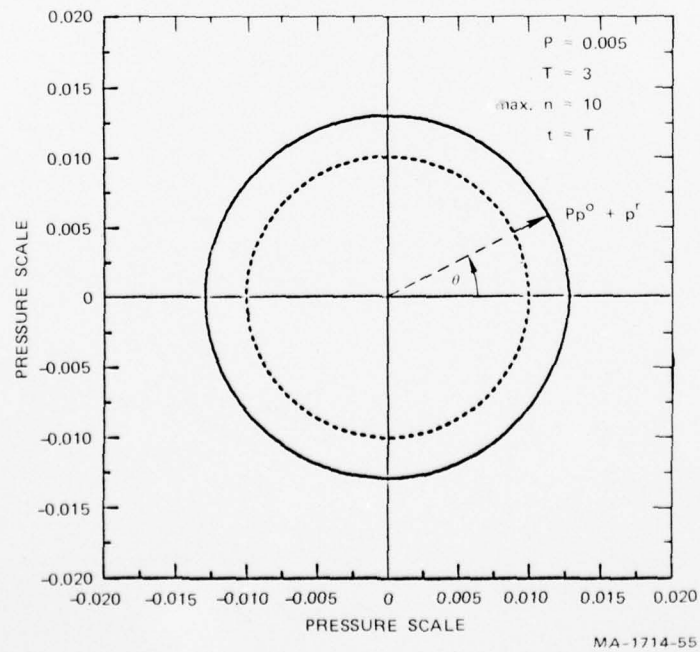
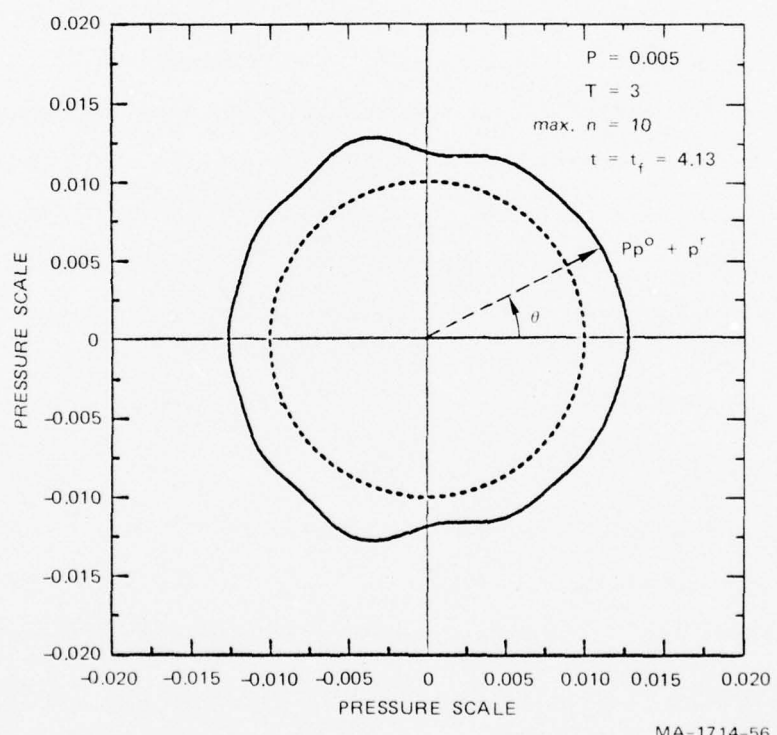


FIGURE 5.20 TOTAL PRESSURE DISTRIBUTION AT TIME
 $t = T = 3$



MA-1714-56

FIGURE 5.21 TOTAL PRESSURE DISTRIBUTION AT TIME
 $t = t_f = 4.13$

6. PRESSURE-IMPULSE ISODAMAGE REPRESENTATION AND COMPARISON WITH EXCESS IMPULSE RULE

An effective way of representing the damage to a structure by pulse loading is by an isodamage curve in the pressure-impulse plane.⁷ For an incident rectangular pulse of pressure P and duration T , the impulse is $I = PT$. Damage to a submarine shell structure may be taken as the maximum permanent radial displacement δ ; in dimensionless terms this displacement may be represented as a fraction of the shell radius or a multiple of the shell thickness. A pressure-impulse curve is therefore the curve in the P-I plane on which δ is a constant; the curve connects rectangular pulses of equal effectiveness that range from ideal impulses to step loading.

6.1 PI CURVES FOR A CYLINDRICAL SHELL

The theory described in Section 4 was used to generate P-I curves for an externally stiffened cylindrical shell having the properties listed in Table 5.1. Additional clarification of dimensional definitions may be obtained by referring to Figure 4.2(a).

The pressure and duration of the incident rectangular pulses are represented by P and T and the damage is represented nondimensionally by

$$\delta_a = \max |w(\theta, t_f) - w_1(t_f) \cos \theta| \quad (6.1)$$

that is, by the maximum inward radial displacement at the time t_f when the hoop mode inward displacement $w_0(t)$ reaches a maximum; t_f is given by $\dot{w}_0(t_f) = 0$ and the rigid body translational mode is subtracted from

the total. Dimensionally, δ_a is the maximum final inward displacement divided by the shell radius a .

Pressure-time (P-T) curves for isodamage values of δ_a equal to 0.02, 0.03, and 0.04 are shown in Figure 6.1 and the corresponding P-I curves are shown in Figure 6.2. The overall shapes of the curves resemble rectangular hyperbolas and are typical of critical load curves for many structures. The horizontal asymptote $P = 0.0025$ gives the pressure in a step incident wave that is required to just cause plastic deformation. Cross plots that show how damage gradients steepen with increasing T and P are shown in Figures 6.3 and 6.4 (compare Figures 3.13 and 6.4).

6.2 PHYSICAL QUANTITIES

The δ_a values of the isodamage curves of Figures 6.1 and 6.2 are the ratios of maximum permanent inward displacement to the original radius; that is, the damage displacement curves represent 2, 3, and 4 percent of the original radius. Because the ratio of radius to wall thickness is $a/h = 88$, the isodamage curves, as multiples of wall thickness, are $\delta_h = 1.8, 2.6$, and 3.5 . Unit values of $P = 0.001$, $T = 1$, and $I = 0.01$ correspond to an incident pressure of $p_i = KP = 330$ psi, a radius transit time of $t_d = aT/c = 25 \mu\text{sec}$, and an impulse of 82.5 psi-msec. For an acoustic step wave traveling horizontally in water, the free surface cuts off the pulse experienced at a depth D at a time equal to the transit time $t_d = D/c$.

For the model cylindrical shell subjected to a rectangular incident pulse with a duration equal to a transit time of two diameters ($t_d = 100 \mu\text{sec}$, $T = 4$), a pressure of $p_i = 2046$ psi ($P = 0.0062$) will cause a permanent deformation of 3.5 wall thicknesses ($\delta_a = 0.04$); the corresponding incident impulse is 204 psi-msec ($I = 0.0248$). The static yield pressure is $p_y = \sigma_y (kH)/a = 925$ psi, giving a pressure ratio

$p_i/p_y = 2.21$; thus the excess impulse is $I_x = (p_i - p_y)t_d = 112 \text{ psi-msec}$ ($I = 0.0136$).

As another example, if the pulse has a transit time of four diameters ($t_d = 200 \mu\text{sec}$, $T = 8$), a pressure of $p_i = 1250 \text{ psi}$ ($P = 0.0083$) will also cause a permanent deformation of 3.5 wall thicknesses ($\delta_a = 0.04$); the pressure ratio is now $p_i/p_y \approx 1.35$. The incident impulse is 250 psi-msec ($I = 0.304$) and the excess impulse is $I_x = 65 \text{ psi-msec}$ ($I = 0.0079$).

6.3 COMPARISON WITH EXCESS IMPULSE RULE

An examination of the isodamage curves shows that the excess impulse depends on the P-I or P-T point selected. For example, along curve $\delta_a = 0.04$ of Figure 6.1, the dimensionless excess impulse ranges from about 0.014 to 0.008, a difference of almost a factor of two, as P-T points range from (0.007, 3.4) to (0.0038, 8.0). Hence, excess impulse is not constant for constant damage, and therefore excess impulse is not as accurate a measure of the damage potential of underwater shock waves as the P-I representation.

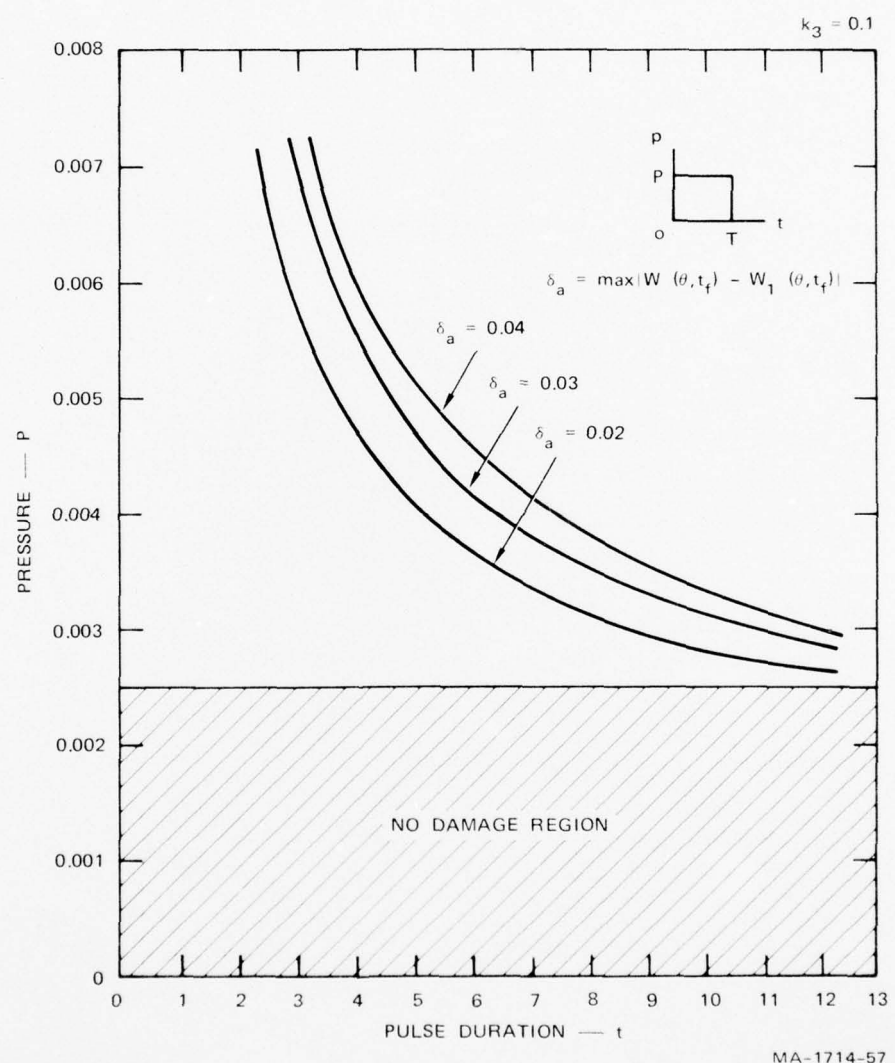


FIGURE 6.1 ISODAMAGE CURVES IN PRESSURE-DURATION PLANE

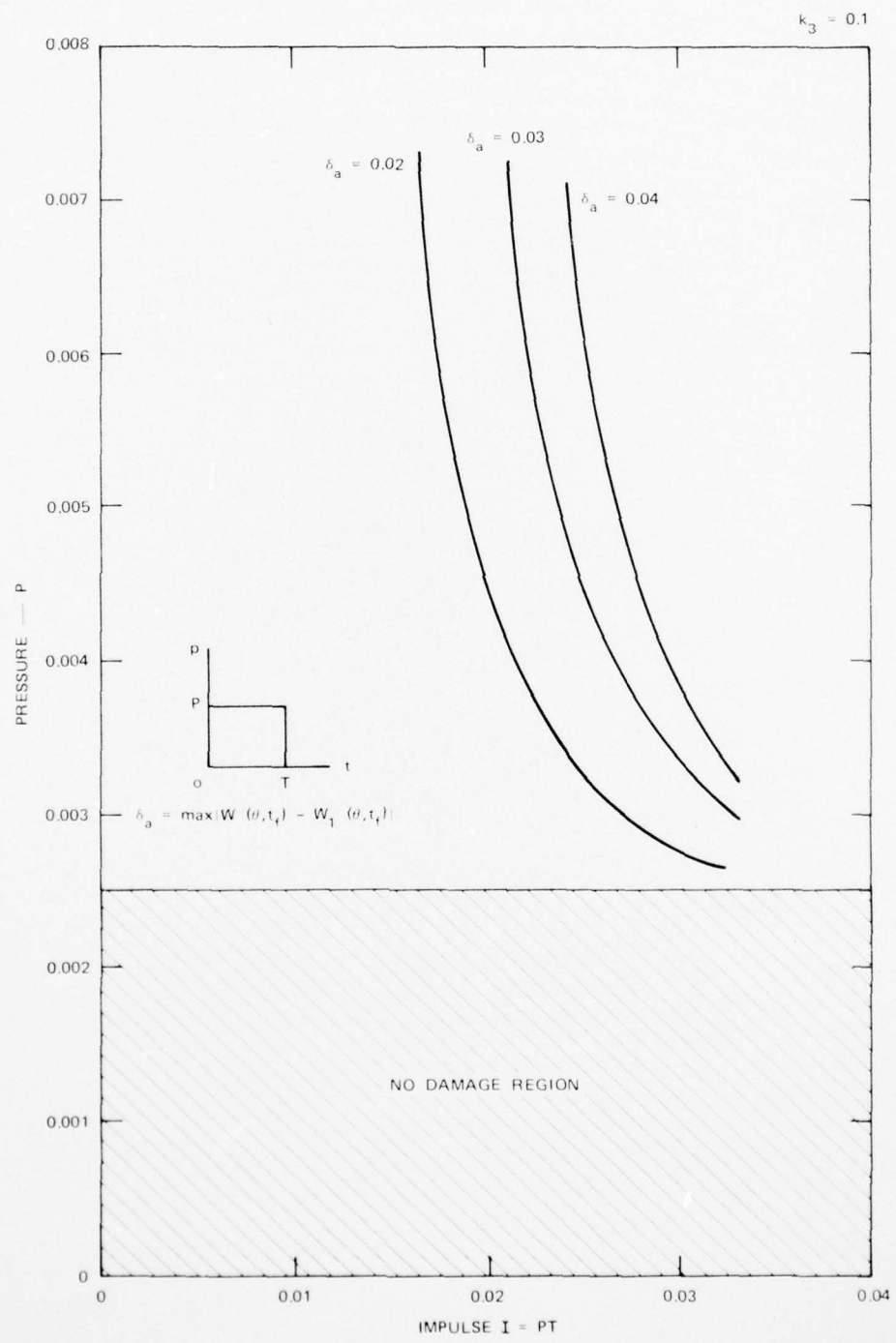
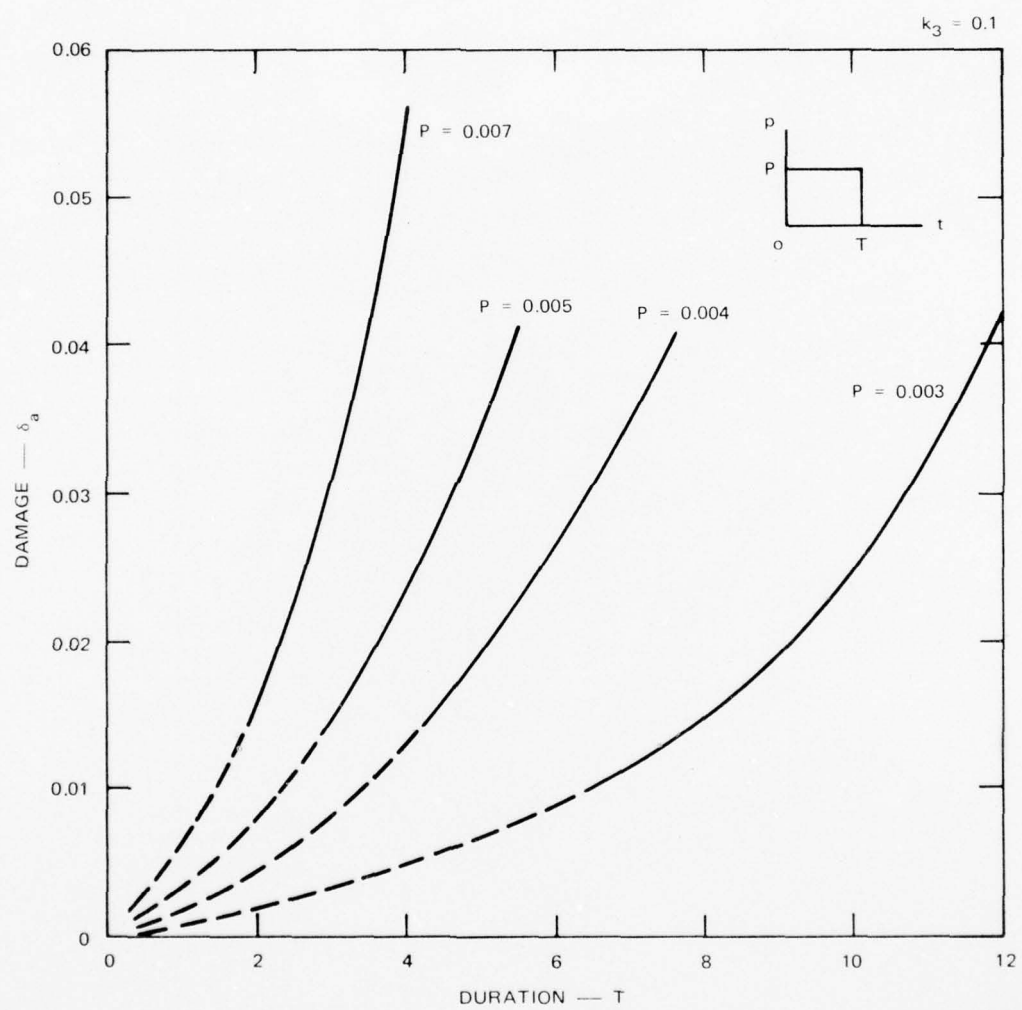


FIGURE 6.2 ISODAMAGE CURVES IN PRESSURE-IMPULSE PLANE



MA-1714-59

FIGURE 6.3 DAMAGE-DURATION GRADIENT CURVES

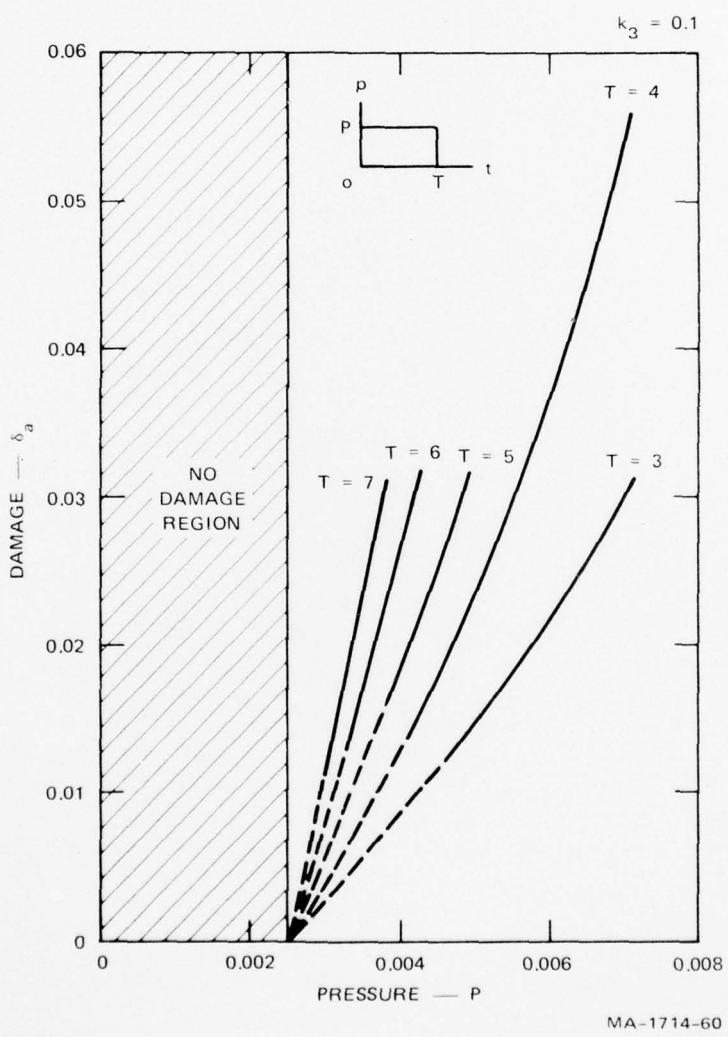


FIGURE 6.4 DAMAGE-PRESSURE GRADIENT CURVES

REFERENCES

1. G. M. Muller and G. R. Abrahamson, "A New Theory of Submarine Hull Damage from Underwater Explosions," Stanford Research Institute (Unpublished).
2. W. J. Sette and R. C. Gooding, "Damage to Stiffened Cylinders Under Scaled A-Bomb Attack in Water," Navy Department (Unpublished).
3. R. C. Gooding, G. Elmer, and W. J. Sette, "A Second Investigation on Damage to Stiffened Cylinders Under Scaled Atomic Bomb Attack," Navy Department (Unpublished).
4. J. D. Colton and J. E. Malinak, "Stress Wave Approach to the Analysis of Submarine Equipment Shock Response," to be published in Proceedings of 46th Shock and Vibration Symposium, San Diego, October 1975.
5. Ye. N. Mnev and A. K. Pertsev, "Hydroelasticity of Shells," English translation of Foreign Technology Division, Wright-Patterson Air Force Base, Ohio, Report AD-731 646 (24 August 1971).
6. F. R. Shanley, "Inelastic Column Theory," Journal of Aerospace Sciences, Vol. 14, pp. 261-268 (1947).
7. G. R. Abrahamson and H. E. Lindberg, "Peak Load-Impulse Characterization of Critical Pulse Loads in Structural Dynamics," in Dynamic Response of Structures, G. Herrmann and N. Perrone, Eds. (Pergamon Press, New York, 1972).

AD-A042 074

STANFORD RESEARCH INST MENLO PARK CALIF
A THEORY FOR CRITICAL LOADS TO DAMAGE A CYLINDRICAL SHELL BY A --ETC(U).
JUN 76 A L FLORENCE, G R ABRAHAMSON

F/G 15/6

DNA001-72-C-0087

NL

UNCLASSIFIED

DNA-4047F

2 OF 2

ADA042074



END

DATE
FILMED
8-77

Appendix A

EXCESS IMPULSE RULE

Figure A.1 shows a sketch of a simplified free-field pressure-time curve from an underwater explosion. Here p_c is the static pressure that will collapse the hull, and p_h is the local hydrostatic pressure. The excess impulse is the shaded area. The Excess Impulse Rule states that hull damage depends on the magnitude of the excess impulse.

Parnell and Schauer^{*} introduce the Excess Impulse Rule as follows. The submarine hull is regarded as a rigid-plastic system of one degree of freedom. As indicated in Figure A.2(a), the load on the hull is taken to be uniform, and the hull is assumed to deform uniformly inward. The hull material is taken to have the rigid-plastic stress-strain curve shown in Figure A.2(b). This representation of a submarine hull can be expected to be valid for distributed loads for which the deformations greatly exceed the elastic range.

The equation of motion of the model of Figure A.2 is

$$m\ddot{y} = p(t) - P_o \quad (A.1)$$

where m is the mass per unit area of the hull, \ddot{y} is the inward acceleration, $p(t)$ is the pressure acting on the hull, and P_o is the pressure

* U. C. Parnell and H. M. Schauer, "Submarine Hull Response and Damage Development," Chapter 6 in Handbook of Nuclear Explosions: Part II Effects, Report DASA-1240 II (6) and C-2188 (June 1966).

that must be exceeded to initiate deformation. Denoting, as before, the static pressure required to collapse the hull by p_c and the local hydrostatic pressure by p_h , we have

$$P_o = p_c - p_h$$

and (A.1) becomes

$$\dot{m}\ddot{y} = p(t) - (p_c - p_h) \quad (A.2)$$

To solve (A.2) in terms of the free-field pressure, we must know the relationship between the free-field pressure and $p(t)$, the load acting on the hull. For this relationship, Parnell and Schauer give, at the point of normal incidence during the engulfment phase

$$p(t) = 2 \bar{p}(t) - \rho c \dot{y} \quad (A.3)$$

where $\bar{p}(t)$ is the local free-field pressure, ρ and c are the density and sound speed of water, and \dot{y} is the inward velocity. Thus, the free-field pressure is doubled by reflection and reduced by the term $\rho c \dot{y}$ due to hull motion. The pressure calculated using this interaction law is compared with the measured free-field pressure and the measured pressure on the surface of a model for a typical example in Figure A.3. The calculated pressure history reproduces the initial spike reasonably well, but represents the remainder rather poorly.

For the postengulfment phase, Parnell and Schauer take, instead of (A.3),

$$p(t) = \bar{p}(t) - \rho c \dot{y} \quad (A.4)$$

for the interaction law. Using (A.4) in (A.2), they find as an approximate relation between the inward displacement d and the excess impulse I_x ,

$$\rho cd = I_x \quad (A.5)$$

Because of the many approximations involved in deriving (A.5), Parnell and Schauer abandon the theoretical approach at this point and adopt the functional load-deflection relation

$$d = f(I_x, H) \quad (A.6)$$

where f is a function to be determined from experimental data and H represents a combination of parameters characterizing hull design and depth of submergence.

To determine (A.6), Parnell and Schauer introduce the two parameters

$$K_s = \frac{d}{h} \left(\frac{S}{S_o} \right) \frac{1}{\left(1 - \frac{p_h}{p_c} \right)}$$

$$K_\sigma = \frac{I_x}{h} \left(\frac{\sigma_o}{\sigma_y} \right)$$

where

d = maximum stiffener deflection (inches)

h = hull plating thickness (inches)

S = stiffener factor

S_o = reference stiffener factor ($S_o = 0.013$)

σ_y = yield stress of hull material (psi)

σ_o = reference yield stress ($\sigma_o = 80,000$ psi)

and the stiffener factor is

$$S = \frac{M_s}{2 \sigma_y a h L}$$

L being the stiffener spacing, a the hull radius, and M_s the plastic limit moment of the stiffener with one frame spacing of hull plating.

Test results plotted in terms of the two parameters of (A.7) are shown in Figure A.4. From this figure, Parnell and Schauer obtain

$$K_s = 0.3 (K_\sigma)^2 \quad (A.8)$$

or

$$\frac{d}{h} = 0.3 \left(\frac{s_o}{s} \right) \left[\frac{I_x}{h} \frac{\sigma_o}{\sigma_y} \right]^2 \left(1 - \frac{p_h}{p_c} \right) \quad (A.9)$$

This is the Excess Impulse Rule. Thus, the Excess Impulse Rule is an empirical relation based on the correlation of test results indicated in Figure A.4.

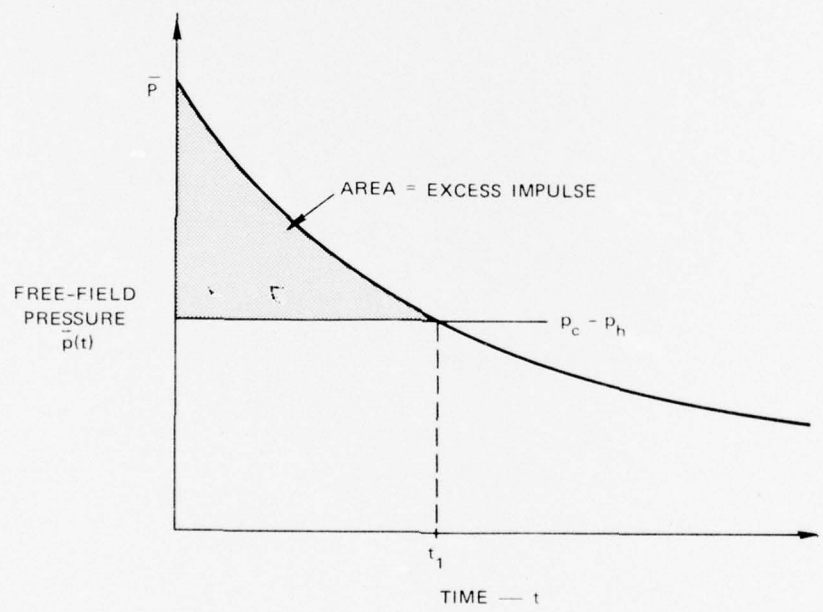
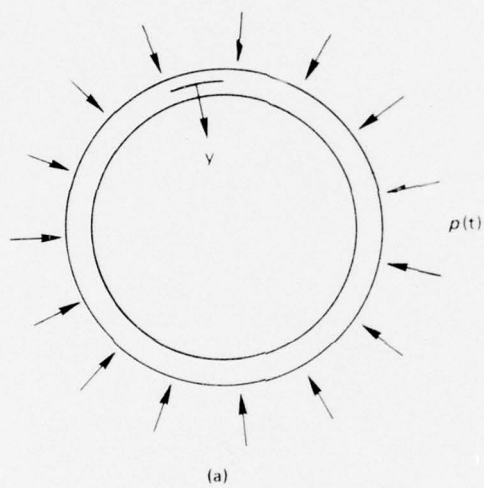
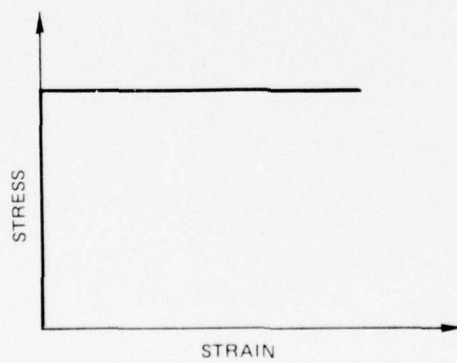


FIGURE A.1 DEFINITION OF EXCESS IMPULSE



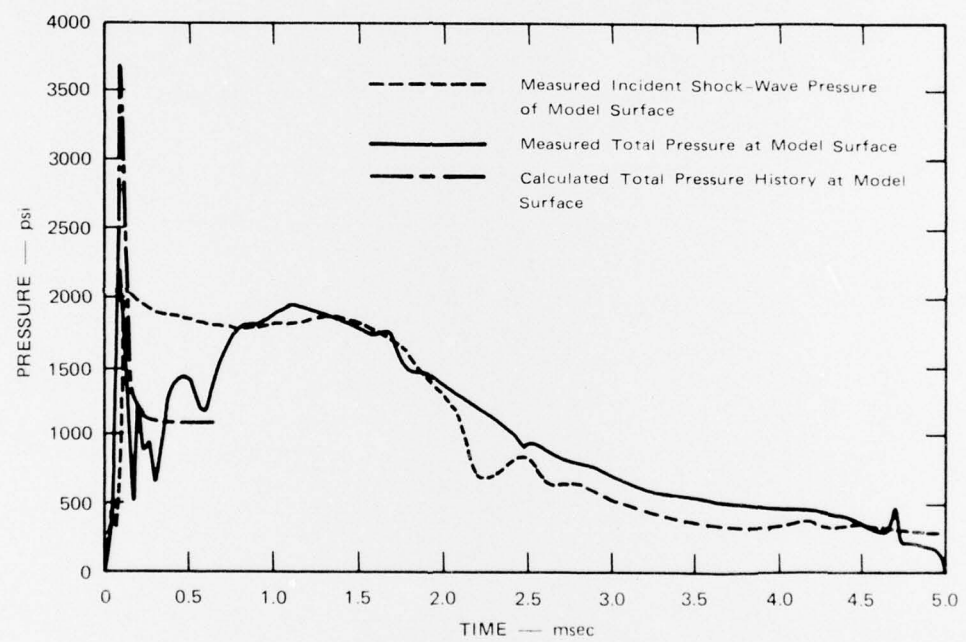
(a)



(b)

MA-1111-6

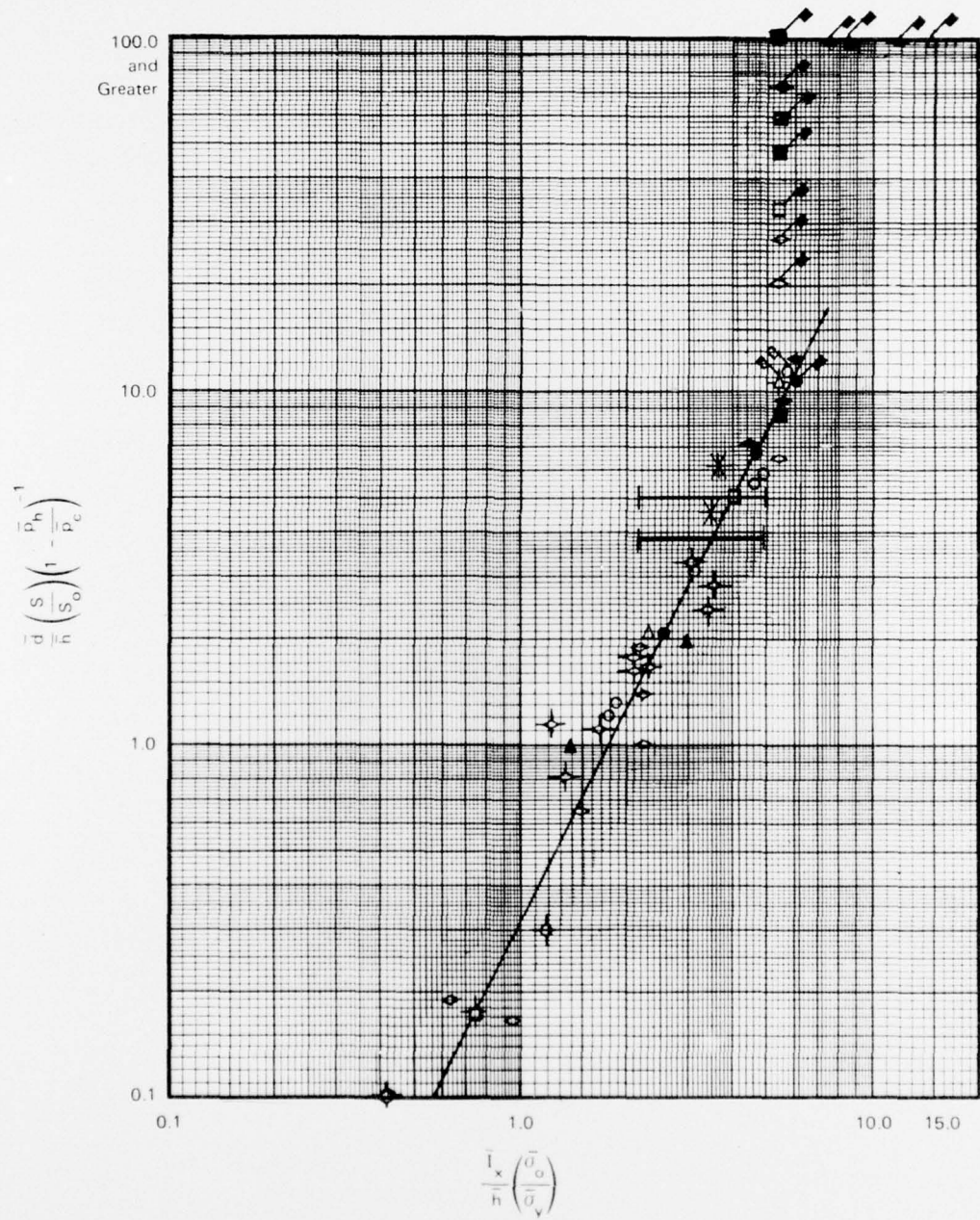
FIGURE A.2 RIGID-PLASTIC SYSTEM



(After Parnell and Schauer, Figure 6.7.3.)

MA-1111-7

FIGURE A.3 CALCULATED AND MEASURED PRESSURE HISTORIES



(After Parnell and Schauer, Figure 6.7.4.)

MA-1111-8A

FIGURE A.4 PLOT OF EXPERIMENTAL DATA SHOWING RELATIONSHIP OF K_s AND K_o

Appendix B

SUMMARY OF MATHEMATICAL TREATMENT

This appendix collects the governing equations and solutions for dynamic overall buckling by a rectangular incident pulse. Also included are some improvements to the approximate results given in Section 4 that were suggested by the study of numerical examples. The treatment given in this appendix was used to generate the numerical results of Sect. . The description is developed by modes.

Fundamental Mode ($n = 0$)

The governing equations for elastic ($0 < t < \bar{t}$), and plastic ($t > \bar{t}$) motion in the hoop mode are

$$\ddot{w}_o + k_2 \frac{w}{r} = \mu (P p_0^0 - p_0^r) \quad 0 < t < \bar{t} \quad (B.1)$$

$$\ddot{w}_o = \mu (P p_0^0 - p_0^r) - k_2 \frac{\dot{w}}{r} \quad t > \bar{t} \quad (B.2)$$

Expressions for the diffraction and radiation pressures are (4.40) and (4.41), obtained by substituting the approximate unit resistance function (4.38) in formulas (4.36) and (4.33). For step loading a better approximation to the diffraction pressure is given by Mnev and Pertsev^{*} as

$$p_0^0(t) = f_0(t) = 1 - 0.282e^{-0.464t} - 0.391e^{-1.376t} - 0.327e^{-8.0t} \quad (B.3)$$

^{*}Ye. Mnev and A. K. Pertsev, "Hydroelasticity of Shells," English translation of Foreign Technology Division, Wright-Patterson Air Force Base, Ohio, Report AD-731 646 (24 August 1971).

Thus, for a rectangular pulse of duration T ,

$$p_0^o(t) = H(t) f_0(t) - H(t - T)f(t - T) \quad (B.4)$$

Equations (B.1) and (B.2) may now be written in the form

$$\ddot{w}_o + \mu \dot{w}_o + (k_2 - \mu/2)w_o + (\mu/4a) \int_0^t w_o(\tau) e^{-(t-\tau)/2a} d\tau = \mu p_0^o(t) \quad 0 < t < \bar{t} \quad (B.5)$$

$$\ddot{w}_o + \mu \dot{w}_o - (\mu/2)w_o + (\mu/4a) \int_0^t w_o(\tau) e^{-(t-\tau)/2a} d\tau = \mu p_0^o(t) - k_2 \bar{w}_o \quad t > \bar{t} \quad (B.6)$$

with the diffraction pressure given by (B.4) and (B.3). Equations (B.5) and (B.6) are solved by numerical methods.

Translational Mode ($n = 1$)

The equation governing translational motion is

$$\ddot{w}_1 = \mu(p_1^o - p_1^r) \quad (B.7)$$

Expressions for the diffraction and radiation pressure are (4.42) and (4.43), obtained by substituting the approximate unit resistance function (4.39) in formulas (4.36) and (4.33). For step loading a better approximation to the diffraction pressure is given by Mnev and Pertsev as

$$p_1^o(t) = f_1(t) = 2.97 \left[e^{-0.646t} \cos(t/3) - e^{-1.725t} \right] \\ + 0.6 \left(e^{-4.5t} - e^{-16.0t} \right) \quad (B.8)$$

Thus, for a rectangular pulse of duration T ,

$$p_1^o(t) = H(t) f_1(t) - H(t - T) f_1(t - T) \quad (B.9)$$

Again for step loading, a better approximation to the radiation pressure p_1^r is obtained by introducing the approximate unit resistance function $\psi_1(t) = e^{-t/2}$ instead of (4.43) in formula (4.33). This function gives a final shell translational velocity equal to the step incident wave particle velocity. The resulting governing equation is

$$\ddot{w}_1 + \mu \dot{w}_1 - (\mu/2)w_1 + (\mu/4) \int_0^t w_1(\tau) e^{-(t-\tau)/2} d\tau = \mu P p_1^o(t) \quad (B.10)$$

with the diffraction pressure given by (B.8) and (B.9). Equation (B.10) is solved by numerical methods.

Buckling Modes ($n \geq 2$)

The governing equations for elastic ($0 < t < \bar{t}$) and plastic ($t > \bar{t}$) motion in the higher modes are

$$\ddot{w}_n + k_2(n^2 - 1) \left[k_1 n^2 - w_o^o(t) \right] w_n = \mu (P p_n^o - p_n^r) \quad 0 < t < \bar{t} \quad (B.11)$$

$$\ddot{w}_n + k_2(n^2 - 1) (k_1 k_3 n^2 - \bar{w}_o^o) w_n = \mu (P p_n^o - p_n^r) \quad t > \bar{t} \quad (B.12)$$

with the diffraction pressure p_n^o , obtained by substituting (4.39) in (4.36), is

$$p_n^o(t) = a_n(t) - b_n(t) + (n/2) \int_0^t b_n(\tau) d\tau - (n/2) H(t - 2/n) \int_0^{t-2/n} b_n(\tau) d\tau \quad (B.13)$$

in which, for a unit rectangular incident pulse of duration T ,

$$\begin{aligned}
 a_n(t) &= A_n(t) - A_n(t-T) \\
 b_n(t) &= B_n(t) - B_n(t-T) \\
 A_n(t) &= [H(t) - H(t-2)]f_n(t) \\
 B_n(t) &= [H(t) - H(t-2)]g_n(t) \\
 f_n(t) &= \frac{2}{\pi n} \sin n\theta_0 \\
 g_n(t) &= -\frac{1}{\pi} \left[\frac{\sin(n+1)\theta_0}{n+1} + \frac{\sin(n-1)\theta_0}{n-1} \right] \\
 \cos\theta_0 &= 1-t
 \end{aligned} \tag{B.14}$$

Explicit expressions for the diffraction pressure (B.13) are listed below.

Loading ($t < T$):

$$\begin{aligned}
 0 < t < \frac{2}{n}, \quad p_n^o &= f_n - g_n + \frac{n}{2} \int_0^t g_n(\tau) d\tau \\
 \frac{2}{n} < t < 2, \quad p_n^o &= f_n - g_n + \frac{n}{2} \int_0^t g_n(\tau) d\tau \\
 2 < t < 2 + \frac{n}{2}, \quad p_n^o &= \frac{n}{2} \int_{t-2/n}^2 g_n(\tau) d\tau \\
 2 + \frac{2}{n} < t, \quad p_n^o &= 0
 \end{aligned}$$

Unloading ($t > T$) (Cases for $T > 1$):

$$1 < t < 2 \quad p_n^o = f_n(t) - g_n(t) + \frac{n}{2} \int_{t-2/n}^t g_n(\tau) d\tau - f_n(t-T)$$

$$+ g_n(t-T) - \frac{n}{2} \int_{\max(t-2/n, T)}^t g_n(\tau-T) d\tau$$

$$2 < t < 2 + \frac{2}{n} < T + 2, \quad p_n^o = \frac{n}{2} \int_{t-2/n}^2 g_n(\tau) d\tau - f_n(t-T)$$

$$+ g_n(t-T) - \frac{n}{2} \int_{\max(t-2/n, T)}^t g_n(\tau-T) d\tau$$

$$2 + \frac{2}{n} < t < T + 2, \quad p_n^o = -f_n(t-T) + g_n(t-T)$$

$$- \frac{n}{2} \int_{\max(t-2/n, T)}^t g_n(\tau-T) d\tau$$

$$T + 2 < t < T + 2 + \frac{2}{n}, \quad p_n^o = - \frac{n}{2} \int_{t-\frac{2}{n}}^{T+2} g_n(\tau-T) d\tau$$

$$T + 2 + \frac{2}{n} < t \quad p_n^o = 0$$

The radiation pressure, given by (4.43) and (4.44), is substituted in the governing equations to produce the following two equations for elastic ($0 < t < \bar{t}$) and plastic ($t > \bar{t}$) motion:

$$(1 + \mu \gamma_n) \ddot{w}_n + \mu \beta_n \dot{w}_n + \left[k_2(n^2 - 1)(k_1 n^2 - w_o) + \mu \alpha_n \right] w_n = \mu P p_n^o \quad (B.15)$$

$$(1 + \mu \gamma_n) \ddot{w}_n + \mu \beta_n \dot{w}_n + \left[k_2(n^2 - 1)(k_1 k_3 n^2 - \bar{w}_o) + \mu \alpha_n \right] w_n = \mu P p_n^o \quad (B.16)$$

with the diffraction pressure p_n^o given by (B.13) and (B.14), and the values of the parameters α_n , β_n , γ_n given by (4.44), that is

$$\alpha_n = -n/2 \quad \beta_n = 1 \quad \gamma_n = 0 \quad \text{for} \quad t < 2/n$$

$$\alpha_n = 0 \quad \beta_n = 0 \quad \gamma_n = 1/n \quad \text{for} \quad t > 2/n$$

In general, equation (B.15) governing elastic motion is solved numerically because of the term $w_o(t)$. However, for practical values of the parameters k_1 , k_2 , k_3 , and μ , and for n sufficiently large, $w_o(t)$ may be neglected. For these cases, solutions are

$$w_n = \frac{\mu P}{\gamma_n} \int_0^t p_n^o(\tau) e^{-\mu(t-\tau)/2} \sin \gamma_n(t - \tau) d\tau \quad (B.17)$$

$$0 < t < 2/n$$

$$\text{where } \gamma_n = \left[\lambda_n^2 - (\mu/2) \right]^{1/2}, \quad \lambda_n^2 = k_1 k_2 (n^2 - 1) n^2 - \mu n/2$$

and

$$w_n = \tilde{w}_n \cos \lambda_n (t - \tilde{t}) + \frac{\tilde{v}_n}{\lambda_n} \sin \lambda_n (t - \tilde{t}) \\ + \frac{\mu P}{(1 + \mu/n) \lambda_n} \int_{\tilde{t}}^t p_n^o(\tau) \sin \lambda_n (t - \tau) d\tau \quad \frac{2}{n} < t < \tilde{t} \quad (B.18)$$

where $\tilde{t} = 2/n$, $\tilde{w}_n = w_n(\tilde{t})$, $\tilde{v}_n = \dot{w}_n(\tilde{t})$, and $\lambda_n^2 = \frac{k_1 k_2 (n^2 - 1)n^2}{1 + \mu/n}$

Equation (B.16) governing plastic motion has the solutions for $0 < \tilde{t} < t < 2/n$:

$$w_n = \left[\tilde{w}_n \cos \psi_n (t - \tilde{t}) + \frac{(\tilde{v}_n + \frac{\tilde{w}_n \mu/2}{\psi_n})}{\psi_n} \sin \psi_n (t - \tilde{t}) \right] e^{-\mu(t-\tilde{t})/2} \\ + \frac{\mu P}{\psi_n} \int_{\tilde{t}}^t p_n^o(\tau) e^{-\mu(t-\tau)/2} \sin \psi_n (t - \tau) d\tau \quad (B.19)$$

where $\psi_n^2 = [\lambda_n^2 - (\mu/2)]^{1/2}$, $\lambda_n^2 = k_2(n^2 - 1)(k_1 k_3 n^2 - \frac{w_o^2}{\psi_n^2}) - \mu n/2 > (\mu/2)^2$

and

$$w_n = \left[\tilde{w}_n \cosh \psi_n (t - \tilde{t}) + \frac{(\tilde{v}_n + \frac{\tilde{w}_n \mu/2}{\psi_n})}{\psi_n} \sinh \psi_n (t - \tilde{t}) \right] e^{-\mu(t-\tilde{t})/2} \\ + \frac{\mu P}{\psi_n} \int_{\tilde{t}}^t p_n^o(\tau) e^{-\mu(t-\tau)/2} \sinh \psi_n (t - \tau) d\tau \quad (B.20)$$

$$\text{where } \nu_n = \left[(\mu/2)^2 - \lambda_n^2 \right]^{1/2}$$

and

$$\lambda_n^2 = k_2(n^2 - 1)(k_1 k_3 n^2 - \bar{w}_o) - \mu n/2 > 0, \quad \lambda_n^2 < (\mu/2)^2$$

$$\text{or } \nu_n = \lambda_n^2 + (\mu/2)^2^{1/2}$$

and

$$\lambda_n^2 = \left[-k_2(n^2 - 1)(k_1 k_3 n^2 - \bar{w}_o) - \mu n/2 \right] > 0$$

Equation (B.16) governing plastic motion has the solutions for
 $0 < \tilde{t} < 2/n < t$ or $0 < 2/n < \tilde{t} < t$:

$$\begin{aligned} w_n &= w_n^* \cos \lambda_n^* (t - t^*) + \frac{v_n^*}{\lambda_n^*} \sin \lambda_n^* (t - t^*) \\ &+ \frac{\mu P}{(1 + \mu/n) \lambda_n^*} \int_{t^*}^t p_n^*(\tau) \sin \lambda_n^* (t - \tau) d\tau \end{aligned} \quad (B.21)$$

$$\text{where } \lambda_n^2 = k_2(n^2 - 1)(k_1 k_3 n^2 - \bar{w}_o)/(1 + \mu/n) > 0$$

and

$$\begin{aligned} w_n &= w_n^* \cos \lambda_n^* (t - t^*) + \frac{v_n^*}{\lambda_n^*} \sinh \lambda_n^* (t - t^*) \\ &+ \frac{\mu P}{(1 + \mu/n) \lambda_n^*} \int_{t^*}^t p_n^*(\tau) \sinh \lambda_n^* (t - \tau) d\tau \end{aligned} \quad (B.22)$$

$$\text{where } \lambda_n^2 = -k_2(n^2 - 1)(k_1 k_3 n^2 - \bar{w}_o) / (1 + \mu/n) > 0$$

The initial conditions are

$$w_n^* = w_n(t^*) = w_n(\tilde{t}) = w_n(2/n) = \tilde{w}_n \text{ for } \tilde{t} < 2/n$$

$$w_n^* = w_n(t^*) = w_n(\tilde{t}) = \bar{w}_n \text{ for } 2/n < \tilde{t}.$$

DISTRIBUTION LIST

DEPARTMENT OF DEFENSE

Assistant to the Secretary of Defense
ATTN: Honorable Donald R. Cotter

Director
Defense Advanced Research Project Agency
ATTN: A. Tachmindji
ATTN: STO, Kent Kresa
ATTN: Technical Library
ATTN: R. Chapman

Defense Documentation Center
12cy ATTN: TC

Director
Defense Intelligence Agency
ATTN: DT-2, Wpns. & Sys. Division
ATTN: DB-4C, Edward O'Farrell
ATTN: DT-1C
ATTN: Technical Library
ATTN: DI-7E

Director
Defense Nuclear Agency
ATTN: STSI, Archives
ATTN: DDST
3cy ATTN: STTL, Tech. Library
2cy ATTN: SPSS

Chairman
Dept. of Defense Explos. Safety Board
ATTN: DD/S&SS

Director of Defense Rsch. & Engineering
ATTN: AD/SW
ATTN: DD/S&SS
ATTN: DD/TWP
ATTN: AD/NP

Commander
Field Command, Defense Nuclear Agency
ATTN: FCPR

Director
Interservice Nuclear Weapons School
ATTN: Tech. Library

Director
Joint Strat. Tgt. Planning Staff, JCS
ATTN: STINFO Library

Chief
Livermore Division, Field Command
Defense Nuclear Agency
ATTN: FCPRL

DEPARTMENT OF THE ARMY

Deputy Chief of Staff for Rsch., Dev. & Acq.
ATTN: DAMA-CSM-N, LTC G. Ogden
ATTN: Tech. Library

Commander
Harry Diamond Laboratories
ATTN: DRXDO-TI, Tech. Library
ATTN: DRXDO-NP

DEPARTMENT OF THE ARMY (Continued)

Commander
U.S. Army Armament Command
ATTN: Tech. Library

Director
U.S. Army Ballistic Research Labs.
ATTN: Tech. Library, Edward Baicy

Commander
U.S. Army Communications Command
ATTN: Tech. Library

Director
U.S. Army Engr. Waterways Exper. Sta.
ATTN: John N. Strange
ATTN: Tech. Library
ATTN: William Flathau

Commander
U.S. Army Mat. & Mechanics Rsch. Ctr.
ATTN: Richard Shea

Commander
U.S. Army Nuclear Agency
ATTN: Tech. Library

DEPARTMENT OF THE NAVY

Chief of Naval Material
ATTN: MAT 0323

Chief of Naval Operations
ATTN: OP 985F
ATTN: OP 03EG

Chief of Naval Research
ATTN: Tech. Library
2cy ATTN: Nicholas Perrone

Officer-in-Charge
Civil Engineering Laboratory
Naval Construction Battalion Center
ATTN: Technical Library
ATTN: R. J. Odello

Commander
David W. Taylor Naval Ship R & D Center
ATTN: Code 11
ATTN: Code 2740, Y. F. Wang
ATTN: Code 1171
ATTN: Code 1731C
ATTN: Code 1962
ATTN: Code L42-3, Library
ATTN: Code 19
ATTN: Code 174, R. D. Short
ATTN: Code 1903

Commander
Naval Electronic Systems Command
Naval Electronic Systems Command Headquarters
ATTN: PME 117-21A

Commander
Naval Facilities Engineering Command
ATTN: Tech. Library

DEPARTMENT OF THE NAVY (Continued)

Superintendent
Naval Postgraduate School
ATTN: 2124, Tech. Rpts. Librarian

Director
Naval Research Laboratory
ATTN: Code 2027, Tech. Library
ATTN: Code 840, J. B. Gregory
ATTN: Code 8440, F. Rosenthal
ATTN: Code 8403, Robert O. Belshem
ATTN: Code 8403A, George J. O'Hara
ATTN: Code 8442, Hanson Huang

Commander
Naval Sea Systems Command
ATTN: ORD-91313, Library
ATTN: Code 03511, Carl H. Pohler

Commander
Naval Ship Engineering Center
ATTN: NSEC 6110.01
ATTN: NSEC 6105
ATTN: NSEC 6105G
ATTN: NSEC 6120D
ATTN: 6105C1
ATTN: Tech. Library

Commander
Naval Ship Rsch. and Development Center
Underwater Explosive Research Division
ATTN: Edward W. Palmer
ATTN: Tech. Library
ATTN: Code 17, William W. Murray

Commander
Naval Surface Weapons Center
ATTN: Code WA501, Navy Nuc. Progms. Off.
ATTN: Code WX21, Tech. Library
ATTN: Code 243, G. Young

Commander
Naval Surface Weapons Center
ATTN: Tech. Library

Commander
Naval Undersea Center
ATTN: Tech. Library

Commanding Officer
Naval Underwater Systems Center
ATTN: Code EM, Jack Kalinowski

Commander
Naval Weapons Center
ATTN: Code 533, Tech. Library

Commanding Officer
Naval Weapons Evaluation Facility
ATTN: Tech. Library

Director
Strategic Systems Project Office
ATTN: NSP-272
ATTN: NSP-43, Tech. Library

DEPARTMENT OF THE AIR FORCE

AF Geophysics Laboratory, AFSC
ATTN: SUOL, AFCRL Rsch. Library

DEPARTMENT OF THE AIR FORCE (Continued)

AF Institute of Technology, AU
ATTN: Library, AFIT Bldg. 640, Area B

AF Weapons Laboratory, AFSC
ATTN: SUL

Headquarters
Air Force Systems Command
ATTN: Technical Library

Commander
Armament Development & Test Center
ATTN: Tech. Library

ENERGY RESEARCH AND DEVELOPMENT ADMIN

University of California
ATTN: Tech. Info. Dept., L-3

Los Alamos Scientific Laboratory
ATTN: Doc. Con. for Reports Library

Sandia Laboratories
ATTN: Doc. Con. for Tech. Library

Sandia Laboratories
ATTN: Doc. Con. for 3141, Sandia Rpt. Coll.

U.S. Energy Rsch. & Dev. Admin.
Division of Headquarters Services
ATTN: Doc. Con. for Class. Tech. Library

DEPARTMENT OF DEFENSE CONTRACTORS

Agbabian Associates
ATTN: M. Agbabian

Battelle Memorial Institute
ATTN: Tech. Library

The BDM Corporation
ATTN: Tech. Library

The Boeing Company
ATTN: Aerospace Library

Cambridge Acoustical Assoc., Inc.
ATTN: M. C. Junger

Civil/Nuclear Systems Corp.
ATTN: T. A. Duffy

Columbia University
Dept. of Civil Engineering
ATTN: H. Bleich
ATTN: F. DiMaggio

General Dynamics Corp.
Electric Boat Division
ATTN: L. H. Chan

General Electric Company
TEMPO-Center for Advanced Studies
ATTN: DASIAC

IIT Research Institute
ATTN: Tech. Library

DEPARTMENT OF DEFENSE CONTRACTORS
(Continued)

Institute for Defense Analyses
ATTN: IDA Librarian, Ruth S. Smith

Kaman Avidyne
Division of Kaman Sciences Corp.
ATTN: G. Zartarian
ATTN: E. S. Criscione
ATTN: Technical Library

Kaman Sciences Corporation
ATTN: Library

Lockheed Missiles and Space Company
ATTN: Tech. Info. Center, D/Coll.
ATTN: Tom Geers, D/52-33, Bldg. 205

University of Maryland
Dept. of Civil Engineering
ATTN: Bruce S. Berger

Merritt Cases, Incorporated
ATTN: Technical Library

Newmark, Nathan M.
Consulting Engineering Services
ATTN: Nathan M. Newmark

DEPARTMENT OF DEFENSE CONTRACTORS
(Continued)

Polytechnic Inst. of Brooklyn
Dept. of Aerospace & Applied Mech.
ATTN: J. M. Klosner

R & D Associates
ATTN: Tech. Library

Stanford Research Institute
ATTN: Burt R. Gasten
ATTN: George R. Abrahamson
ATTN: A. L. Florence

Tetra Tech, Inc.
ATTN: Tech. Library
ATTN: Li-San Hwang

URS Research Company
ATTN: Technical Library

Weidlinger Assoc. Consulting Engineers
ATTN: Melvin L. Baron